Department of Physics and Astronomy

University of Heidelberg

Master's thesis

in Physics

submitted by

Viola Rädle

born in Speyer

2019

Multi-tracer study for groundwater dating in Southern Oman

This Master's thesis has been carried out by Viola Rädle

at the

Institute of Environmental Physics

under the supervision of

Prof. Dr. Werner Aeschbach

Abstract

This thesis reports on a multi-tracer study to investigate the groundwater system in the Salalah Plain in Southern Oman. Hydrogeological studies in this area are of great significance as extensive groundwater abstraction has led to serious environmental problems. To resolve open questions from former studies, ^{39}Ar was chosen as a dating tracer for its conservative properties and its suitable dating range. To facilitate the purification of argon for its detection with Argon Trap Trace Analysis, a conversion factor for volume estimation of small samples was determined and the pressure readout was automated by a Labview program. In addition to ^{39}Ar, other dating tracers were applied, i.e. noble gases, ^{14}C, CFCs and SF_6. While radiogenic ^{4}He served as an initial qualitative dating approach, ^{14}C tracer ages were calculated and corrected yielding mean residence times of up to 7000 years. In contrast, tracer ages derived from CFCs and SF_6 data ranged from 20 to 50 years. In a mixing model with two water masses, ^{14}C and CFC-11 data were combined. On average, the contributions of the modern component and a 2000 to 19 000 years old component were found to be almost equal. Combining those findings with prospective ^{39}Ar results sheds light on the so-far contradictive groundwater system in the Salalah Plain.

Zusammenfassung

Im Rahmen dieser Arbeit wurde mithilfe mehrerer Tracer eine Grundwasserstudie in der Salalah Plain im Süden Omans durchgeführt. Aufgrund von Umweltschäden durch umfangreiche Grundwasserentnahmen sind hydrogeologische Untersuchungen in dieser Region von großer Wichtigkeit. Um offene Fragen aus früheren Studien zu klären, wurde neben anderen Methoden ^{39}Ar zur Datierung genutzt, da es neben seinen konservativen Eigenschaften die hier wichtige Zeitskala zwischen 50 und 1000 Jahren abdeckt. Um die notwendige Probenaufbereitung für die Messung mit Argon Trap Trace Analysis zu erleichtern, wurde an der bestehenden Argonseparationsanlage die Volumenabschätzung für kleine Proben kalibriert und die Drucksteuerung durch ein Labview-Programm automatisiert. Neben ^{39}Ar wurden Edelgase, ^{14}C, CFCs und SF_6 analysiert. Für eine erste qualitative Abschätzung der Grundwasseralter wurde radiogenes ^{4}He untersucht. Korrigierte ^{14}C Werte ergaben Traceralter von bis zu 7000 Jahren, wohingegen Analysen von CFCs und SF_6 Traceralter zwischen 20 und 50 Jahren ergaben. Um Daten von ^{14}C und CFC-11 zu vergleichen, wurde ein Mischungsmodell zweier Wassermassen aufgestellt. Durchschnittlich ergab das Modell Beiträge aus gleichen Teilen von einer modernen und einer 2000 - 19 000 Jahre alten Komponente. Die Kombination dieser Ergebnisse mit den noch ausstehenden ^{39}Ar Daten wird wichtige Aufschlüsse über ungeklärte Aspekte des Grundwassersystems in der Salalah Plain geben.

Contents

1 Introduction

Groundwater, the world's largest freshwater reservoir, has become increasingly important as perennial source of water supply for municipal, agricultural and industrial use. Especially in arid regions, the reliance of irrigation is focused solely on groundwater. However, extensive abstraction has led to a depletion of groundwater in many parts of the world [Richey et al., 2015; Schwartz and Ibaraki, 2011], including the irreversible mining of fossil waters in the Arabian Peninsula [Kinzelbach et al., 2002]. The water quality of aquifers in coastal areas is of particular concern as altered hydraulic heads may lead to seawater intrusions [Bear and Cheng, 1999]. For a sustainable groundwater management a figure of great significance is the amount of recharge drawn by an aquifer [Kinzelbach et al., 2002]. However, determining this quantity proves to be difficult [Alley, 2002]. Besides other methods, this is approached by groundwater dating with environmental tracers revealing water flow on different time scales [Kinzelbach et al., 2002; Solomon et al., 1993]. A broad spectrum of dating tracers is applied in environmental studies, exhibiting characteristic advantages and weaknesses. To warrant the credibility of a tracer age, the comparison with results deduced from other tracers is crucial. Hence, multi-tracer studies pose a reasonable approach for the thorough investigation of a study area.

In the area of interest, the Salalah Plain in Southern Oman, seawater intrusions as a result of groundwater abstraction are posing a threat on the maintainability of the freshwater supply [Shammas and Jacks, 2007]. Despite a variety of hydrogeological studies [Clark et al., 1987; Askri et al., 2016; Mueller, 2012; Strauch et al., 2014], the complex groundwater system in the Salalah Plain has not yet been well understood. For a better insight, a joint project was launched between the German Helmholtz Centres *GEOMAR Kiel* and *UFZ Leipzig* and the Omani *Institute of Advanced Technology Integration (IATI)*. In this context, a multi-tracer study was conducted in May 2018 to investigate groundwater ages. Besides noble gases, ^{14}C, CFCs and SF$_6$, the most valuable tracer in this study was the noble gas radioisotope ^{39}Ar. In addition to its chemical inertness, ^{39}Ar offers a suitable dating range for the expected groundwater ages. Hence, this study was one of the first applications of ^{39}Ar using the newly developed ArTTA (Argon Trap Trace Analysis) detection setup at the *Kirchhoff Institute for Physics, University of Heidelberg.*

The following chapter gives an introduction to the theoretical basics of groundwater hydrology, environmental tracers, groundwater age representations and the ArTTA setup. Chapter 3 describes the sampling and purification techniques as well as the improvements of the existing argon purification setup carried out in the course of this thesis. Those encompass the determination of a conversion factor for volume estimation of small samples and the automation of the pressure readout by a Labview program. Chapter 4 reports on the multi-tracer study in the Salalah Plain including preliminary considerations, the sampling campaign, data evaluation, interpretation and discussion. Finally, chapter 5 sums up the findings of this work and gives an outlook on further steps of the project in the near future.

2 Fundamentals

This chapter addresses the theoretical aspects fundamental for the understanding of the projects carried out in this thesis. First, processes in groundwater are discussed, including terminology, quantitative considerations of the flow and gas exchange. Subsequently, an overview on tracers used in groundwater hydrology is given. The mathematics to calculate the tracer age and excess air content of a sample is outlined as well as the application of field parameters to investigate the groundwater chemistry. At last, the measurement technique for ^{39}Ar, Argon Trap Trace Analysis (ArTTA), is explained.

2.1 Groundwater

Freshwater as a crucial element for biological life is a precious resource. While oceans account for most of Earth's total water, only 2.5 % are available as freshwater, of which 30.1% is stored as groundwater. Thus, groundwater represents the largest freshwater reservoir accessible for human use [Fitts, 2013]. Although surface water, i.e. lakes and rivers, can be accessed more easily, it often suffers from anthropogenic pollution and its availability is locally variant. Therefore, many regions rely on freshwater conveyed by extracting groundwater.

Apart from its function as drinking water, groundwater serves as an environmental archive. Extracting water that has been enclosed from the atmosphere for many years can reveal information on the geology, on subsurface biological and chemical processes and on environmental parameters at the time of formation.

In order to understand relevant mechanisms in groundwater, the underlying principles will be discussed in the following.

2.1.1 Hydrological cycle and subsurface structure

On Earth, water is stored and transported through different reservoirs. The hydrological cycle depicted in Figure 2.1 includes gravitational and pressure-driven flow, evapotranspiration, condensation, atmospheric circulation, precipitation, freezing and melting of water. It represents a spatially and temporally averaged model of global means. Groundwater as one of those reservoirs is mainly recharged by precipitation, surface water or melting ice and naturally discharges to oceans or surface water bodies.

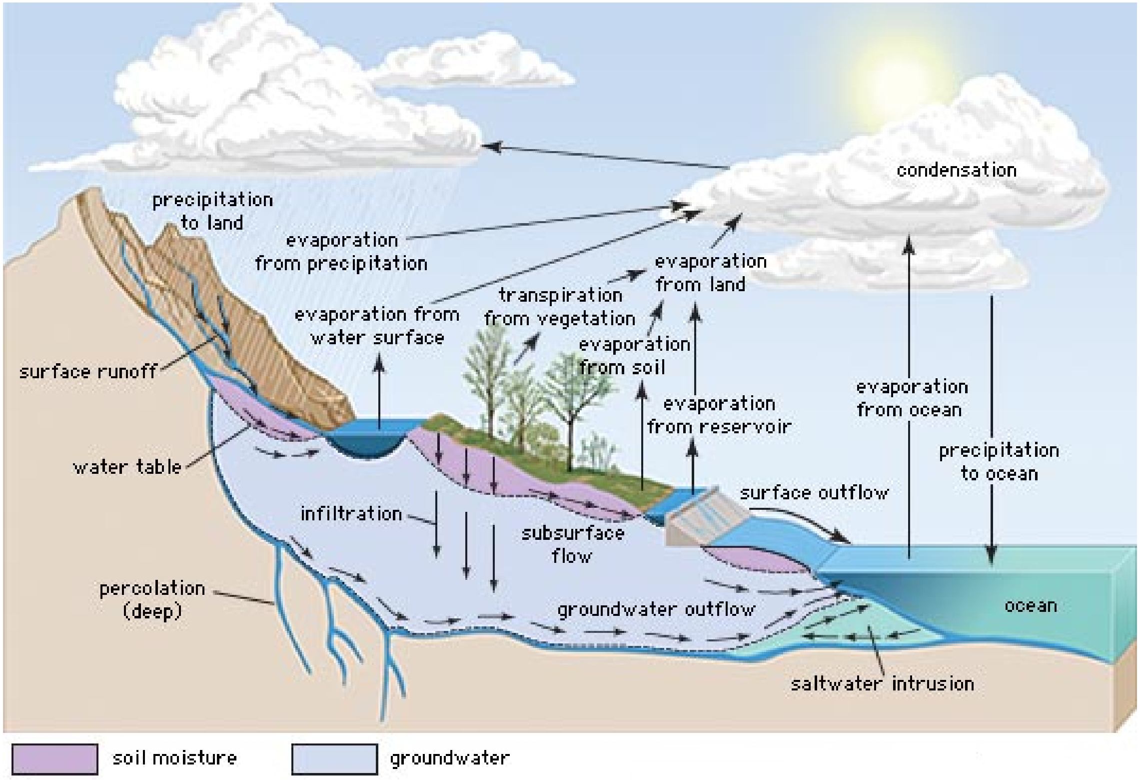

Figure 2.1: The hydrological cycle: Different reservoirs store and exchange water [Britannica, 2018].

During infiltration, water percolates into soil pores and rock fractures of different size. The subsurface can be divided into different zones as shown in Figure 2.2. In the upper zone, the *vadose (unsaturated) zone*, pore space is still partially filled with air, leading to an equilibrium between water and soil air. Subsurface water in the vadose zone is referred to as *soil moisture*, *soil water* or *vadose water*. Capillary forces from surface tension arise as the water is dragged towards soil grain surfaces. As soil water pressures are less than atmospheric ones, capillary rise proceeds until hydrostatic equilibrium is reached.

The zone saturated in water but still above the groundwater table, with water pressures lower than atmospheric ones, is often referred to as the *capillary fringe*. Its thickness depends on the pore size: while small pore sizes cause high capillary rise, only thin capillary fringes are found in areas of large pore sizes [Roth, 2017]. As water migrates deeper into the ground, it reaches the groundwater table below which the *phreatic (saturated) zone* is situated. All pores are filled with water, resulting in a seclusion of the contained *groundwater* from atmospheric air until it leaves this reservoir by natural discharge or extraction.

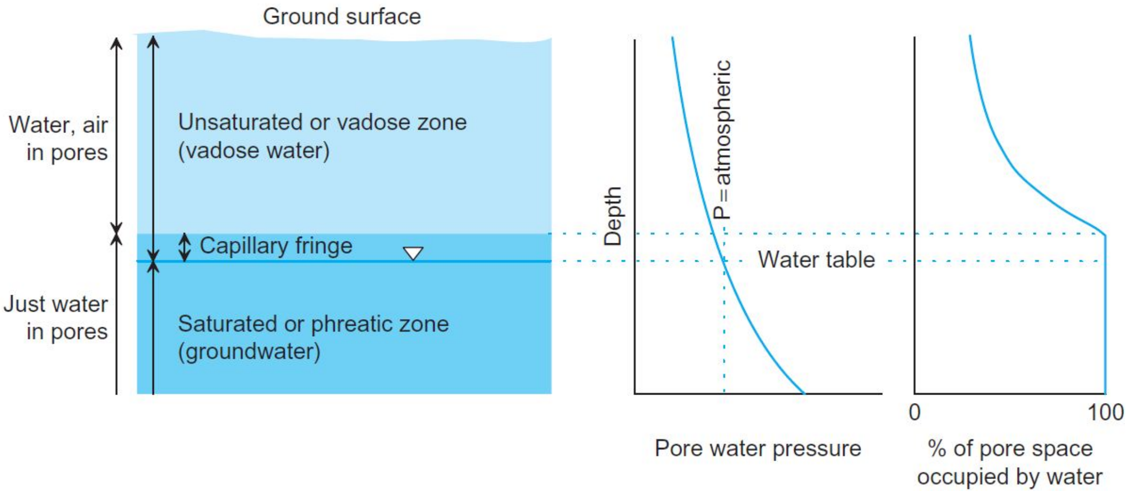

Figure 2.2: Vertical cross-section of the subsurface structure (left). The saturated zone is defined by the water table where the pore water pressure is atmospheric and where all pore space is occupied by water (right) [Fitts, 2013].

2.1.2 Aquifers and hydraulic head

Geological formations with pores that enable groundwater flow and storage are referred to as *aquifers*. An important property of aquifers is the dimensionless *porosity* n, defined as

$$n = \frac{V_{\text{pore}}}{V_{\text{total}}}. \tag{2.1}$$

with $0 < n < 1$. It is a measure for the pore volume relative to the total volume element. For groundwater flow considerations, however, it has to be taken into account that not all pore space contributes to water storage and flow, leading to the *effective porosity* $n_{\text{e}} \leq n$. Materials with high amounts of pores that are not part of the interconnected pore system show significant deviations of those two quantities. The lower boundary of an aquifer is usually restricted by an underlying, impermeable layer called *aquitard*. An aquifer is called *unconfined* if its upper boundary is not vertically limited by an aquitard, causing it to rise freely to the level at which the surface pressure equals the atmospheric one. If an aquifer is *confined* by an aquitard above, higher pressures are usually found. This can be quantified using a measure called *hydraulic head*, defined as the potential height the water level would rise to in an open borehole. It can be considered the actual vertical position z of a water parcel above the $z = 0$ point, corrected by its internal (pressure) energy:

$$\begin{aligned} h &= \frac{E_{\text{tot}}}{mg} \\ &\approx \frac{pV + mgz}{mg} \\ &= \frac{p}{\rho g} + z \end{aligned} \tag{2.2}$$

with
h : hydraulic head
E_{tot} : total energy
p : pressure
V : volume of water element
m : mass of water element

The kinetic energy was neglected due to low velocities in groundwater. For simplicity, vectorial notation was renounced since the z axis points upwards and $\vec{g} = g \cdot \vec{e}_z$. By definition, the hydraulic head of an unconfined aquifer equals the water table while in a confined aquifer it is higher. It is measured by piezometers, open pipes in which the rise of the water table can be observed. Mapping an area of interest with those measurements defines the *potentiometric surface.*
Figure 2.3 shows an aquifer system with an unconfined upper and a confined lower aquifer, seperated by aquitards. While the water level in the well of the unconfined aquifer equals its water table, the water in the well tapping the confined aquifer rises up to the potentiometric surface, way higher than the aquifer's upper boundary.

2.1.3 Groundwater flow

Groundwater is not a static reservoir; it contributes to the hydrological cycle through infiltration, subsurface transport and outflow. For the mathematical derivation of groundwater flow, a scale analysis is done to simplify the Navier-Stokes equation for

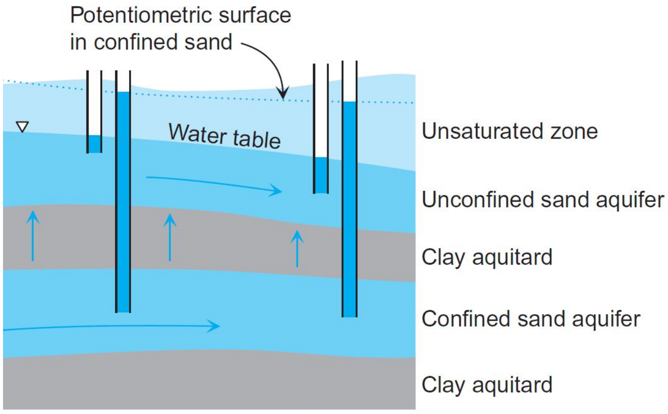

Figure 2.3: Vertical cross-section through an aquifer system. The water level of the upper, unconfined aquifer is at the same height as its water table: $h = z$. The lower aquifer is confined by an aquitard. The head h is higher than z, allowing for the water in the well to rise much higher than the water table of the aquifer [Fitts, 2013].

incompressible fluids, i.e.

$$\underbrace{\frac{\partial \vec{v}}{\partial t} + (\vec{v} \cdot \vec{\nabla})\vec{v}}_{=0} = \underbrace{-\frac{1}{\rho}\vec{\nabla}p}_{\text{pressure gradient}} - \underbrace{\vec{g}}_{\text{gravitation}} - \underbrace{2(\vec{\Omega} \times \vec{v})}_{\text{Coriolis}} + \underbrace{\nu\,\Delta\vec{v}}_{\text{viscosity}} \tag{2.3}$$

$$\text{with} \quad \begin{aligned} \vec{\Omega} &: \quad \text{rotation rate of the Earth} \\ \nu &: \quad \text{kinematic viscosity} \ . \end{aligned}$$

Under the assumption of a stationary, slow, incompressible flow, this simplifies to

$$0 = -\frac{1}{\rho}\vec{\nabla}p - \vec{g} + \nu\,\Delta\vec{v}. \tag{2.4}$$

As $\Delta\vec{v}$ is parallel to $-\vec{v}$ [Roth, 2017], the viscosity term can be expressed as

$$\vec{v} = -k\Delta\vec{v} \tag{2.5}$$

with the intrinsic permeability k, leading to

$$\begin{aligned} 0 &= -\frac{1}{\rho}\vec{\nabla}p - \vec{g} - \frac{\nu}{k}\vec{v} \\ \rightarrow \vec{v} &= \frac{k}{\nu}\left(\frac{1}{\rho}\vec{\nabla}p + \vec{g}\right) \ . \end{aligned} \tag{2.6}$$

With the definition of the hydraulic head (Eq. 2.2), the pressure gradient can be formulated as:

$$\begin{aligned} \frac{1}{\rho}\vec{\nabla}p &= \vec{\nabla}\left[g \cdot (h - z)\right] \\ &= g \cdot \left(\vec{\nabla}h - \vec{\nabla}z\right) \\ &= g \cdot \left(\vec{\nabla}h - \vec{e}_z\right) \\ &= g\vec{\nabla}h - \vec{g} \end{aligned} \tag{2.7}$$

Inserting this into Eq. 2.6 yields:

$$\begin{aligned} \vec{v} &= \frac{k}{\nu}\left(g\vec{\nabla}h - \vec{g} + \vec{g}\right) \\ &= \frac{k}{\nu}\, g\vec{\nabla}h \end{aligned} \tag{2.8}$$

Instead of a scalar permeability k, a tensor $\mathbf{k}$ is needed as the permeability is an anisotropic property. Introducing the hydraulic conductivity $\mathbf{K} := \frac{\mathbf{k}}{\nu}\, g$ [Hubbert, 1940] leads to *Darcy's law*:

$$\vec{q} = -\mathbf{K} \cdot \vec{\nabla}h \tag{2.9}$$

with the Darcy velocity $\vec{q}$ in m/s. The hydraulic conductivity $\mathbf{K}$ is a material property of the pore space. It is an anisotropic tensor as the conductivity depends on the flow direction, especially on the distinction between horizontal and vertical movement. In a coordinate system along the layers, it is typically found that $K_{xx} \approx K_{yy} > K_{zz}$.

Darcy's law shows that water flow always occurs against the head gradient, meaning towards areas of lower hydraulic head. This is an important aspect for the extraction of water from an aquifer. A depression cone of the head is found around the area of pumping, affecting the groundwater flow of the surroundings.

Substances are transported in groundwater by *advective* and by *dispersive* flow. While advection is defined as the transport by a mean flow field, dispersion denotes the widening of a distribution [Aeschbach, 2017]. The spreading is caused by direction changes enforced by the solid grain matrix. In addition, different pore sizes and velocity profiles inside the pores exist. The effect of dispersion can be quantified and corrected for which is outlined in Section 2.3.

2.1.4 Groundwater budget

As groundwater constitutes a dynamic reservoir, a budget of all incoming and outgoing fluxes can be formulated. Infiltration from surface water bodies or precipitation into groundwater will be denoted as recharge R. It is important to note that not all water entering the soil will eventually reach the groundwater and count as recharge. A part of it returns to the atmosphere by evapotranspiration, meaning the combined effect of evaporation and transpiration by plants [Alley, 2002]. After infiltration, the fluid is stored and transported through the aquifer as part of the groundwater body. Eventually, it is discharged into other reservoirs (discharge D) or removed by pumping P.

The rate of change in the stored water is expressed as

$$\begin{aligned} \frac{dV}{dt} &= \text{flux in} - \text{flux out} \\ &= R - D - P\,. \end{aligned} \tag{2.10}$$

In natural conditions, marked with index 0, no pumping occurs ($P = 0$) and the system is in steady state ($\frac{dV}{dt} = 0$). Inserting this in the budget equation (Eq. 2.10) shows that recharge is balanced by discharge:

$$R_0 = D_0 \tag{2.11}$$

Now, a pump tapping the aquifer is installed in this steady-state system, i.e. $P \neq 0$. This will have an effect on the budget: First of all, $\frac{dV}{dt} = 0$ cannot be ensured any more. In addition, the pumping may have secondary effects on the recharge and discharge behaviour of the aquifer. Other reservoirs, i.e. surface waters and oceans, are affected as they are closely linked to the groundwater flux system [Sophocleous, 2002]. The hydraulic head is lowered in the area of pumping, in the shape of an (anisotropic) depression cone. As the main driver of groundwater flow, this may induce altered fluxes and interactions with surrounding reservoirs.

On the recharge side, pumping for (agricultural) irrigation may induce irrigation return flow to the aquifer. Besides, the depression of the hydraulic head may cause recharge fluxes from other reservoirs like rivers, lakes or oceans. (As a sideline, pumping in coastal areas inducing seawater intrusions may pose major environmental problems on the aquifer system.) In areas of rejected recharge (e.g. with water table close to the soil surface and water lost as surface runoff), pumping may lower the water table or change the saturation in the vadose zone [Devlin and Sophocleous, 2005]. As a consequence, the hydraulic conductivity of the recharge zone may be altered as it is highly dependent on the degree of saturation [Roth, 2017]. This, together with a change in vegetation, will influence the fraction of soil water lost to evapotranspiration. Finally, as the pore fluid provides mechanical support, the degree of saturation may also change the soil matrix structure, its compaction and the porosity [Alley, 2002]. All those aspects concerning the recharge units may lead to a different behaviour of infiltration and evapotranspiration and therefore cause a difference in recharge ΔR_0. Thus, the recharge R consists of the natural recharge R_0 and pumping-induced changes ΔR_0:

$$R = R_0 + \Delta R_0 \ . \tag{2.12}$$

For the discharge D, similar considerations can be made. Depending on the magnitude of the pumping rate in relation to the discharge, major adjustments of the groundwater system may occur in response to pumping. As a consequence, the discharge behaviour to other reservoirs may be changed, since they are closely linked in the hydrological cycle as described in Section 2.1.1. For instance, if the depression of the hydraulic head reaches a neighbouring reservoir and declines drastically with respect to the reservoir boundaries, a discharge of the groundwater may no longer occur. Those changes in discharge are expressed as ΔD_0, with

$$D = D_0 + \Delta D_0 \ . \tag{2.13}$$

As pumping extracts parts of the water body volume, it will most likely result in a diminishing of the discharge to other reservoirs, so in most cases, ΔD_0 is a negative number.

The groundwater budget including pumping (after [Bredehoeft, 2002]) can now be written as

$$\frac{dV}{dt} = (R_0 + \Delta R_0) - (D_0 + \Delta D_0) - P. \tag{2.14}$$

To ensure a steady state with sustainable pumping, meaning a pumping rate that can be maintained indefinitely without dewatering or mining an aquifer [Devlin and Sophocleous, 2005], $\frac{dV}{dt} = 0$ is required. Using Eq. 2.11 shows that this only applies for

$$P \overset{!}{=} \Delta R_0 - \Delta D_0, \tag{2.15}$$

so the extracted water must be balanced by pumping-induced changes in recharge and discharge. Even if the groundwater volume remains unchanged, consistent pumping can imply a drastic change in the water budget for all surrounding reservoirs, especially for the units the groundwater was formerly discharged to. If $\frac{dV}{dt} = 0$ cannot hold, the long-term groundwater budget will adjust until a new steady state is established. The water body in the aquifer will decrease in size and the ability to extract water for human usage cannot be guaranteed any more.

2.1.5 Gas exchange

Groundwater not only provides a storage volume for freshwater but is also of scientific value. In this context, it can reveal a variety of information linked to prevalent environmental conditions at the time of infiltration. This is possible as once having entered the saturated zone, the water is enclosed from atmosphere. Ideally, no further interactions occur until the time of sampling. As many tracer methods rely on the analysis of gases dissolved in the water samples, the process of gas exchange will be explained in this section. All information was taken from Aeschbach [2017].

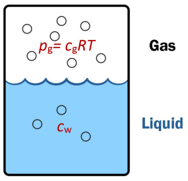

Figure 2.4: The equilibrium between the partial pressure p_{g} of a gas and its concentration in water c_{w} is determined by Henry's law (draft adapted from Detwiler [2015].

When water is in contact with air, an equilibrium of a substance's concentration in the water phase c_w and its partial pressure in the gas phase p_g will establish according to *Henry's law* (draft adapted from Detwiler [2015]):

$$K_\mathrm{H} = \frac{p_\mathrm{g}}{c_\mathrm{w}} \tag{2.16}$$

The Henry coefficient K_H has the unit [atm L mol^{-1}]. It can also be converted into a dimensionless coefficient K'_H by expressing the partial pressure p_g in terms of the gas-side concentration c_g:

$$\begin{aligned} p_\mathrm{g} &= \frac{nRT}{V} = c_\mathrm{g}RT \qquad\qquad \text{in (2.16)} \\ \rightarrow K'_\mathrm{H} &:= \frac{K_\mathrm{H}}{RT} \;=\; \frac{c_\mathrm{g}}{c_\mathrm{w}} \end{aligned} \tag{2.17}$$

In literature, the equilibrium concentration of a gas in water is often described using the dimensionless *Ostwald solubility*

$$L = \frac{1}{K'_\mathrm{H}} = \frac{c_\mathrm{w}}{c_\mathrm{g}} \; . \tag{2.18}$$

In this thesis, the Ostwald solubility will be the measure used. It is primarily dependent on the temperature and salinity of the water as well as on the gas considered. In figure 2.5, the solubility of all gases relevant for this thesis are depicted. The calculation and data are found in Section 6.1.

2.2 Tracers in groundwater hydrology

Isotope hydrology encompasses the application of environmental tracers to study the hydrological cycle and aquatic systems in order to identify different water components, mixing, recharge areas and rates, flow paths and velocities [Aeschbach, 2017]. Tracers are substances (solutes and isotopes) that mark the water's origin, its age or environmental processes that unfold in water. They range from gases dissolved in water and the water's isotopic composition to water features like temperature and salinity.

In the beginning of this section, tracers for groundwater chemistry are presented. As the main focus of this thesis lies on isotope methods, a short introduction into

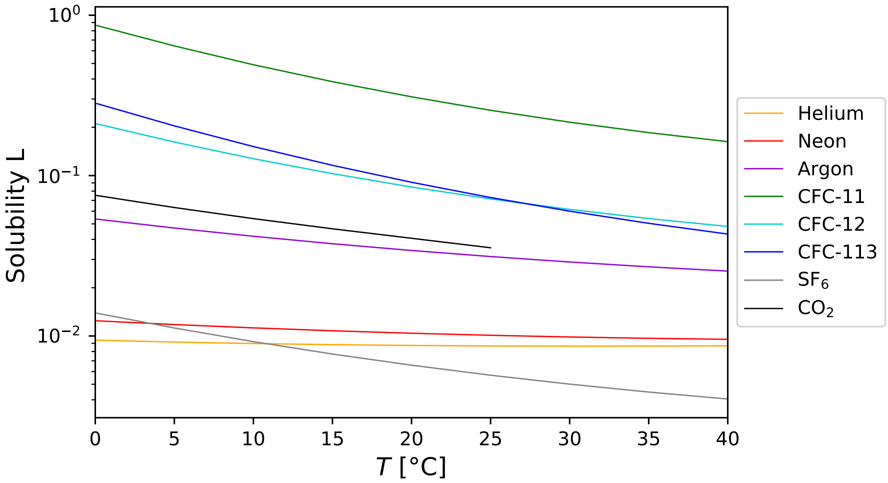

Figure 2.5: Temperature dependence of the solubility of gases in water with salinity $S = 0$, pressure $p = 1\,\text{atm}$. Data taken from Weiss [1971] (He and Ne), Weiss [1970] (Ar), Warner and Weiss [1985] (CFC-11 and CFC-12), Bu and Warner [1995] (CFC-113), Bullister et al. [2002] (SF_6) and Aeschbach [2017] (CO_2).

the terminology is given in the following. Finally, a variety of tracer application principles is discussed as well as the individual tracers applied in the course of this thesis.

2.2.1 Tracers to investigate groundwater chemistry

To understand subsurface processes it is essential to consider geochemical aspects in groundwater. Those data can provide information on properties of the recharge area and on the aquifer that the calculated tracer ages have to be corrected for [IAEA, 2013]. As geochemical data were measured on site, they are referred to as *field parameters*. The field parameters of importance for this study are salinity, oxygen content, pH and titration and are presented in the following.

Salinity

Naturally, a variety of inorganic ionic solutes are found in water. The amount of dissolved ions is characterized by the *salinity* defined as the mass of ions per water volume. To determine the salinity of a sample water, the *electric conductivity* κ in $\left[\frac{\mu\text{S}}{\text{cm}}\right]$ is measured. As κ is temperature dependent, it is converted to a standard temperature of $T = 20\,°\mathrm{C}$ [Aeschbach, 2017]:

$$\kappa_{20} = \kappa_T \cdot (1.72118 - 0.0541369\,T + 1.14842 \cdot 10^{-3} \cdot T^2 - 1.222651 \cdot 10^{-5} \cdot T^3) \quad (2.19)$$

with κ_{20} : electric conductivity at $T = 20\,°\mathrm{C}$
κ_T : electric conductivity at sampling temperature T (measured during sampling)

Note that some devices give an EC value normed to 25°C.
This empirical formula holds for waters dominated by $\mathrm{Ca(HCO_3)^{2\text{-}}}$. For these waters[1], the salinity S is derived by

$$S = \eta \cdot \kappa_{20} \quad (2.20)$$

with S : salinity in ‰
η : proportionality factor, for $\mathrm{Ca(HCO_3)_{2\text{-}}}$-dominated waters: $\eta \approx 0.87 \cdot 10^{-3} \frac{\mathrm{cm}}{\mathrm{\mu S}}$ ‰

As the solubility of gases in water is dependent on salinity, this parameter will be important for the data analysis in Section 4.3.

Oxygen concentration

While rainwater is saturated in oxygen and exhibits concentrations around 10 mg/L, substantially lower concentrations are found in groundwater [Fitts, 2013]. The reason for this is the consumption of oxygen by organic matter in the soil as water infiltrates into the ground. This process is referred to as *aerobic respiration*. Environments with a lack of oxygen, e.g. due to contamination with fuel, are called *anoxic*. As aerobic respiration cannot be administered, different kinds of microbes are found using other processes to release energy.
Generally, the oxygen content of groundwater reveals its state with respect to the prevalent microbial reactions. Hence, it can be an indicator for microbial consumption of a tracer, i.e. of CFCs (compare Section 2.2.5). In field applications the oxygen concentration also serves as a measure for the gas exchange with atmosphere. As stagnant (atmosphere equilibrated) water generally exhibits higher oxygen concentrations, the parameter is monitored while water contaminated with atmosphere is

---

[1] This assumption is valid for most samples analyzed in this campaign

removed from the well before sampling. During this process, the oxygen concentration usually decreases and approaches a constant value.

pH

The pH is a quantification of the H^+ activity in water:

$$[\mathrm{H}^+] = 10^{-\mathrm{pH}}. \tag{2.21}$$

Neutral water is defined as pH = 7 [Fitts, 2013]. At lower pH it is denoted *acidic* whereas at higher pH it is called *basic*. Groundwater is usually in the pH neutral range [Clark and Fritz, 1997].
For this thesis the pH is of particular interest as it is a measure for the relative contribution of the carbon species found in the water. This is explained in Section 2.2.5.

Titration and alkalinity

In titration, sulfuric acid (H_2SO_4) is added to a given volume of sample water until a pH of 4.3 is reached. The amount of acid added is converted into *alkalinity* (Alk) and reported in terms of mg/L $CaCO_3$, which is the amount of calcium carbonate dissolved in water that would be necessary to produce an equal alkalinity [Clark and Fritz, 1997]. With this, the alkalinity of a bicarbonate-equivalent can be derived:

$$\mathrm{Alk}\left[\frac{\mathrm{mg}}{\mathrm{L}}\right]_{\mathrm{HCO_3^-}-\mathrm{eqiv}} = \mathrm{Alk}\left[\frac{\mathrm{mg}}{\mathrm{L}}\right]_{\mathrm{CaCO_3}-\mathrm{eqiv}} \cdot \frac{M_{\mathrm{eq}}(\mathrm{HCO_3^-})}{M_{\mathrm{eq}}(\mathrm{CaCO_3})}\,, \tag{2.22}$$

with equivalent masses

$$M_{\mathrm{eq}}(\mathrm{CaCO_3}) = \frac{M_{\mathrm{molar}}(\mathrm{CaCO_3})}{valence} = \frac{100.09}{2}\,\frac{\mathrm{g}}{\mathrm{mol}} = 50.05\,\frac{\mathrm{g}}{\mathrm{mol}} \quad \text{and}$$

$$M_{\mathrm{eq}}(\mathrm{HCO_3^-}) = \frac{M_{\mathrm{molar}}(\mathrm{HCO_3})}{valence} = \frac{61.02}{1}\,\frac{\mathrm{g}}{\mathrm{mol}} = 61.02\,\frac{\mathrm{g}}{\mathrm{mol}}\,. \tag{2.23}$$

Alkalinity is defined as the sum of negative charges neutralizing H^+ ions, thus buffering the pH [Roy-Barman and Jeandel, 2016]. Considering the most abundant carbon species in water gives

$$\mathrm{Alk} \approx [\mathrm{HCO_3^-}] + 2 \cdot [\mathrm{CO_3^{2-}}] \tag{2.24}$$

which is used for the Tamers model in radiocarbon dating (Section 2.2.5).

2.2.2 Isotopic fractionation

As a variety of isotope methods are applied in the scope of this thesis, this section gives a short introduction to isotopes and fractionation processes.
Isotopes of an element are atoms with the same number of protons Z but varying number of neutrons N. Therefore, they are commonly identified by their atomic weight

$$A = N + Z. \tag{2.25}$$

For many elements, constant ratios of their isotopes are found within certain reservoirs. Thus, the ratio found in a sample can be compared to well-defined standard values using a Delta notation. As an example, $\delta^{13}\mathrm{C}$ (in ‰) is defined as:

$$\begin{aligned}\delta^{13}\mathrm{C} &= \frac{{}^{13}\mathrm{R_{sample}} - {}^{13}\mathrm{R_{standard}}}{{}^{13}\mathrm{R_{standard}}} \cdot 1000 \\ &= \frac{\frac{^{13}\mathrm{C}}{^{12}\mathrm{C}}\Big|_{\mathrm{sample}} - \frac{^{13}\mathrm{C}}{^{12}\mathrm{C}}\Big|_{\mathrm{standard}}}{\frac{^{13}\mathrm{C}}{^{12}\mathrm{C}}\Big|_{\mathrm{standard}}} \cdot 1000\ . \end{aligned} \tag{2.26}$$

Several mechanisms alter those isotopic ratios as the mass difference between isotopes changes their thermodynamic behaviour and reaction rate [Clark and Fritz, 1997]. Those effects are called *fractionation*. Generally, heavy isotopes are less mobile and reactive than the abundant light ones [Aeschbach, 2017], which affects the isotope ratio in the change of physical state (e.g. evaporation) or chemical reactions (e.g. carbon chemistry in water). In addition, biologic fractionation is found, i.e. plants preferably incorporate light carbon isotopes in photosynthesis [Mook, 2002]. These aspects are discussed in further detail in Section 2.2.5.

2.2.3 Excess air

For the correct analysis of tracer data, the influence of *excess air* has to be taken into account. Excess air denotes a gas surplus entrapped in the subsurface and dissolved in groundwater. During groundwater recharge, the water table rises while some pore space is still filled with air. Due to the increase in hydraulic pressure an abundance of gases enter the water, leading to concentrations higher than the expected atmospheric equilibrium. As the gas concentrations in water are used for groundwater age calculations, it is important to quantify the portion. This Section only considers a simple approach to characterize excess air, fractionation is not taken into account. However, more elaborate models exist and can be found in literature [Kipfer et al., 2002].

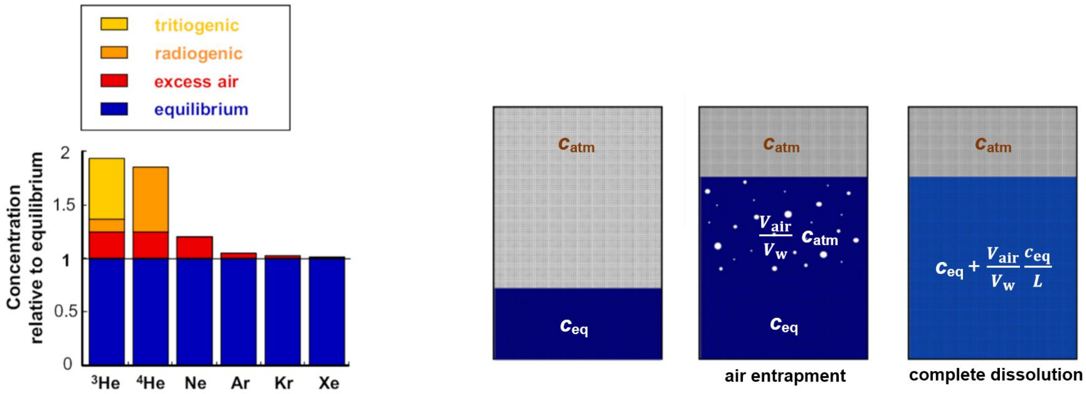

Figure 2.6: Left: noble gas components in groundwater. Right: Excess air model: complete, unfractionated dissolution of air entrapped in water [Aeschbach, 2017].

As depicted in Figure 2.6 (left), the concentration of individual noble gases in water originate from different processes. Besides the air-equilibrated fraction (indicated in blue), the influence of excess air (red) is shown. For ^{3}He and ^{4}He, additional components of radiogenic origin are found (orange), whereas ^{3}He is also produced by decaying tritium (yellow).

On the right side of Figure 2.6, the *Unfractionated Excess Air Model (UA)* is shown. Air bubbles with atmospheric gas composition c_{atm} are entrapped in equilibrated water with concentration c_{w}. Assuming a complete dissolution without fractionation, the resulting gas concentration in the water can be derived using Henry's law

(Eq. 2.18):

$$\begin{aligned} c_{\text{tot}} &= c_{\text{eq}} + \frac{V_{\text{air}}}{V_{\text{w}}} \cdot c_{\text{atm}} \\ &= c_{\text{eq}} \left(1 + \frac{1}{L} \cdot \frac{V_{\text{air}}}{V_{\text{w}}} \right) \end{aligned} \tag{2.27}$$

It can be seen that gases with high solubility L (e.g. Xe, CO_2) are less affected by excess air than gases with low solubility (e.g. Ne, SF_6). For a known infiltration temperature, salinity and altitude, the amount of a noble gas i (i ϵ {Ne, Ar, Kr, Xe}) dissolved due to excess air can be calculated [Kipfer et al., 2002]:

$$\begin{aligned} c_{\text{i.ex}} &= c_{\text{i.meas}} - c_{\text{i.eq}}(S, T, p) \\ &= c_{\text{i.meas}} - c_{\text{i.atm}}(p) \cdot L_{\text{i}}(S, T) \end{aligned} \tag{2.28}$$

On account of their inertness, noble gases are well suited for the quantification of excess air. For the data analysis in this thesis (Section 4.3.2), neon is chosen as an indicator for excess air because of its low solubility and no subsurface sources.

2.2.4 Dating methods in hydrology

The *groundwater age* as described in Section 2.3 is a valuable information as it helps to understand the dynamics of the aquifer system observed. Therefore, a variety of dating methods are employed using characteristics of different tracers and processes in the atmosphere, water and biosphere [Loosli, 1983].

Generally, dating tracers can be categorized into four different dating principles (Figure 2.7) that are presented in the following.

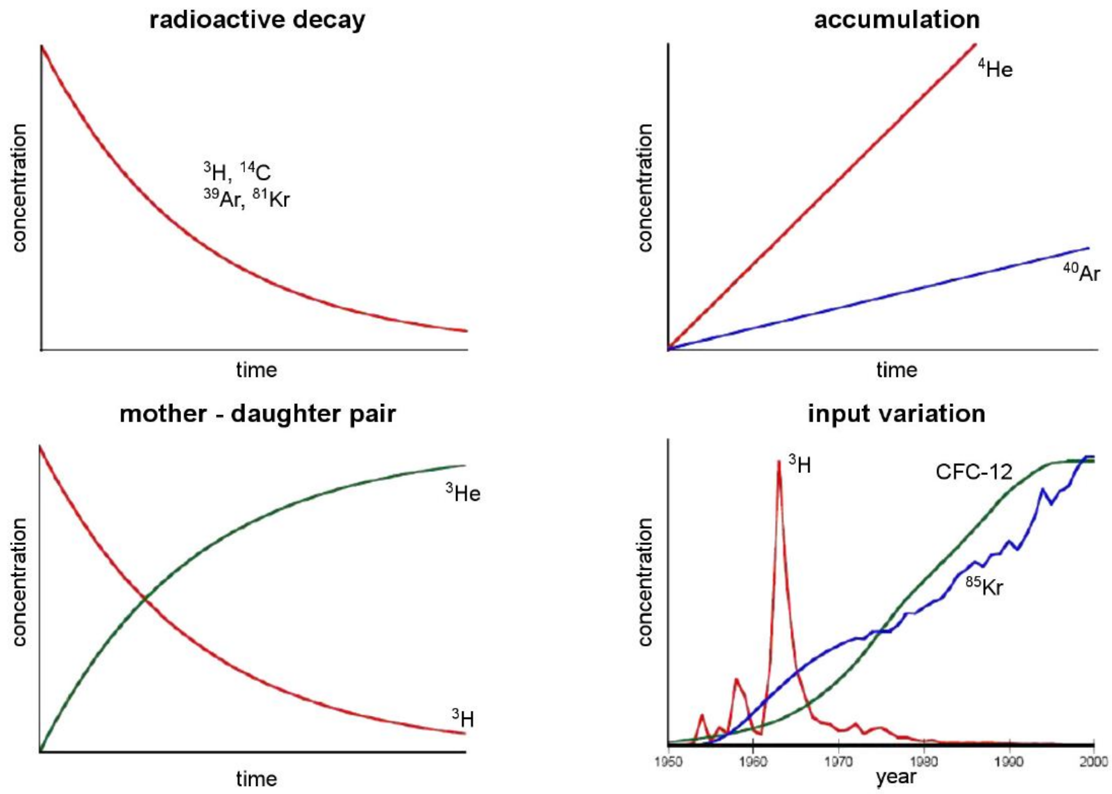

Figure 2.7: Basic principles for groundwater dating [Aeschbach, 2017].

Radioactive decay

For radioactive tracers, the known behaviour of the exponential decay is capitalized on. Assuming no subsurface production, the number of the radioactive atoms within a water parcel decreases exponentially with time from the moment it is isolated from the atmosphere. This means that in the easiest model, the atmosphere is considered the only source of the tracer. The amount N of the tracer in the water after time t is given by

$$N(t) = N_0 \cdot \mathrm{e}^{-\frac{t}{\tau}} = N_0 \cdot \mathrm{e}^{-\frac{t}{T_{1/2}} \ln(2)} \tag{2.29}$$

with N_0: initial amount of tracer
τ: mean life
$T_{1/2}$: half life

Thus, the tracer age t can be calculated by

$$t = \tau \cdot \ln\left(\frac{N_0}{N(t)}\right) = \frac{T_{1/2}}{\ln(2)} \cdot \ln\left(\frac{N_0}{N(t)}\right) \tag{2.30}$$

Note that instead of the amount of atoms N_0 and $N(t)$, the tracer concentrations in the water c_0 and $c(t)$ or activities $A_0 = \frac{dN}{dt}\big|_0$ and $A(t) = \frac{dN}{dt}(t)$ can be used. Still, it can be challenging to determine the initial condition N_0 or c_0 if the atmospheric input function is unknown.
For some tracers like ^{14}C, the atmospheric concentration (and therefore the initial water concentration c_0) cannot be assumed to be constant. In addition, subsurface production of the tracer of interest must be taken into account. Those issues will be discussed in detail for individual tracers in Section 2.2.5.

Mother-daughter pair

Mother-daughter pair dating also relies on radioactive decay of an isotope (*mother*) but additionally considers its decay product (*daughter*). Assuming zero concentration of the daughter at $t = 0$ or a known offset, all additional daughter atoms at time t can be pinned down to be a product of the radioactive decay. Taking the tritium-helium β^- decay as the most common example, with

$$^3\mathrm{H} \;\rightarrow\; ^3\mathrm{He} + \mathrm{e}^- + \bar{\nu}_\mathrm{e}, \tag{2.31}$$

this allows for a tracer age deduction of a sample independent of the tritium input function:

$$^3\mathrm{H}_0 = {}^3\mathrm{He}(t) + {}^3\mathrm{H}(t) \tag{2.32}$$

$$\rightarrow t = \tau \cdot \ln\left(\frac{^3\mathrm{He}(t)}{^3\mathrm{H}(t)} + 1\right) = \frac{T_{1/2}}{\ln(2)} \ln\left(\frac{^3\mathrm{He}(t)}{^3\mathrm{H}(t)} + 1\right) \tag{2.33}$$

The major difficulty in the tritium-helium method is the distinction between tritiogenic ^{3}H and such from other sources.

Accumulation

Subsurface production is defined as the production of isotopes by radioactive decays in the soil. Those radiogenic daughter isotopes accumulate with time. For long-lived mother isotopes, this accumulation can be mostly assumed as a linear increase. If the production and accumulation rates are known, the amount of the daughter isotope can be used to derive a groundwater age. The accumulation rate of a region can be determined by calibrating it with other dating tracers.

Input variation

While the dating principles discussed so far use geochemical tracers of natural origin, the input variation principle is based on tracers of anthropogenic origin. As the emission of those substances to the atmosphere is not constant but variable with time, a record of atmospheric concentrations is required. With Henry's law, the measured water-side concentration of a substance c_w can be used to deduce an air-side concentration c_g. As this matches the atmospheric concentration $c_\mathrm{g}(t_\mathrm{inf})$, it can be assigned to the time of infiltration t_inf. For a precise allocation, an unambiguous atmospheric input function is necessary (i.e. a constant rise). This aspect will be addressed in Section 2.2.5.
Note that in addition to a variable input function, further processes like exponential decay, subsurface production or biochemical reactions may affect the concentration of a substance in the groundwater.

2.2.5 Dating tracers applied in this study

In this section, the dating tracers used in the context of this thesis are presented. Depending on their half-lives (for radioactive tracers), their accumulation rate and the time of their input variation, the individual tracers cover different age ranges in groundwater dating. Figure 2.8 gives an overview which ranges are suitable for the tracers applied in this study.

^{4}He

For their chemical inertness, noble gases have proven to be valuable tracers in groundwater science [Aeschbach-Hertig and Solomon, 2013]. Noble gases in groundwater mainly originate from infiltration of atmosphere-equilibrated precipitation. Helium, in particular, is found as ^{3}He (relative abundance: $1,399 \cdot 10^{-6}$) and ^{4}He (relative abundance ≈ 1) [Porcelli et al., 2002]. In groundwater, ^{4}He originates from three potential sources (compare Figure 2.6): besides the equilibrium component from gas exchange with atmospheric helium, additional ^{4}He arise from excess air (see Section 2.2.3) and radiogenic production. As end member of α decays in the

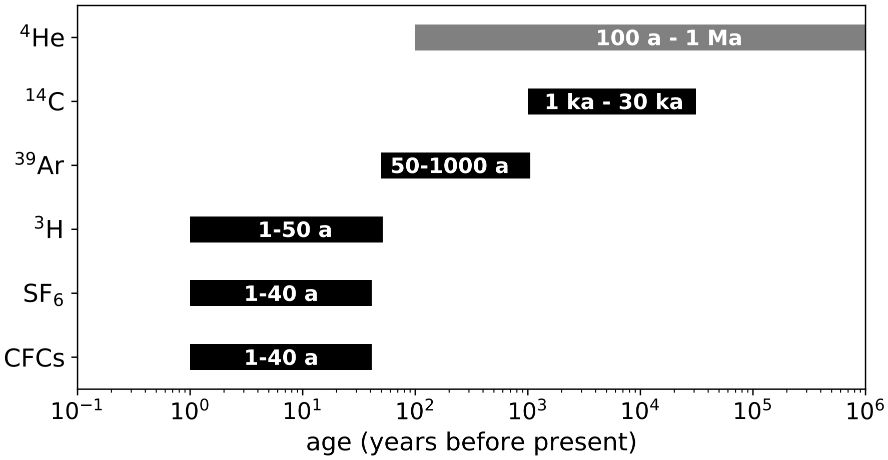

Figure 2.8: Dating ranges of the applied tracers after IAEA [2013].

U/Th decay series, the radiogenic ^{4}He component is an example for dating by accumulation of a daughter isotope. This process is assumed linear as the amount of ^{4}He released to the groundwater is dependent on the time the groundwater was in contact with the mineral and ^{238}U is constant [Solomon, 2000]. The necessity of a second tracer for the calibration of the release rate, however, restricts ^{4}He dating to qualitative considerations. In the context of this thesis, radiogenic ^{4}He levels are only adduced for comparison with other dating tracers and among different wells.

^{14}C

The radioactive isotope of carbon ^{14}C, also called radiocarbon, is produced by nuclear reactions in the upper atmosphere:

$$^{14}\mathrm{N} + \mathrm{n} \rightarrow {}^{14}\mathrm{C} + \mathrm{p} \tag{2.34}$$

$$\text{with} \quad \begin{aligned} {}^{14}\mathrm{N}: &\quad \text{nitrogen} \\ \mathrm{n}: &\quad \text{cosmic neutron} \\ \mathrm{p}: &\quad \text{proton} \end{aligned}$$

The reaction rate depends on solar activity [Crowe, 1958] and the Earth's magnetic field [Beiser, 1957]. In addition to the natural variability of ^{14}C production, anthropogenic influences can be seen in atmospheric records of the last ≈150 years. In bomb tests in the 1960s, a large number of high-energy neutrons were released into the stratosphere, causing a characteristic ^{14}C bomb peak in the atmospheric

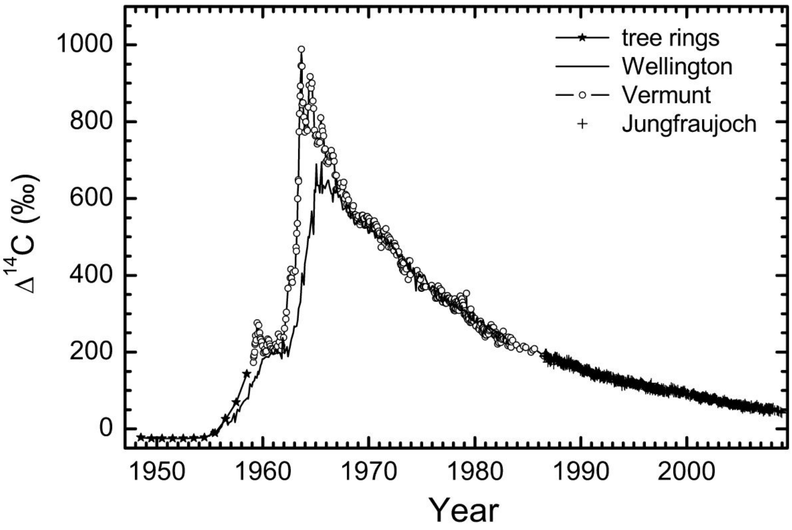

Figure 2.9: Atmospheric record of Δ^{14}C levels in the Northern (tree rings, Vermunt, Jungfraujoch) and Southern (Wellington) hemisphere. The bomb peak decays rapidly due to incorporation of carbon in the biosphere and the ocean [Levin et al., 2010b].

input function shown in Figure 2.9. After being produced, ^{14}C forms carbon dioxide ($^{14}CO_2$) with oxygen and takes part in the carbon cycle [IAEA, 2013], including gas exchange with water, photosynthetic uptake by vegetation and their decomposition into the soil.

The production of radiocarbon is balanced by its β^- decay with a half-life of (5730 ± 40) years [Godwin, 1962]:

$$^{14}\mathrm{C} \rightarrow {}^{14}\mathrm{N} + \mathrm{e}^- + \bar{\nu}_\mathrm{e}\ . \tag{2.35}$$

In addition, more changes in the atmospheric radiocarbon record are induced by anthropogenic actions: burning fossil fuels made of old decomposed organic materials releases ^{14}C - free CO_2 into the atmosphere [Suess, 1955]. The associated dilution of ^{14}C is described by the *Suess effect*.

Carbon chemistry in groundwater

All numbers and equations in the following Section were taken from Clark and Fritz [1997] if not stated otherwise.

Radiocarbon dating of groundwater is based on inorganic carbon dioxide dissolved in the water (DIC: **D**issolved **I**norganic **C**arbon). Depending on pH, it is present in different forms

$$[\mathrm{DIC}] = [\mathrm{CO_2}] + [\mathrm{HCO_3^-}] + [\mathrm{CO_3^{2-}}] \tag{2.36}$$

as chemical reactions with the water molecules occur:

$$\begin{aligned} \mathrm{CO_2} + \mathrm{H_2O} &\leftrightarrow \mathrm{H_2CO_3} \\ \mathrm{H_2CO_3} &\leftrightarrow \mathrm{HCO_3^-} + \mathrm{H^+} \\ \mathrm{HCO_3^-} &\leftrightarrow \mathrm{CO_3^{2-}} + \mathrm{H^+} \end{aligned} \tag{2.37}$$

with $\mathrm{H_2CO_3}$: carbonic acid
$\mathrm{HCO_3^-}$: hydrogen carbonate or bicarbonate
$\mathrm{CO_3^{2-}}$: carbonate

The (temperature dependent) reaction constants $\mathrm{K_i}$ are given by

$$\mathrm{K_0}(T) = \frac{[\mathrm{CO_2}]}{p_{\mathrm{CO_2}} \cdot [\mathrm{H_2O}]} = 10^{7\cdot 10^{-5}\cdot T^2 - 0.016\cdot T - 1,11} \qquad \text{(Henry's law)} \tag{2.38}$$

$$\mathrm{K_1}(T) = \frac{[\mathrm{H^+}][\mathrm{HCO_3^-}]}{[\mathrm{CO_2}]} = 10^{-1.1\cdot 10^{-4}\cdot T^2 + 0.012\cdot T - 6.58} \tag{2.39}$$

$$\mathrm{K_2}(T) = \frac{[\mathrm{H^+}][\mathrm{CO_3^{2-}}]}{[\mathrm{HCO_3^-}]} = 10^{-9\cdot 10^{-5}\cdot T^2 + 0.0137\cdot T - 10.62} \tag{2.40}$$

with $p_{\mathrm{CO_2}}$: partial pressure of carbon dioxide
$\mathrm{K_0} = {K_{\mathrm{H}}}^{-1}$: Inverse of the Henry coefficient
$\mathrm{K_1}$: first dissociation constant
$\mathrm{K_2}$: second dissociation constant

They determine the equilibrium activities[2] of the reactants and the products of

---

[2] Note that despite their compliant units, the *activity* a_{i} and *concentration* or *molality* m_{i} of a substance i in water are not the same. The activity $a_{\mathrm{i}} = m_{\mathrm{i}} \cdot \gamma_{\mathrm{i}}$ is derived using the *activity coefficient* γ, a measure for the ion strength of the water.

each chemical reaction.

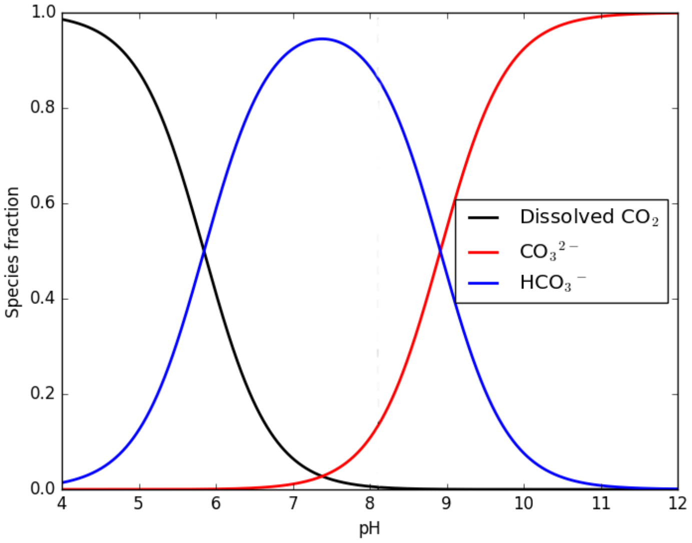

Figure 2.10: Distribution of the carbonate species in water as a function of pH at 25 ℃ [Rice, 2016].

In Figure 2.10, the relative distribution of the three carbon species in water is shown. Note that at neutral pH values (pH $\approx$ 7), the majority of the carbon is present as bicarbonate while there is effectively no carbonate, leading to the assumption

$$[\mathrm{DIC}]_{\mathrm{pH}\approx 7} \approx [\mathrm{CO_2}] + [\mathrm{HCO_3^-}] \tag{2.41}$$

Dissolution of air-side CO_2 in the water shifts the pH to lower values. As a result, available calcium carbonate (limestone) in the ground is dissolved:

$$\mathrm{H_2CO_3} + \mathrm{CaCO_3} \leftrightarrow 2\,\mathrm{HCO_3^-} + \mathrm{Ca^{2+}} \tag{2.42}$$

This behaves as a buffer system since it counteracts a further decrease in pH. The dissolving (old) $CaCO_3$ is depleted in ^{14}C with respect to the dissolved CO_2 from soil air, which is an important finding for radiocarbon groundwater dating.

Dating groundwater with radiocarbon

Dating of water with ^{14}C is challenging as many aspects have to be considered. In theory, the tracer age of a sample can be calculated with Equation 2.30 by measuring the ^{14}C activity $A(t)$. However, this ignores its variable input function as well as fractionation and geochemical processes. Therefore, a number of correction models have been postulated of which a few will be presented here.

To calculate the ^{14}C tracer age of a sample, its activity A_s is compared to the standard activity A_0 in year 1950:

$$^{14}\mathrm{C} = \frac{A_\mathrm{s}}{A_0} \cdot 100\% \quad [\mathrm{pMC}] \tag{2.43}$$

with $A_0 = 13.56 \frac{\text{decays}}{\text{min} \cdot \text{g carbon}}$: standard activity (1950) [Mook and van der Pflicht, 1999]
[pMC] : **p**ercent **M**odern **C**arbon

The **conventional carbon age** is defined as the age before 1950 (before bomb tests were performed):

$$t = \frac{T_{1/2\,(\mathrm{Libby})}}{\ln(2)} \ln\left(\frac{A_0}{A_s}\right) - (year - 1950) \tag{2.44}$$

with $T_{1/2\,(\mathrm{Libby})} = 5568 \pm 30$ years : Libby half-life [Libby, 1952]
$year$: year at the time of dating

However, for consistency, in this thesis the carbon age is given with respect to the sampling year (2018) and with the correct half-life of (5730 ± 40) years.

This does not consider reservoir effects, i.e. the dilution of ^{14}C in groundwater by dissolved calcium carbonate, and tends to overestimate the radiocarbon age. These effects are taken into account by different correction models.

The **Vogel model** is based on the empirical finding that the initial activity of ^{14}C in groundwater is not 100 pMC but a lower value, depending on the type of mineral present in the soil [Vogel, 1967]. In literature, typical values around 85%

are found. In the context of this thesis, $A_0 = (80 \pm 5)\,\mathrm{pMC}$ is used due to geological aspects.

The **Tamers model** emanates from the assumption that in a closed system, one $CaCO_3$ molecule is dissolved per bicarbonate molecule formed by dissolved CO_2 (compare Equation 2.42) [Tamers, 1975]. The measured ^{14}C activity is corrected by a factor q:

$$q_{\text{Tamers}} \equiv q = \frac{[\mathrm{CO_2}] + \frac{1}{2}[\mathrm{HCO_3^-}]}{[\mathrm{CO_2}] + [\mathrm{HCO_3^-}]} = \frac{[\mathrm{DIC}] - \frac{1}{2}[\mathrm{HCO_3^-}]}{[\mathrm{DIC}]}, \tag{2.45}$$

where q represents the fraction of atmosphere-originated CO_2. At zero age, the original radiocarbon content of the dissolved carbon species diluted by limestone is given by

$$\begin{aligned} [^{14}\mathrm{C_{meas}}]\, \mathrm{e}^{\frac{t}{T_{1/2}}\ln(2)} &= q \cdot [^{14}\mathrm{C_{modern}}] + (1-q) \cdot [^{14}\mathrm{C_{lime}}] \\ &\approx q \cdot [^{14}\mathrm{C_{modern}}] \end{aligned} \tag{2.46}$$

where the limestone is assumed to be radiocarbon-dead: $[^{14}\mathrm{C_{lime}}] = 0$.
This gives the Tamers age

$$t = \frac{T_{1/2}}{\ln(2)} \cdot \ln\left(q \cdot \frac{[^{14}\mathrm{C_{modern}}]}{[^{14}\mathrm{C_{meas}}]} \right) \tag{2.47}$$

For the calculation of q, $[\mathrm{HCO_3^-}]$ is computed using the alkalinity of the system. As elaborated in Section 2.2.1, alkalinity is deduced from titration and linked to the activity of carbon species by

$$\mathrm{Alk} \approx [\mathrm{HCO_3^-}] + 2 \cdot [\mathrm{CO_3^{2-}}]\,. \tag{2.48}$$

With Eq. 2.40, the carbonate concentration can be substituted:

$$[\mathrm{CO_3^{2-}}] = \frac{\mathrm{K_2}(T) \cdot [\mathrm{HCO_3^-}]}{[\mathrm{H^+}]}\,, \tag{2.49}$$

leading to the bicarbonate concentration[3]

$$[\mathrm{HCO_3^-}] = \frac{\mathrm{Alk}}{1+2\,\frac{\mathrm{K_2}(T)}{[\mathrm{H^+}]}}\,. \tag{2.50}$$

For the activity of aqueous carbon dioxide $[\mathrm{CO_2}]$, $[\mathrm{H^+}]$ is calculated using the pH of the sample water as described in Section 2.2.1.

After calculation of $\mathrm{K_1}$ for the respective water temperature, $\mathrm{CO_2}$ is derived using equation 2.39:

$$[\mathrm{CO_2}] = \frac{[\mathrm{H^+}][\mathrm{HCO_3^-}]}{\mathrm{K_1}(T)} \tag{2.51}$$

The Tamers model only considers a simple mixing between atmosphere-originated dissolved $\mathrm{CO_2}$ and carbon derived from dissolved carbonate minerals [IAEA, 2013]. The system is assumed to be closed, ignoring further $\mathrm{CO_2}$ exchange and isotopic fractionation during gas exchange in the soil. The latter, in particular, is an assumption that does not hold as the fractionation between soil air $\mathrm{CO_2}$ and DIC is dependent on pH.
In general, it is found that the Tamers model tends to underestimate the radiocarbon age of a sample.

The **Pearson model** corrects for the same processes as the Tamers model but instead of chemical relations, isotopic relations between ^{13}C and ^{14}C are used [Pearson JR., 1965]. Since ^{13}C is a stable isotope, the difference in δ^{13}C between soil air originated DIC and carbonate rocks is a good proxy to observe dilution processes. Any change in the ^{14}C concentration by fractionation processes will also affect the ^{13}C concentration. The correction factor is calculated by

$$q_{\mathrm{Pearson}} = \frac{\delta^{13}\mathrm{C_{DIC}} - \delta^{13}\mathrm{C_{CaCO_3}}}{\delta^{13}\mathrm{C_{soil}} - \delta^{13}\mathrm{C_{CaCO_3}}} \tag{2.52}$$

---

[3] At pH values $<$ 7, the carbonate concentration does not significantly contribute to DIC (Eq. 2.41), leading to

$$[\mathrm{HCO_3^-}] \approx \mathrm{Alk}\,.$$

This assumption is valid but not inevitable. However, it simplifies the calculation massively while only producing a relative deviation of a few % in Tamers age.

with $\delta^{13}C_{CaCO_3} \approx 0$ ‰ : ^{13}C value of dissolved calcites
$\delta^{13}C_{soil} \approx -23$ ‰ : ^{13}C value of the soil CO_2 [Clark and Fritz, 1997]
$\delta^{13}C_{DIC}$: measured ^{13}C in groundwater

In this approximation of $\delta^{13}C_{soil}$, fractionation effects are ignored. The fractionation between soil air and DIC during infiltration increases with pH due to the pH dependence of the carbon species distribution. Thus, it is recommended to measure not only $\delta^{13}C_{soil}$ but also the pH in the infiltration area. It is assumed that during infiltration, the soil water is more acidic than the (equilibrium) pH measured at the sampling site of the groundwater would indicate. Using the pH measured during sampling would produce $\delta^{13}C$ values that are considerably less depleted than the -23 ‰ estimated above. This correction will be taken into account in the results (Section 4.3.3.
Another aspect that $\delta^{13}C_{soil}$ literature values do not regard is the influence of vegetation on $\delta^{13}C_{soil}$. There are two groups of plants with respect to their isotopic fractionation during photosynthesis. C3 plants (mainly found in moderate climates like Europe and North America) produce a $\delta^{13}C$ value of approx. -28 ‰. In contrast, C4 plants are predominantly found in dry and warm climates as they have a higher water use efficiency. They fractionate with $\delta^{13}C \approx -14$ ‰ [Mook, 2002; Still et al., 2003]. In areas with similar climates to the study area (India and Saudi Arabia), both C3 and C4 plants have been identified [Ziegler et al., 1981]. However, this correction cannot be quantified and will not be used for the data of the groundwater study.

The Pearson correction factor is applied in the same way as in the Tamers model. Likewise, the Pearson model tends to overcorrect and thus, underestimate radiocarbon ages, which will be seen in the results (Section 4.3.3).

At last, it should be noted that none of the models can incorporate effects caused by the sampling itself. Thus, it is crucial to inhibit biological activity in the sample water as well as prevent atmospheric contamination.

^{39}Ar

This section is mainly based on Loosli [1983].
The radioactive isotope ^{39}Ar is produced in the stratosphere by cosmic ray induced spallation:

$$^{40}\mathrm{Ar} + \mathrm{n} \;\rightarrow\; ^{39}\mathrm{Ar} + 2\mathrm{n} \tag{2.53}$$

$$\text{with} \quad ^{40}\mathrm{Ar}: \quad \text{abundant argon isotope } (99.6\,\%)$$

In addition, there can be significant contributions from local subsurface production of ^{39}Ar in granite rock aquifers [Florkowski, 1992]:

$$^{39}\mathrm{K} + \mathrm{n} \;\rightarrow\; ^{39}\mathrm{Ar} + \mathrm{p} \tag{2.54}$$

As atmospheric mixing happens on much smaller time scales than the β^- decay

$$^{39}\mathrm{Ar} \;\rightarrow\; ^{39}\mathrm{K} + \mathrm{e}^- + \bar{\nu}_\mathrm{e}\ , \tag{2.55}$$

the tropospheric isotopic abundance $^{39}\mathrm{Ar}/\mathrm{Ar} = 8,23 \cdot 10^{-16}$ can be assumed homogeneous. This ratio is used as input concentration and defines the 100 % modern value [pMAr]. Over the last 1000 years, variations of this ratio were estimated to be up to 7 %, based on ^{14}C fluctuations in tree rings. In summary, those aspects yield a well-known atmospheric reference.
With its half-life of (269 ± 3) years [Stoenner et al., 1965], ^{39}Ar is the only reliable tracer suited to date waters in the age range between 50 and 1000 years. As a noble gas, it is not involved in geochemical processes and no fractionation processes need to be considered. Although its inertness make ^{39}Ar an ideal conservative tracer, the extremely low isotopic abundance has hampered its routine application in environmental science. The problem of detecting ^{39}Ar will be addressed in Section 2.4.
Analogous to Section 2.2.4, age determination with ^{39}Ar is done assuming the atmosphere to be the only source. Once having infiltrated into groundwater, no further gas exchange is assumed and the ^{39}Ar amount decreases exponentially. In some groundwater applications, however, subsurface production has to be taken into account. It has predominantly been observed in thermal waters from granitic rocks. The neutrons required for reaction 2.54 originate from α particles and spontaneous fission in the ^{238}U decay chain [Andrews et al., 1989]. The neutron production and

the diffusion of potassium into groundwater are dependent on the type of rock; for instance, crystalline environments like granite have shown a higher proneness than sandstone. Therefore, geological information and the U/Th content can serve as a proxy for subsurface production. Corrections have be made using ^{37}Ar levels in the water [Loosli et al., 2000].

CFCs

CFCs (**C**hloro**f**luoro**c**arbons) are inert gases of anthropogenic origin. The organic compounds are composed of carbon, chlorine and fluorine (compare Figure 2.11). Produced since the early 20th century, they mainly served as refrigerants [Walker et al., 2000]. In 1987, after it became clear that rising atmospheric CFC levels cause a depletion of the Earth's protective ozone layer, they were restricted by the *Montreal Protocol* [Molina and Rowland, 1974].

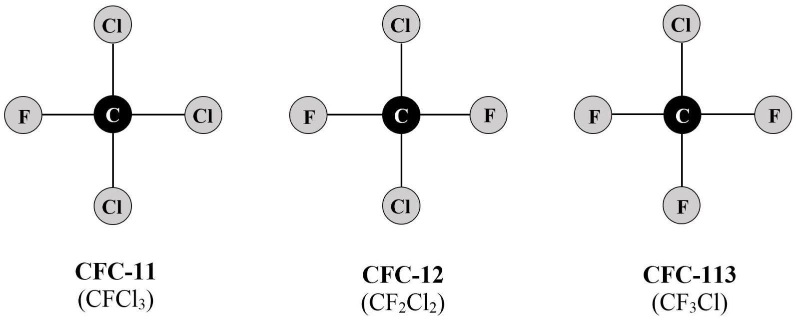

Figure 2.11: Chemical structure of CFC-11, CFC-12 and CFC-13.

Despite their negative impacts on the atmosphere, CFCs have proven valuable traits essential for hydrological dating tracers. As seen in Figure 2.12, their atmospheric input functions show unique levels for long periods of time in the last century. Their conservative behaviour in water allows for a conversion of the concentrations dissolved in water into an atmospheric concentration at the respective time of infiltration. Measurements are done by gas chromatography, where the gas is split into its compounds in a column filled with a specific adsorbent.

For dating of very young waters, additional dating tracers like SF_6 have to be consulted as two different possible tracer ages exist for a given concentration. Another difficulty of dating with CFCs is their susceptibility to contamination, among others by sampling equipment [IAEA, 2006]. In industrial areas, high levels of CFCs are found, e.g. in the vicinity of dump sites of chlorinated substances [Kinzelbach et al., 2002]. Under anaerobic conditions in the soil, CFC-11 (and CFC-12, to a lower extent) values in groundwater may be depleted due to microbial degradation [Bauer and Yavitt, 1996].

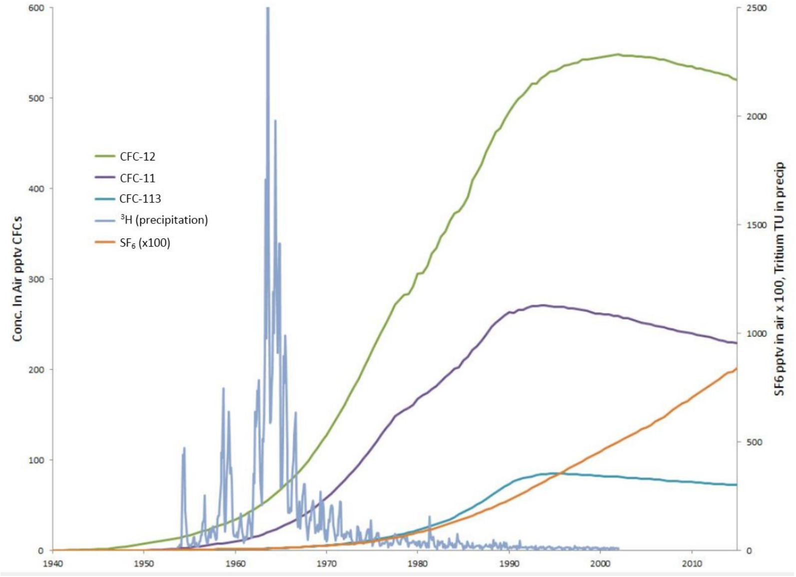

Figure 2.12: Atmospheric concentrations of CFC-11, CFC-12, CFC-113 and SF_6 (Northern Hemisphere). CFC and $SF_6 \cdot 100$ concentrations are given in parts per trillion by volume (pptv), ^3H in precipitation is given in Tritium Units (TU) [USGS, 2017].

SF_6

Sulfur hexafluoride (SF_6, compare Figure 2.13) is a stable, nonreactive trace gas with a greenhouse gas potential of 23 000 x CO_2. Produced for industrial use since the 1950s, e.g. as insulation gas in switchgear, the atmospheric SF_6 concentration has since increased by two orders of magnitude. Once released to the atmosphere, it remains there with an extremely long atmospheric lifetime of about 3200 years [Maiss and Brenninkmeijer, 1998].

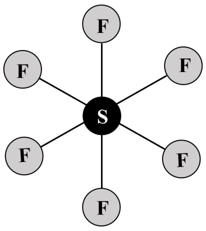

Figure 2.13: Chemical structure of SF_6.

In 1997, SF_6 was included in the *Kyoto Global Warming Protocol Agreement*, obliging all countries to report their emissions to the *United Nations Framework Convention on Climate Change* (UNFCCC). Nevertheless, Levin et al. [2010a] found that emissions derived from atmospheric measurements exceeded the reported amounts by a factor of > 2. The atmospheric concentrations in volumetric parts per trillion (pptv), magnified by factor 100, is found in Figure 2.12. In contrast to CFCs, SF_6 levels are still rising. For dating purposes, this is of advantage in so far as the input function is unique with respect to time. The dating procedure is similar to CFC dating. For groundwater applications, potential subsurface SF_6 production in fluoride-containing rocks has to be considered [Harnisch et al., 2000]. In addition, due to its low solubility (compare Figure 2.5), SF_6 is very susceptible to excess air.

2.3 Transit time distributions

To characterize the subsurface flow and to gain insight into the dynamics of an aquifer system, the *groundwater age* is a parameter of importance. The idealized groundwater age is defined as the time elapsed between the entering of water into the saturated zone and the sampling at a distance downstream within the groundwater system [IAEA, 2013]. However, this *transit time* usually cannot be considered a distinct value. While the *tracer age* or *apparent age* describes a purely advective flow, water movement also results from (longitudinal and transversal) dispersion. Within a sampled water volume, the single water elements originate from different flow lines and have therefore spent a different amount of time in the subsurface. To account for those different ages and quantify the composition of a water mixture, age distributions or ***T**ransit **T**ime **D**istributions (TTDs)* are employed.

Mathematically, TTDs act as a transfer function on an (aqueous) input concentration $c_{\text{in}}(t')$ of a tracer. For tracers with an additional (time-dependent) exponential decay, the output concentration $c_{\text{out}}(t)$ can be written as a convolution [Aeschbach, 2017]:

$$c_{\text{out}}(t) = \int_{-\infty}^{t} c_{\text{in}}(t') \cdot g(t-t') \cdot \mathrm{e}^{-\gamma(t-t')} dt' \, . \tag{2.56}$$

with t : time of sampling
t' : time of infiltration
$t - t'$: groundwater age
$g(t - t')$: distribution of groundwater ages (TTD)
γ : decay constant of radioactive tracer

For a known atmospheric history (resulting in an aqueous input concentration $c_{\text{in}}(t')$) and a measured output concentration $c_{\text{out}}(t)$, the hydrological system can be treated as a 'black box' between input and output. It is described by the Green's function $g(t - t')$ accounting for the relative contributions of waters with ages $t - t'$ and satisfies

$$\int_{-\infty}^{t} g(t - t')\, dt' = 1 \ . \tag{2.57}$$

Transit time distributions are characterized by a ***M**ean **R**esidence **T**ime (MRT)* τ:

$$\tau = \int_{-\infty}^{t} (t - t') \cdot g(t - t')\, dt' \tag{2.58}$$

When modelling groundwater ages from tracer data with a modelling software, the calculated MRTs depend on the chosen TTD. In the following, example TTDs and underlying assumptions on the water body are explained.

Piston-Flow Model (PM)

In the most simplified assumption, the ***P**iston-Flow **M**odel (PM)*, any kind of mixing is neglected. Only one flow line is considered, meaning that the water parcels are transported by a purely advective flow (compare Figure 2.14). In practice, this would only a reasonable approximation for wells with a well defined recharge area and a screen with infinitesimal extent.

The output concentration corresponds to the input concentration shifted by the age $t - t' = \tau$. The transfer function $g(t - t')$ in the PM model equals a δ-distribution with apparent age = MRT = τ:

$$\begin{aligned} c_{\text{out}}(t) &= \int_{0}^{\infty} c_{\text{in}}(t') \cdot \delta(t - t' - \tau) \cdot \mathrm{e}^{-\gamma(t-t')}\, d(t - t') \\ &= \ c_{\text{in}}(t - \tau) \cdot \mathrm{e}^{-\gamma\tau} \end{aligned} \tag{2.59}$$

The PM model usually does not describe the flow properties in an adequate manner as it ignores dispersion, mixing of waters, the broadness of the recharge area and the screen expanse of the sampling well.

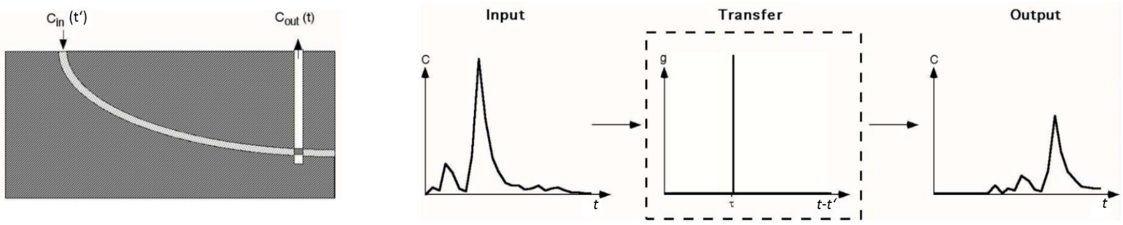

Figure 2.14: Piston-Flow Model. Left: Cross section of the aquifer. Only one flow line contributes to the sampled water. Right: The δ-distribution shifts the input function by the MRT τ [Aeschbach, 2017].

Exponential model (EM)

The ***E**xponential **M**odel (EM)* is used for so called *Vogel aquifers* [Vogel, 1968], meaning unconfined aquifers with homogeneous recharge and porosity over the entire aquifer area and a sampling screen expanding from the bottom to the top of the aquifer (compare Figure 2.15). In contrast to the Piston-Flow Model, mixing is taken into account. All flow lines are considered, with a higher contribution of young waters (originating from recharge areas close to the well) than old waters (originating from recharge areas far away). At the very bottom of the well, the age of the water is assumed to tend towards infinity. The weight of the input events decreases exponentially with age [Aeschbach, 2017], giving the (normalized) transfer function

$$g(t-t') = \frac{1}{\tau}\,\mathrm{e}^{-\frac{t-t'}{\tau}} \tag{2.60}$$

$$\text{with} \quad \tau: \quad \text{MRT in the mixed system}$$

The output concentration is derived by

$$\begin{aligned} c_{\text{out}}(t) &= \int_0^\infty c_{\text{in}}(t') \cdot \frac{1}{\tau}\,\mathrm{e}^{-\frac{t-t'}{\tau}} \cdot \mathrm{e}^{-\gamma(t-t')}\,d(t-t') \\ &= \int_0^\infty c_{\text{in}}(t') \cdot \frac{1}{\tau} \cdot \mathrm{e}^{-(\gamma+\frac{1}{\tau})\cdot(t-t')}\,d(t-t') \end{aligned} \tag{2.61}$$

The EM is suitable for oceanic surface waters, lakes or shallow aquifers. However, for aquifers with limited screen depth it tends to give young waters too high a weight.

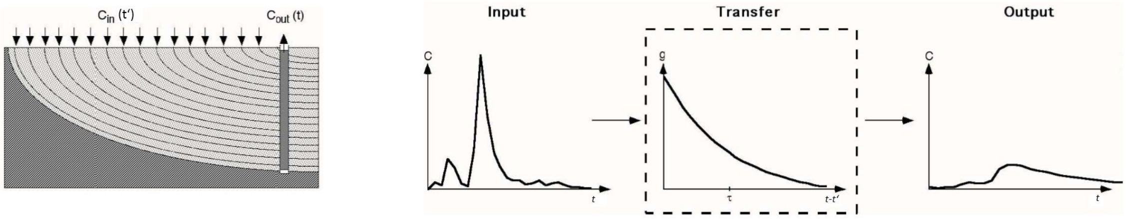

Figure 2.15: Exponential Model. Left: Cross section of the aquifer. All flow lines contribute to the sampled water. Right: The exponential transfer function gives young waters a higher weight than older waters [Aeschbach, 2017].

Dispersion model (DM)

The model of choice for this thesis is the ***Dispersion Model (DM)***. It can be seen as a combination of the two previous models as it describes a flow system with (limited) mixing due to dispersion. The input events are weighted in an asymmetric Gauss distribution, with the highest contribution for a certain input time t' and decreasing contributions for younger and older inputs [Aeschbach, 2017]:

$$g(t-t') = \sqrt{\frac{Pe \cdot \tau}{4\pi(t-t')^3}} \cdot \mathrm{e}^{-\frac{Pe\cdot(t-t'-\tau)^2}{4\pi(t-t')}} \tag{2.62}$$

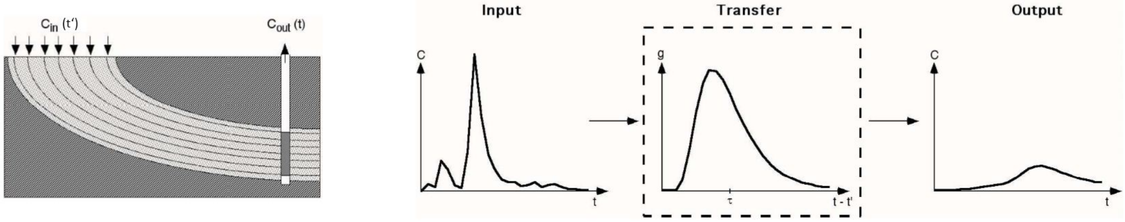

Figure 2.16: Dispersion Model. Left: Cross section of the aquifer. Only a part of the flow lines contribute to the sampled water. Right: The transfer function comprises both advection and mixing [Aeschbach, 2017].

In contrast to the PM and the EM, the Dispersion Model requires a second parameter to describe the flow. The *Peclet Number Pe* is a measure for the ratio of advection and dispersion. In Figure 2.17, the effect of different Peclet numbers on the (normalized) age distribution with MRT = 50 years can be seen. For high Peclet numbers the distribution tends towards a δ peak, corresponding to the Piston-Flow Model. On the other hand, very low Peclet numbers (indicating a prevalence of dis-

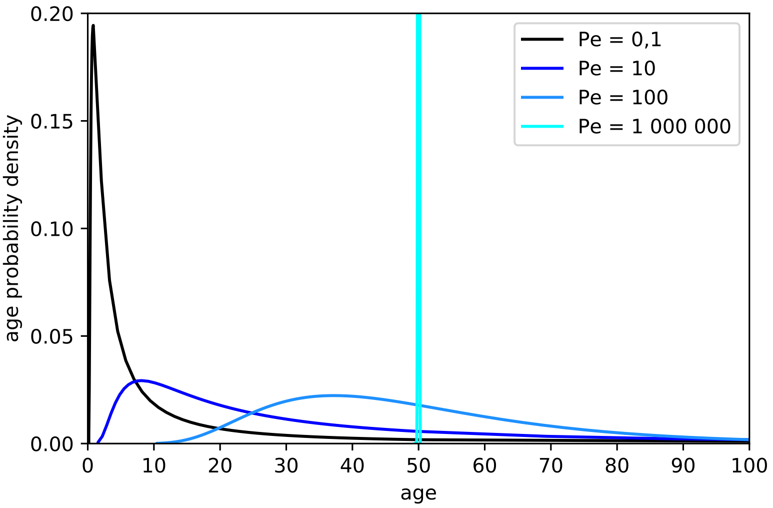

Figure 2.17: Age probability density in the Dispersion Model for different Peclet numbers, with constant MRT = 50 years (curves generated with the software *Lumpy*).

persion) produce a curve with a maximum close to zero. Thus, the Peclet number determines the tendency of the Dispersion Model towards the PM. Scale analysis by Gelhar et al. [1992] constrained the Peclet number in groundwater flow to $Pe \approx 10$ which will be used throughout this thesis.

Mixing of waters

While Transit Time Distributions account for water mixing processes due to different flow paths and velocities, the mixing of several distinct water components cannot be characterized by a (continuous) distribution. Examples for those processes are the addition of an old, tracer free component causing a dilution, or a young (atmospheric) component increasing the tracer concentration. While old waters may originate from underground reservoirs, young water components are often of anthropogenic origin, like infiltrated wastewater or irrigation.

The mixing of two distinct water masses, each with a respective TTD, can be simulated in a Lumped-Parameter modelling software (e.g. Lumpy). Here, the fraction of the respective water masses A and B and their parameters (e.g. temperature, salinity, MRT and, if necessary, Peclet number) are employed as follows:

$$c_{\text{mix}} = (1-r) \cdot c_{\text{A}}(T, S, \text{MRT}, Pe, ...) + r \cdot c_{\text{B}}(T, S, \text{MRT}, Pe, ...) \tag{2.63}$$

with r : ratio of model B in mixture
c_{mix} : measured tracer concentration in sample
c_{A}, c_{B} : (modeled) tracer concentration of water mass A, B

By disentangling the water mixture, the correct MRT of the component of interest can be calculated, as applied in section 4.3.4.

2.4 Argon Trap Trace Analysis (ArTTA)

As mentioned in Section 2.2.5, the low isotopic abundance combined with the relatively long half-life poses a problem for the measurement of ^{39}Ar. While low-level counting and Cyclotron Atomic Mass Spectrometry have been administered successfully [Loosli, 1983; Collon et al., 2004], large required sample amounts and high costs have as yet hindered its application. With the rise of **Ar**gon **T**rap **T**race **A**nalysis (ArTTA) based on the atomic optical technique **A**tom **T**rap **T**race **A**nalysis (ATTA) [Chen et al., 1999], new potentials have been unlocked with respect to routine sampling feasibility in groundwater, oceans and ice [Ritterbusch et al., 2014; Ebser et al., 2018; Feng et al., 2018]. As this technique does not rely on the decaying portion of ^{39}Ar but uses optical methods addressing all ^{39}Ar atoms, the required sample size was reduced markedly.

Based on repetitive resonant laser photon-atom interactions, the ArTTA technique provides a high degree of selectivity for ^{39}Ar [Collon et al., 2004]. As the difference in mass alters its resonance frequencies (isotope shifts), the rare isotope can be distinguished clearly from the 10^{15}-times more abundant ^{40}Ar. Laser cooling allows to selectively decelerate and capture ^{39}Ar while ^{40}Ar can pass unaffected.

Many steps of the ArTTA technique make use of laser cooling, meaning the reduction of atom velocity in a certain direction. While the resonant atoms in the system receive a directed momentum from laser photons in laser-atom interactions, they emit photons isotropically. For the argon atoms, this results in a net change of momentum directed parallel to the laser beam. This principle is made use of in the collimator, the **M**agneto-**O**ptical **L**ens (MOL), the **Z**eeman **SL**ower (ZSL) and the **M**agneto **O**ptical **T**rap (MOT).

As shown in Figure 2.18, a sample consisting of different argon isotopes is introduced into the source. Here, ^{40}Ar and ^{39}Ar atoms are equally excited to a metastable

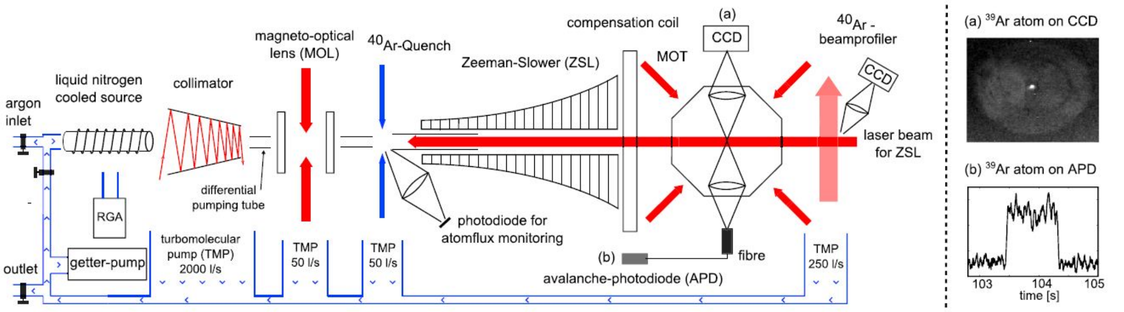

Figure 2.18: Schematic of the ArTTA aperatus, with (a) a CCD image and (b) an APD signal of a trapped ^{39}Ar atom [Ritterbusch et al., 2014].

state by a radio frequency plasma cooled by liquid nitrogen, with efficiency $\approx 10^{-4}$. A divergent beam of atoms with mean velocity $\approx 280\,\mathrm{m/s}$ leaves the source. It is first collimated by transverse laser cooling in a tilted mirror setup where transverse atom velocities are reduced via photon momenta. Then, the beam is further focused with a MOL [Ritterbusch et al., 2014]. In the next step, the ^{40}Ar atoms are deexited from the metastable state by ^{40}Ar - quench laser light to avoid background fluorescence light in the MOT. The quench is isotope selective, so the ^{39}Ar atoms remain unaffected. During deexcitation to the ground state, each ^{40}Ar atoms emits one fluorescence photon which is detected by a photo diode to monitor the atom flux [Ebser, 2018]. In the Zeeman Slower, the ^{39}Ar atoms are longitudinally slowed down [Ritterbusch et al., 2014]. The Doppler shift is compensated for by an external magnetic field so the atoms are at any time resonant with the cooling laser. Finally, the ^{39}Ar atoms reach the MOT. They are captured by resonant scattering with $\approx 10^6$ photons and kept in the center of the MOT for up to half a second. An external magnetic field is used to ensure resonance for atoms off the center. The spontaneous emission of fluorescence photons by captured ^{39}Ar atoms is monitored by a CCD camera (Figure 2.18a) and an **A**valanche **P**hoto **D**iode (APD) (Figure 2.18b). The APD signal can identify single ^{39}Ar atoms.

The measured count rate R_{sample} is compared to a reference sample of known ^{39}Ar concentration (tenfold of the atmospheric concentration). This gives the the ^{39}Ar concentration c_{sample} in **p**ercent **m**odern **ar**gon (pMAr):

$$c_{\text{sample}} = \frac{R_{\text{sample}}}{0.1 \cdot R_{\text{ref}}} \quad [\text{pMAr}] \tag{2.64}$$

ArTTA is run in recycle mode, meaning that after passing through the system, the gas is reintroduced into the source. This reduces the required argon amount drastically, so only a typical sample size of 2 mL pure argon is needed [Ebser, 2018].

3 Methods

3.1 Sampling

For the groundwater campaign in Oman, a variety of preparations were necessary. Appropriate sample containers and techniques were chosen and prepared for the different tracers. Once arrived in Salalah, a few last preparations had to be done before the sampling was carried out. At the sampling sites, power for the *Grundfos MP1* submersible pump was supplied by a gasoline fueled generator. After lowering and fastening the pump in the well (Figure 3.1a), the water volume in the well was extracted three times to prevent atmosphere-equilibrated water from contamining the samples. For each well, A and B samples were taken for four different analysis methods. The sampling equipment can be seen in Figure 3.1b).


(a)

(b)

Figure 3.1: a) Construction to fixate both the cable of the pump and the water hose. b) Equipment for sampling of CFCs/SF_6, noble gases, ^{14}C and ^{39}Ar.

In this chapter, the standard sampling methods used for CFCs/SF_6, noble gases and field parameters are described in short. In the following, the new sampling techniques of ^{14}C and ^{39}Ar are presented, as well as their purification methods. Finally, improvements of the argon purification setup carried out in the scope of this thesis are delineated.

3.1.1 Conventional sampling methods

In this section, the sampling methods for CFCs/SF_6, noble gases and the field parameters are described. Since standard techniques are concerned, only a brief overview is given.

Sampling procedure for CFCs/SF_6 and noble gases

For the analysis of both CFCs and SF_6, groundwater is sampled in 500 mL stainless steel cylinders with Swagelok valves (compare Figure 3.2 a). For noble gas sampling, crimped copper tubes with stainless steel clamps are used (Figure 3.2 b).

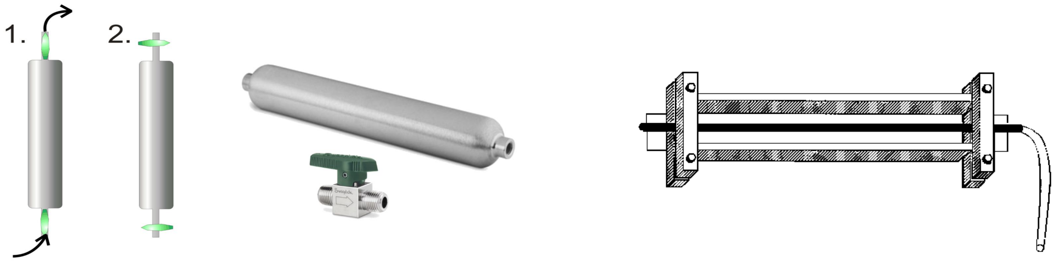

(a) (b)

Figure 3.2: Sketch of sampling equipment for a) CFCs and SF_6 (Swagelok cylinder) [Klement, 2005] [Swagelok] b) noble gases (copper sample tube) [USGS, 2017].

Both sampling techniques involve a flushing of the sample containers prior to sampling. In addition, it is important to assure that no air bubbles are entrapped inside. Therefore, the containers are knocked against with a solid tool. When contaminations can be ruled out, the Swagelok valves are closed (CFCs/SF_6, Figure 3.3 a) or else the screws of the clamps are tightened (noble gases, Figure 3.3 b).

(a) (b)

Figure 3.3: a) Knocking against a CFCs/SF_6 cylinder to release air bubbles. b) Tightening screws to close the copper tubes in noble gas sampling.

The CFCs and SF_6 concentrations are derived using gas chromatography (GC). A headspace in the sample containers is generated and introduced into a GC system where it is flushed through a separation column by a stripper gas. The gases exit the column after characteristic time delays and can therefore be identified. A detailed description of the technique can be found in Schneider [2014]. The CFCs/SF_6 samples were measured by Harald Oster at the Spurenstofflabor in Wachenheim/Weinstraße, Germany.

The concentrations of noble gas isotopes are measured using mass spectrometry. At first, the reactive gases are removed using a getter pump. The remaining gases are ionized, accelerated by an electric field and separated according to their charge-to-mass ratio. Details are described in Schneider [2014]. The noble gas measurements were performed by Florian Freundt at the Institute of Environmental Physics, University of Heidelberg.

Sampling procedure for field parameters

Before sampling for tracer analysis, the field parameters are measured for each well. Monitoring their stability during well purging also serves as a measure for the water's atmospheric contamination. Typically, the values show a trend throughout the pumping process but remain constant at the point when all air-equilibrated water has been removed. The values monitored in this campaign were **temperature, O_2 content, electric conductivity, pH** and **redox value**.

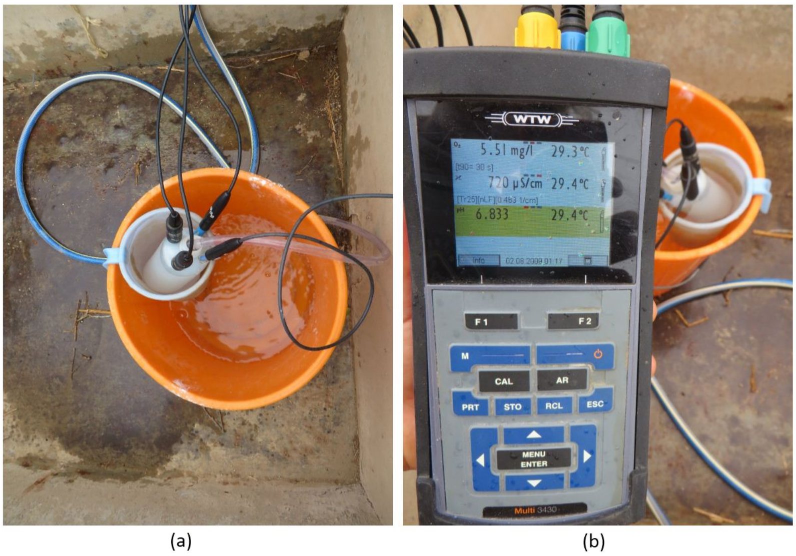

(a) (b)

Figure 3.4: Setup for measuring the field parameters (temperature, O_2 content, electric conductivity, pH and redox value).

The four sensors of the *WTW 3430 portable meter* are immersed in a bucket supplied with water from the well (Figure 3.4). Values are noted down throughout the well purging process. For parameters relevant for calculations in this thesis, the value measured just before the start of the sampling is used. With the electric conductivity, the salinity is calculated as described in Section 2.2.1. The salinity, the sampling temperature and pH are used for calculations of the tracer ages in Section 4.3.3.

3.1.2 Sampling for ^{14}C

The sampling for ^{14}C during this campaign was the first application of a newly developed technique at the Institute of Environmental Physics [Speicher, 2018]. With this method, higher CO_2 extraction yields can be achieved than with conventional methods while the handling is less prone to errors and contamination. A key factor is the rubber sealing which remains on the bottle throughout the whole process of cleaning, sampling and extraction. By stabbing a cannula through the rubber, a very controlled pathway into and out of the bottle is created.

Preparation of the sample containers

Before closing the 100 mL glass bottle with the rubber lid, a stirring magnet is placed inside. To avoid biological activity in the water sample, 0.4 mL of $AgNO_3$ (silver

Figure 3.5: Left: Evacuating C_{14} bottles with cannulas pinched through the rubber lid. Center: For ^{14}C sampling, a glass bottle is placed in a bucket flushed with sample water and filled through a cannula. Right: Water samples immediately after sampling (right bottle) and after 5 minutes (left bottle).

nitrate) solution are added (compare Wieser [2011]) using a syringe and cannula. Then the bottles are evacuated to about 10^{-1} mbar (Figure 3.5, left) and heated with a heat gun to quicken the crystallization of the silver nitrate. Subsequently, the bottles are flushed with nitrogen through two needles as described in Speicher [2018]. This procedure of evacuating and flushing is done twice before the bottles are shipped to the sampling location filled with about 1 bar of N_2. There they are evacuated to about 1.4 mbar the night before sampling.

Sampling in the field

During sampling for ^{14}C analysis it is important to rule out any atmospheric contamination. Therefore, a bucket is filled with water from the well and flushed throughout the whole sampling process. The hose is placed at the bottom. The evacuated glass bottle is held upside down close to the opening of the hose. A cannula, preliminary flushed with sample water using a syringe, is introduced through the rubber lid and the glass bottle is filled with sample water (Figure 3.5, center). After the sampling is done, a change in colour is visible (compare Figure 3.5, right) due to chemical reactions of $AgNO_3$ with sunlight. However, this does not affect the ^{14}C values.

3.1.3 Sampling for ^{39}Ar

As described in Section 2.4, a few mL of pure argon are sufficient to measure ^{39}Ar with ArTTA. Therefore, a 12.2 L steel bottle, usually used for propane gas, is chosen as water sample container [Beyersdorfer, 2016]. The bottles have to be prepared prior to the campaign. To optimize the argon yield, the ideal ratio between water and head space is calculated. This result can be used in the field as an estimate for the amount of water sampled.

Preparation of the sample containers

Similar to the ^{14}C bottles, the argon containers are cleaned prior to the sampling in order to prevent atmospheric contamination. This is done with a three-way setup connecting a nitrogen bottle, a vacuum pump and the sample container. The containers are evacuated down to 1 mbar and then filled with nitrogen up to about 1.5 bar. If the sample containers have been used before, a water trap with a mixture of dry ice and isopropyl is integrated. This procedure is done twice before the bottles are shipped to the sampling location, filled with nitrogen at pressures of around 1.5 bar. The night before sampling they are evacuated to about 1.5 mbar. A detailed consideration of the remaining atmospheric contamination is found in Section 4.3.3.

Calculation of the ideal sample to head space ratio for multiple equilibration cycles

Before sampling groundwater with propane bottles, a theoretical consideration of the ideal trade-off between sample volume V_w and head space V_{air} has to be made. While a high water fraction yields high argon amounts, only little argon is present in a small head space and thus, many equilibration cycles would be necessary, significantly increasing the time needed.

In this section, the following abbreviations are used:

c_{atm} : atmospheric argon concentration
V_{w} : volume of sampled water
$c_{\text{w.0}}$: initial argon concentration dissolved in the sampled water
$V_{\text{Ar.w.0}}$: initial argon volume dissolved in the sampled water
$c_{\text{w}}(t)$: current argon concentration dissolved in the sampled water
$V_{\text{Ar.w}}(t)$: current argon volume dissolved in the sampled water
$V_{\text{h}}(t)$: current volume of headspace
$c_{\text{h}}(t)$: current argon concentration in headspace
$V_{\text{Ar.h}}(t)$: current argon volume in headspace

According to Henry's law (Eq. 2.18), the argon concentration in the sampled water volume V_{w} is:

$$c_{\text{w.0}} = c_{\text{atm}}\; L\left(T_{\text{inf}}\right) \tag{3.1}$$

with the atmosperic argon concentration $c_{\text{atm}} = 0.934\,\%$ [Porcelli et al., 2002]. The Ostwald solubility at different temperatures $L(T)$ can be derived using Weiss [1970]. In the infiltration area and the Heidelberg laboratory, this leads to typical values given in Table 3.1.

	Temperature	L
laboratory	20 ℃	0.03412
infiltration	24 ℃	0.03180
	26 ℃	0.03077
	28 ℃	0.02981

Table 3.1: Ostwald solubility of argon at typical temperatures in the laboratory and in the infiltration area. Values taken from Weiss [1970].

In the closed bottle, the headspace and the water phase equilibrate. The argon concentration c_{h} in the headspace volume V_{h} follows Henry's law:

$$c_{\text{h}}(t) = \frac{c_{\text{w}}(t)}{L(T_{\text{lab}})} \tag{3.2}$$

with temperature in the laboratory T_{lab}. With

$$c_{\text{w}}(t) = \frac{V_{\text{Ar.w}}(t)}{V_{\text{w}}}$$

and

$$c_{\text{h}}(t) = \frac{V_{\text{Ar.h}}(t)}{V_{\text{h}}}$$

this yields:

$$V_{\text{Ar.h}}(t) = \frac{V_{\text{h}}}{V_{\text{w}}} \frac{V_{\text{Ar.w}}(t)}{L(T_{\text{lab}})} \tag{3.3}$$

The remaining argon in the water is

$$\begin{aligned} V_{\text{Ar.w}}(t) &= V_{\text{Ar.w.0}} - V_{\text{Ar.h}}(t) \\ &= c_{\text{w.0}}\, V_{\text{w}} - V_{\text{Ar.h}}(t) \end{aligned} \tag{3.4}$$

with initial argon volume solved in the water $V_{\text{Ar.w.0}}$. Combining Eq. 3.3 and 3.4 to

$$V_{\text{Ar.h}}(t) = \frac{V_{\text{h}}}{L(T_{\text{lab}})} \left(c_{\text{w.0}} - \frac{V_{\text{Ar.h}}(t)}{V_{\text{w}}} \right). \tag{3.5}$$

results in the equilibrated headspace argon yield $V_{\text{Ar.h}}$:

$$\begin{aligned} V_{\text{Ar.h}} &= \frac{V_{\text{Ar.w.0}}}{L(T_{\text{lab}})\frac{V_{\text{w}}}{V_{\text{h}}} + 1} \\ &= \frac{c_{\text{w.0}}}{\frac{L(T_{\text{lab}})}{V_{\text{h}}} + \frac{1}{V_{\text{w}}}} \\ &= \frac{c_{\text{atm}}\, L\left(T_{\text{inf}}\right)}{\frac{L(T_{\text{lab}})}{V_{\text{h}}} + \frac{1}{V_{\text{w}}}} \end{aligned} \tag{3.6}$$

Figure 3.6 shows the argon yield in dependence of the sampled water volume for typical infiltration temperatures. Expected temperature values were taken from noble gas temperatures by Thomas Müller, UFZ.

A higher argon yield can be achieved in multiple equilibration processes inbetween which the equilibrated headspace is extracted from the bottle. Anticipating

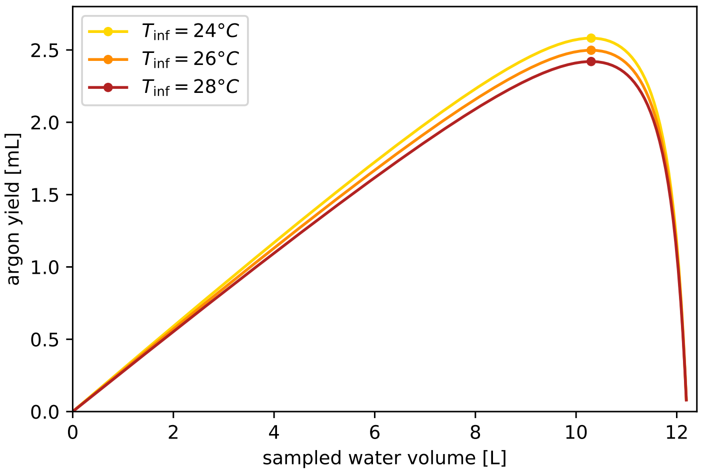

T [°C]	V_{sample} [L]	$V_{\text{Ar.max}}$ [mL]
24	10.3	2.58
26	10.3	2.50
28	10.3	2.42

Figure 3.6: Argon yield after one degassing iteration for different sampled water volumes and infiltration temperatures. Maximum values for each temperature are listed in the Table besides.

a full equilibration of the headspace after each iteration and taking into account the diminishing argon content in the water phase, a recursion for the argon yield can be derived. For simplicity it can be assumed that during the extraction of the equilibrated gas phase, no gas exchange between water phase and headspace takes place.

In the following, $V_{\text{Ar.tot.i}}$ and $V_{\text{tot.i}}$ denote the total argon amount extracted after the i-th iteration, meaning the sum of the individual iteration yields $V_{\text{Ar.h.i}}$. After iteration i, $V_{\text{Ar.w.i}}$ denotes the remaining argon content in the water phase which then determines the initial water-side argon concentration for iteration i+1.

After the first iteration, the remaining argon content in the water is

$$\begin{aligned} V_{\text{Ar.w.1}} &= V_{\text{Ar.w.0}} - V_{\text{Ar.h.1}} \\ &= V_{\text{Ar.w.0}} - V_{\text{Ar.tot.1}} \\ &= V_{\text{Ar.w.0}} \left(1 - \frac{V_{\text{Ar.tot.1}}}{V_{\text{Ar.w.0}}}\right) . \end{aligned} \tag{3.7}$$

With $V_{\text{Ar.w.1}}$ being the new initial water-side argon content in Eq. 3.6, the headspace argon content in the second iteration is

$$\begin{aligned} V_{\text{Ar.h.2}} &= \frac{V_{\text{Ar.w.0}}}{L(T_{\text{lab}})\frac{V_{\text{w}}}{V_{\text{h}}}+1}\left(1-\frac{V_{\text{Ar.tot.1}}}{V_{\text{Ar.w.0}}}\right) \\ &= V_{\text{Ar.h.1}}\left(1-\frac{V_{\text{Ar.tot.1}}}{V_{\text{Ar.w.0}}}\right) \end{aligned} \tag{3.8}$$

Thus, the total argon amount extracted after iteration 2 is

$$\begin{aligned} V_{\text{Ar.tot.2}} &= V_{\text{Ar.h.1}} + V_{\text{Ar.h.2}} \\ &= V_{\text{Ar.h.1}} + V_{\text{Ar.h.1}}\left(1-\frac{V_{\text{Ar.tot.1}}}{V_{\text{Ar.w.0}}}\right) \end{aligned} \tag{3.9}$$

After the second iteration, the remaining argon content in the water is

$$\begin{aligned} V_{\text{Ar.w.2}} &= V_{\text{Ar.w.0}} - V_{\text{Ar.h.1}} - V_{\text{Ar.h.2}} \\ &= V_{\text{Ar.w.0}} - V_{\text{Ar.tot.2}} \\ &= V_{\text{Ar.w.0}}\left(1-\frac{V_{\text{Ar.tot.2}}}{V_{\text{Ar.w.0}}}\right) \qquad , \end{aligned} \tag{3.10}$$

leading to the headspace argon content $V_{\text{Ar.h.3}}$ in the third iteration:

$$\begin{aligned} V_{\text{Ar.h.3}} &= \frac{V_{\text{Ar.w.0}}}{L(T_{\text{lab}})\frac{V_{\text{w}}}{V_{\text{h}}}+1}\left(1-\frac{V_{\text{Ar.tot.2}}}{V_{\text{Ar.w.0}}}\right) \\ &= V_{\text{Ar.h.1}}\left(1-\frac{V_{\text{Ar.tot.2}}}{V_{\text{Ar.w.0}}}\right) \end{aligned} \tag{3.11}$$

The cumulative argon yield after three iterations then becomes

$$\begin{aligned} V_{\text{Ar.tot.3}} &= V_{\text{Ar.tot.2}} + V_{\text{Ar.h.3}} \\ &= V_{\text{Ar.tot.2}} + V_{\text{Ar.h.1}}\left(1-\frac{V_{\text{Ar.tot.2}}}{V_{\text{Ar.w.0}}}\right) \end{aligned} \tag{3.12}$$

In general, the total argon yield after i iterations can be expressed as

$$V_{\text{Ar.tot.i}} = V_{\text{Ar.tot.i}-1} + V_{\text{Ar.h.1}}\left(1-\frac{V_{\text{Ar.tot.i}-1}}{V_{\text{Ar.w.0}}}\right) \tag{3.13}$$

$$\tag{3.14}$$

In Figure 3.7, the extractable argon volume for different numbers of iterations is plotted as a function of the sampled water volume. Numbers are given in Table 3.2. The argon yield after i iterations in % can be calculated using

$$\text{argon yield}_\text{i}\ [\%] = \frac{V_\text{Ar.tot.i}}{V_\text{Ar.w.0}} \cdot 100\ . \tag{3.15}$$

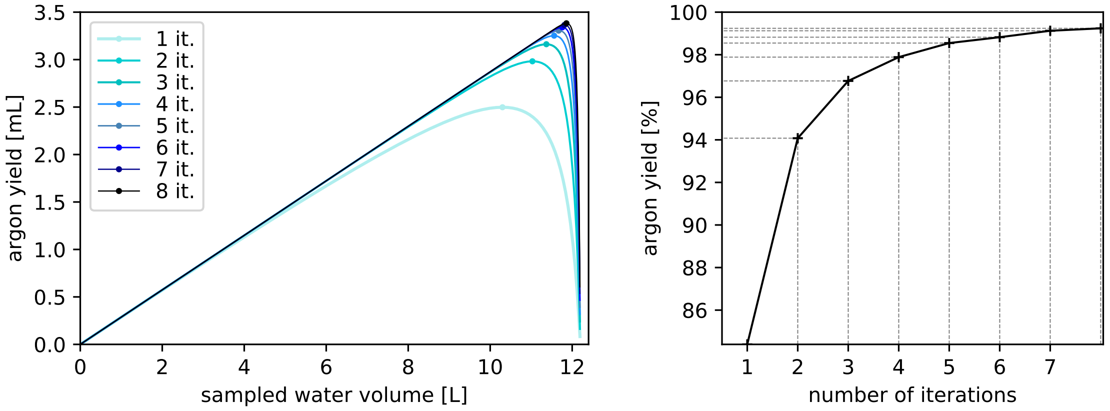

Figure 3.7: Left: argon yield for different numbers of iterations i, plotted against the sampled volume with $T_\text{inf} = 26\,°\text{C}$. Right: Maximum argon yield plotted against the number of iterations.

iterations	V_sample [L]	$V_\text{Ar.max}$ [mL]	argon yield [%]
1	10,30	2,50	84,4
2	11,03	2,98	94,1
3	11,37	3,16	96,8
4	11,56	3,25	97,9
5	11,67	3,31	98,5
6	11,76	3,34	98,8
7	11,81	3,36	99,1
8	11,86	3,38	99,2

Table 3.2: Ideal sample volume, extractable argon volume and achievable argon yield for $T_\text{inf} = 26\,°\text{C}$and $T_\text{lab} = 20\,°\text{C}$.

Sampling in the field

To avoid atmospheric contamination during sampling, a new sampling technique was applied. The self-built 3-way brass adapter is seen in Figure 3.8 on the left. It includes a screw-nut fitting the opening of the propane gas bottle and two adapters for hoses. As depicted in the center of Figure 3.8, the first hose is connected to the pump in the well delivering the sample water while the second hose serves as an outlet. With this setup, the hose and the inlet volume can be flushed while the propane valve remains closed. After this is done, the valve is opened and the evacuated bottle fills with sample water. During the sampling, it is important to monitor the outlet hose to ensure that a portion of the water always exits there. The outlet hose is placed in a way that no air bubbles from the outlet can reach the propane gas bottle (e.g. by coiling it like in Figure 3.8 on the right). This constitutes a tool to prevent any back flow of atmospheric air into the sample container.

The amount of water in the bottle is estimated using analogue scales set to *tare* when starting the sampling. When the ideal weight derived in Section 3.1.3 is reached, the valve of the bottle is closed. After removing the brass adapter, a brass cap with rubber sealing shown on the left in Figure 3.8 is screwed onto the bottle opening. Although the propane gas bottles have been tested to be leak tight [Hopkins, 2018], this provides additional security.

Figure 3.8: Left: Self-built 3-way adapter for sampling of ^{39}Ar into propane gas bottles and brass cap with rubber sealing. Center: An inlet and an outlet hose are connected to the sample container. Right: Sampling of ^{39}Ar.

3.2 Sample purification

After the sampling is done, the sampled water is degassed. The extracted gas volume is then purified to measure the concentration of the individual tracers.
First, the purification steps for analysis of ^{14}C are described. In the following section, sample purification of argon for ^{39}Ar measurement is outlined.

3.2.1 Purification of carbon

This section describes the necessary preparation steps in the laboratory for the analysis of ^{14}C. Those include the generation of a headspace, the extraction of carbon dioxide and graphitizition. Detailed descriptions can be found in Speicher [2018].

Headspace generation

Before the sample is degassed a headspace has to be generated in the ^{14}C glass bottles. Thus, a part of the sample is removed from the bottle and replaced by nitrogen. This is done by connecting a syringe and a nitrogen bottle to the sample bottle by a three-way valve. A needle is introduced half-way into the rubber septum and the syringe is filled with about 30 mL STP of nitrogen. Subsequently, the inlet of the nitrogen bottle is closed and the glass bottle is turned upside down. The needle is pierced entirely through the rubber lid. The syringe is pushed and pulled to inject nitrogen into the bottle and pull water out.
To dissolve ^{14}C in the headspace, 2 mL of hydrochloric acid (5-molar HCl) are added. This is done by introducing a needle connected to a syringe into the glass bottle through the rubber lid.

Extraction of carbon dioxide

Before carbon dioxide is extracted from the headspace, a needle connected to the extraction line is introduced half-way into the rubber lid and the whole extraction setup is evacuated to about 10^{-2} mbar. The extraction line can be seen in Figure 3.9a. After closing all valves, the needle is pushed completely through the rubber lid into the glass bottle. A water trap is cooled by a mix of dry ice and acetone. All valves are re-opened and for 45 minutes, the headspace is extracted while a stirring magnet enhances the outgassing (Figure 3.9b). CO_2 is captured in a liquid nitrogen cooled trap. After extraction, the CO_2 is pumped from the trap to a liquid nitrogen cooled finger. This is done by thawing the CO_2 trap in an acetone - dry ice mixture increasing the temperature.

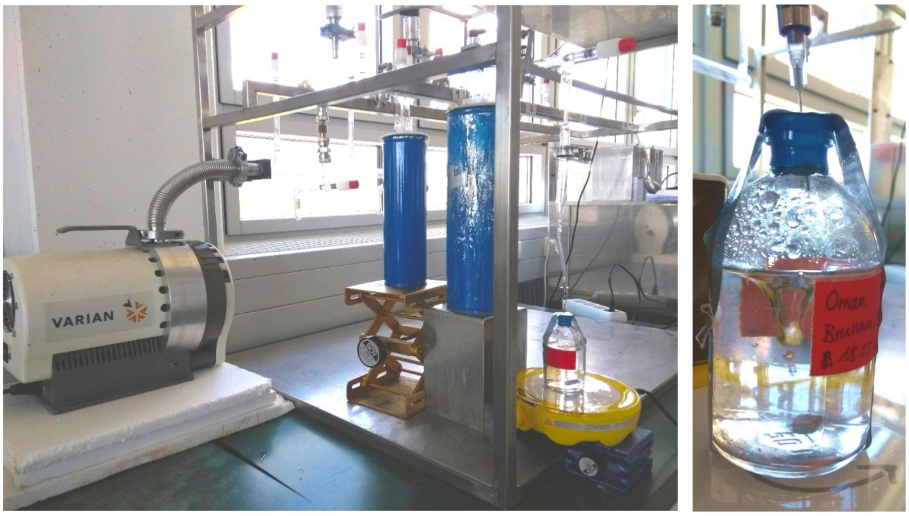

(a) (b)

Figure 3.9: a) Extraction line with a pump, a finger, a CO_2 trap, a water trap and a connected sample bottle. b) A stirring magnet helps to degas the sample.

Graphitization

To measure ^{14}C with accelerator mass spectrometry (AMS), the extracted CO_2 needs to be reduced to carbon. In a process called *graphitization*, the carbon dioxide undergoes two reactions with hydrogen:

$$\mathrm{CO_2 + H_2 \rightarrow CO + H_2O} \tag{3.16}$$

$$\mathrm{CO + H_2 \rightarrow C + H_2O} \tag{3.17}$$

The reaction is catalysed by iron in the form of powder and takes place in up to 6 parallel heated reaction chambers (Figure 3.10a).

The entire graphitization setup is evacuated prior to extracting the gaseous CO_2 from the fingers. The carbon dioxide sample and the respective required amount of hydrogen are injected into the reaction chamber. The calculation of the ratio can be found in Unkel [2006]. The duration of the reduction to carbon depends on the sample size. Typically, after 2 to 3 hours the iron and carbon are stored in small glass vials depicted in Figure 3.10b. After this procedure the samples are ready for ^{14}C measurement with AMS.

(a)

(b)

Figure 3.10: a) Six samples can be graphitized in parallel reaction chambers. b) The graphetized samples are stored in small glass vials.

3.2.2 Purification of argon

The sampled argon is purified for the measurement with ArTTA. On account of ideal sample volume considerations outlined in Section 3.1.3, no further headspace generation step is necessary for the extraction and purification of argon from the water samples. This section describes the extraction of the headspace as well as the purification procedure of argon. Details can be found in Hopkins [2018].

Extraction of the gas volume

To extract the headspace of the water sample, the propane gas bottle is mounted to a cradle and connected to the inlet of the argon purification line (compare Figure 3.11). A shaking device constructed by Beyersdorfer [2016] is used to induce turbulence within the water and expedite the equilibration between the water and the gas phase. Before the valve of the sample container is opened, the system is evacuated and a liquid nitrogen (LN) cooled water trap is installed. Subsequently, the valve is opened and for about 45 minutes, the gas is captured in an LN cooled **A**ctivated **C**harcoal **T**rap (ACT). Pressures in the order of 10^{-1} mbar are reached. To quantify the total extracted gas volume, the valve of the sample bottle is closed again and the ACT is heated to 150 °Cusing an induction heating device constructed by Hopkins [2018]. Using a calibration factor (compare Section 3.3.1), the measured pressure is converted into a gas volume (usually a few hundred mL). The gas composition is analyzed with a **Q**uadrupole **M**ass **S**pectrometer (QMS).

Purification of argon

The extracted gas is purified by removing all reactive gases. The residual noble gases virtually consist of pure argon.

Purification is done by *gettering* in titanium sponge getters. The first getter is heated to 900 °C to activate the getter material and enhance the reactivity of the surface. As oxides and nitrides diffuse into the inner of the sponge material, the surface is free to bind all reactive gases except for hydrogen [Ferrario, 1996]. The latter is adsorbed in a second getter at room temperature. This is a reversible process, so the hydrogen is released if the second getter is heated to temperatures higher than 400 °C.

The residual noble gases are frozen into an ACT (Figure 3.11 on the left). Depending on the initial gas composition, this process takes between one and three hours. Finally, the valves to the getters are closed and the ACT is heated out. The measured pressure is converted into a volume using calibration curves by Hopkins [2018]. Using a QMS, the composition of the residual gases is analyzed. In the last step, the argon is frozen into a sample container ACT which is connected to the ArTTA apparatus for the measurement of ^{39}Ar (described in Section 2.4).

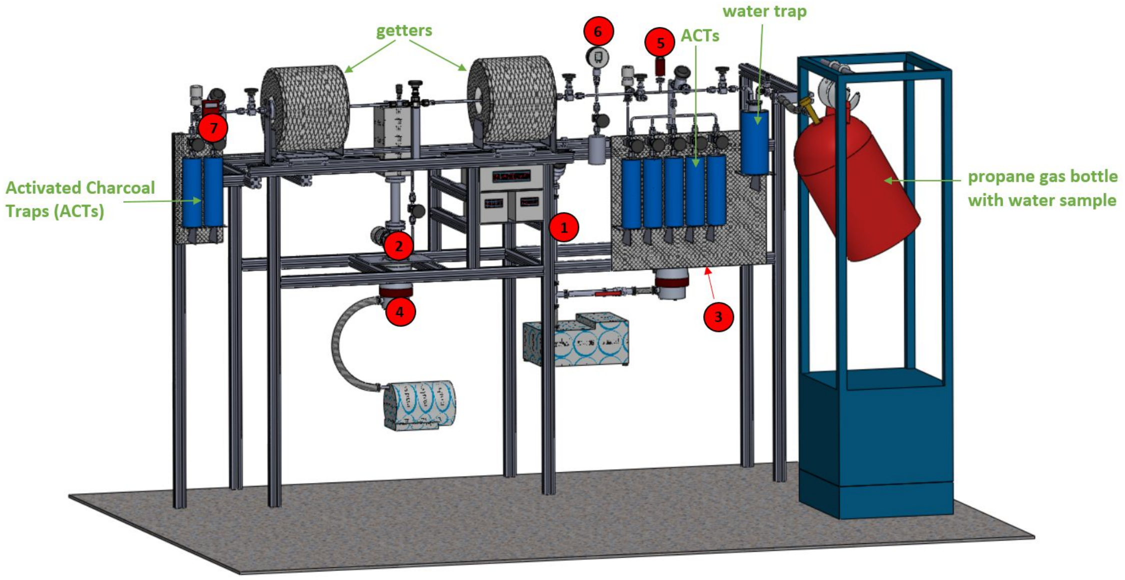

Figure 3.11: SolidWorks sketch of the argon purification setup with the 7 pressure readout locations indicated in red [Beyersdorfer, 2016].

3.3 Improvements of the argon purification setup

In the context of this thesis, several projects aiming to improve the laboratory procedures were carried out. In this section the calibration of pressures for small gas samples is described. In addition, a Labview program was written to automate the pressure readout and management.

3.3.1 Calibrations for volume estimation of small gas samples

To estimate the gas volume before and after gettering, the pressure has to be converted into a gas volume. The gas is stored in ACTs and heated out in a designated volume in the purification setup. For this section, only the right part of the setup in Figure 3.11 is of importance. The volumes were calibrated by Hopkins [2018] as follows:

$$\begin{aligned} V_\mathrm{i} &= (53.60 \pm 0.07)\,\mathrm{mL}: && \text{inner volume on the inlet side} \\ V_\mathrm{C} &= (351.75 \pm 1.58)\,\mathrm{mL}: && \text{calibrated additional volume} \\ V_\mathrm{i+C} &= (405.35 \pm 1.58)\,\mathrm{mL}: && \text{sum of both volumes} \end{aligned}$$

In addition to the inner volumes, the pressure-volume conversion factors including volumes of the ACTs have to be determined. This was done for the volume $V_\mathrm{i+C}$ by Hopkins [2018]. However, for small amounts of gas it is preferable to leave the additional calibrated volume V_C closed. Hence, a calibration curve heating out an ACT in V_i was measured. This was done for ACT 5 only as it is currently the only ACT in use. The calibration procedure is described in the following.

Air is let into one of the three inner volumes of the purification setup mentioned above (V_i, V_C or $V_\mathrm{i+C}$) and the pressure p_0 is noted down. The product of those two numbers yields the amount of gas. The gas is frozen into an ACT and the rest of the system is evacuated. The ACT is heated out in $V_\mathrm{i+ACT}$ at 150 °Cand the pressure is measured using the Lex pressure gauge (sensor 6 in Figure 3.11). Hence, the value $p_\mathrm{i+ACT}$ can be assigned to a gas amount. This is done for different amounts of gas and the results are plotted in Figure 3.12. The error of the gas amount is derived by error propagation of uncertainties of the inner volumes and the pressure measurement uncertainty. A linear fit (with intersects set to zero) yields the calibration curve and the proportionality factor $b_\mathrm{i+ACT} = 0.1286\,\frac{\mathrm{mL}}{\mathrm{mbar}}$.

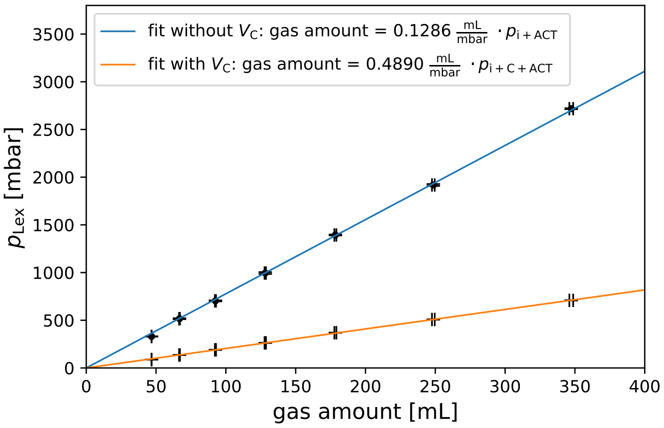

Figure 3.12: Calibration curve of pressures at different gas amounts with and without the additional volume V_C.

To derive the uncertainty Δb_{i+ACT} and verify the calibration by comparison with existing values, the additional volume V_C is opened so the gas expands into the volume $V_{i+C+ACT}$. The pressure $p_{i+C+ACT}$ is measured and fitted linearly (Figure 3.12). The resulting proportionality factor of $b_{i+C+ACT} = 0.4890\,\frac{mL}{mbar}$ is significantly smaller than the value determined by Hopkins [2018] ($b_{i+C+ACT} = 0.5053 \pm 0.0009\,\frac{mL}{mbar}$) although both values were determined with the same method. Hence, the reproducibility of the pressure-volume conversion is limited and the error is larger than expected. The uncertainty of both proportionality factors is set to $0.01\,\frac{mL}{mbar}$, yielding

$$b_{i+ACT} = (0.1286 \pm 0.0100)\,\frac{mL}{mbar} \tag{3.18}$$

$$b_{i+C+ACT} = (0.4890 \pm 0.0100)\,\frac{mL}{mbar}\ , \tag{3.19}$$

which are the values implemented in the program described in the following section.

3.3.2 Automation of the pressure readout

In the context of this thesis, a *Labview* program was designed in order to allow for an easier application of the extraction setup. The aim was to read out and control 7 pressure sensors indicated in Figure 3.11.

As a computer program encompasses many details and steps, this section only gives an overview over the components. The Labview block diagram is shown in Figure 6.1 in the Appendix.

Sensors and communication The seven pressure sensors are controlled by three pressure gauges. Sensors 1 - 5 in Figure 3.11 are centralized in the *Pfeiffer Vacuum TPG 256 Vacuum Gauge Controller*. Sensor 6 is a *Keller Lex 1* and sensor 7 is a *Pfeiffer Vacuum TPG 202 Piezo/Pirani Handheld Vacuum Gauge*. Hence, one program has to include the communication with three control units from now on abbreviated as Maxigauge, Lex and TPG. The controllers are connected to the computer through serial ports and are displayed as COM inputs. In the user interface depicted in Figure 3.13, the control units for communication setup can be selected individually (using the `Lex data`, `TPG data` and `Maxigauge data` buttons).
In the Labview front panel, the user specifies the COM port numbers of the individual controllers. As the controllers tend to interfere, the communication with the Lex has to be established before the other two controllers. Thus, a timed structure is applied where the Lex is initialized and parameters like the baud rate, a timeout value and data bit format are specified. The status of the Lex is imparted to a global variable before the Maxigauge and the TPG are initialized.

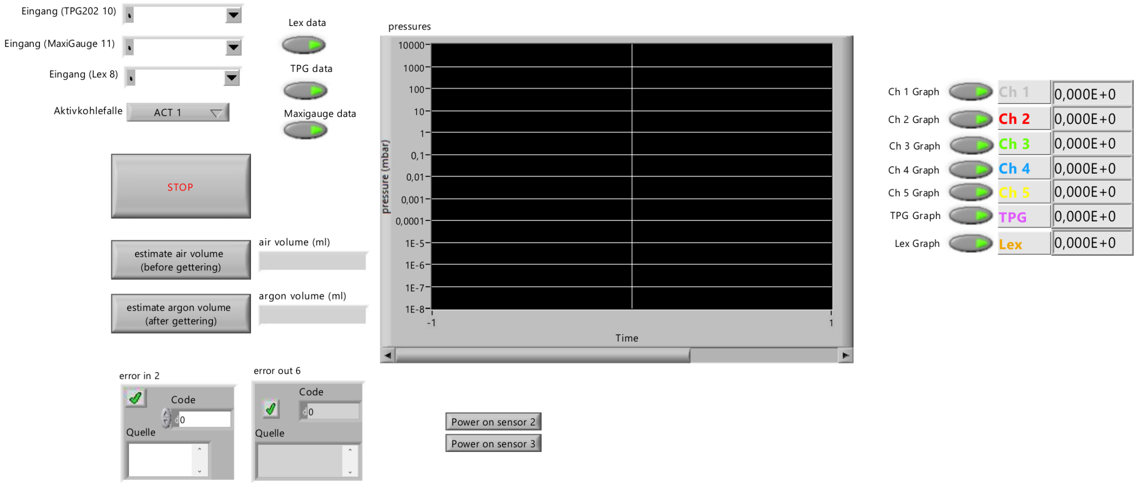

Figure 3.13: Labview front panel of the pressure automation program.

Receive, display and save data Once the computer is able to receive data from the pressure gauges, a measurement file in .txt format is created. The path and the file name are specified by the user in a pop-up window. While the measurement is running, the received data are written into the text file with one line per while-loop iteration. Hence, in case of a program crash, all data are saved.
The measurement itself is proceeded by Labview Sub-VIs (**V**irtual **I**nterfaces) that

collect the values sent by the pressure gauges. Those data are displayed on the right in Figure 3.13 where `Ch X` stands for channels 1 - 5 as denoted in the purification setup above. Using the `Ch.X Graph` buttons, the data displayed in the alongside graph can be selected. This is of particular use as the pressure data encompass values differing by 10 orders of magnitude. As the scale is adjusted automatically, monitoring small pressure changes in the graph is not feasible if pressures in a far out range are plotted simultaneously.
While the pressure values for the data display and the graph are passed over as numbers of type `double`, they are converted into `strings` before writing them to the .txt file. Without this conversion, alignment characters assigning the values to their respective columns in the document could not be used.

Time data In Labview, the function `Get date/time stamp` outputs the current date and time as a string. However, it is useful to not only know the time in HH:MM:SS format but the amount of time since starting the measurement. This can only be done in an indirect way as 'current time' functions in Labview return the time elapsed since Friday, January 1st, 1904 at 12:00 a.m. Hence, the Labview function `Tick Count (ms)` is placed once outside the `while loop` to remember the starting point of the measurement and once inside to collect the current time for each measurement. Subtraction of those two data leads to the time elapsed since the measurement was started.
Generally, about every one to two seconds, a data point is recorded. The speed of the program depends on the number of pressure control units it communicates with.

Volume conversions As described in Section 3.2.2, the gas volume is estimated both before and after gettering. This is done by converting the measured pressure into a volume using a proportionality constant (compare Section 3.3.1). In the Labview program, this can be done by selecting `estimate air volume (before gettering)` or `estimate argon volume (after gettering)`, respectively. Clicking those buttons sets off a case structure with a linear conversion using the proportionality factors determined by Hopkins [2018] (in $\frac{\mathrm{mL}}{\mathrm{mbar}}$):

$$\begin{aligned} b_1 &= 0.5018 \pm 0.01 \\ b_2 &= 0.5076 \pm 0.01 \\ b_3 &= 0.5134 \pm 0.01 \\ b_4 &= 0.5057 \pm 0.01 \\ b_5 &= 0.4890 \pm 0.01^1 \\ b_{\mathrm{Ar}} &= 0.03276 \pm 0.00002 \end{aligned}$$

where the numbers indicate the ACT on the right side in Figure 3.11 and b_{Ar} stands for the ACT on the left side where the gas mainly consists of argon.
In addition, for small gas samples it is possible to leave the additional volume V_{C} closed (compare Section 3.3.1). This option can be selected by the user and the proportionality constant used by Labview is

$$b_5 = 0.1286 \pm 0.01 \, \frac{\mathrm{mL}}{\mathrm{mbar}} \ .$$

The results of the volume estimations are not only displayed in the front panel but written in the current data line (in an individual column) in the .txt file.

Multiple ACTs As the effective volumes of the individual ACTs differ, the program needs to offer the possibility to select the used ACT for the `estimate air volume (before gettering)` calculation. The user can specify this in the drop-down menu `ACT X` (compare Figure 3.13). The selection in the `Ring enum` can be processed in two ways. The first possibility is a case structure with 5 cases with the same calculation involving different proportionality factors. In the second method the 5 proportionality factors are included in an array and the selection controls which element is processed in the calculation. As the second method requires less computing capacity, it was realized for the program. In addition to the choice of pressure-volume conversion, the ACT number is written down in the header of the data document.

---

[1] This value is determined in Section 3.3.1.

Alarms Several pressure gauges are applicable for a certain pressure range only and need to be protected from pressures exceeding their tolerance limit. This applies for the Penning pressure sensors 2 and 3 and for the Lex. The program was designed taking into account the tolerated pressure ranges and includes an alarm system to warn the user when the pressure reaches critical values. This is done by a `case structure` with an audible alarm set off if a certain threshold is exceeded. Those were specified for the respective pressure gauge as follows:

$$\begin{aligned}\text{Channel 2}: \quad p_{\text{alarm}} &= 0.0001\,\text{mbar}\\ \text{Channel 3}: \quad p_{\text{alarm}} &= 0.0001\,\text{mbar}\\ \text{Lex}: \quad p_{\text{alarm}} &= 2500\,\text{mbar}\end{aligned}$$

This step helps the user to intervene given the pressure rises slow enough for the user to react. However, for fast pressure jumps, the program needs to be able to operate without involving the user.

Automatic shutdown In case of an immediate pressure jump the program has to shut down sensors that may be damaged. This is only possible for Maxigauge sensors, i.e. Channels 2 and 3 are concerned. If a threshold p_{shutdown} is exceeded, a code is passed over to the `Maxigauge driver core` inducing it to switch off the respective sensor. It is important to mention that if a sensor is inactive, a value of $p = 0.02\,\text{mbar}$ is read by the computer. Hence, this pressure value has to be excluded from the pressure analysis. The threshold pressures are chosen as follows:

$$\begin{aligned}\text{Channel 2}: \quad p_{\text{shutdown}} &= 0.001\,\text{mbar}\\ \text{Channel 3}: \quad p_{\text{shutdown}} &= 0.001\,\text{mbar}\end{aligned}$$

The `Maxigauge driver core` is not only able to shut down a sensor but also to switch it on again. Pressing the buttons `Power on sensor X` releases the respective code to the `Maxigauge driver core`. However, during rebooting, the sensor displays numbers starting from the default value $p = 0.02\,\text{mbar}$ and approaching the actual pressure. Although this only takes about two seconds, pressures above the shutdown threshold are identified during this time interval and the program immediately switches the sensor off again. Hence, a `wait` function is interposed stalling the program execution for about 2.5 seconds.

Design Generally, programming poses the challenge to produce a code that is clearly expressed and unambiguous. Due to the graphical interface of Labview, this aspect is of great importance for the usability of the program. A way to leave the interface neatly arranged is to use several layers by conflating a set of commands in a SubVI. On the other hand, this exacerbates the possibility to understand the program at a glance.

The pressure automation program was designed using SubVIs for communication processes, i.e. the initialization, the driver core, sensor status and data transmission are organized in sublayers. At the same time, all processes that need to be understood by the user as data processing, volume estimation and pressure thresholds are seen in the main interface. This guarantees that a user unfamiliar with the program is able to understand the relevant processes.

Future projects The program described in this section works and is applied on a frequent basis. However, some improvements can still be implemented. A handy tool would be a cursor readout in the pressure plot. While current pressure values are always displayed on the right, the user is not able to receive exact pressure values at other points of time at a glance. However, the currently used function `waveform chart` does not support cursor readout. Instead, a `waveform graph` is required. In contrast to a `waveform chart` which displays received data in addition to already existing points, this function plots all received points at once and the data are passed over in an array. Due to complications with data formats, including a `waveform graph` in the existing program structure has not been possible up to date.

In addition, the pressure gauge automation is not the only component of the purification setup controlled by the computer. The mass spectrometer used to analyze the gas composition before and after gettering is operated using a computer software. Implementing the mass spectrometer control unit into the pressure automation Labview program would facilitate the application considerably. In particular, it would require notably less time to teach the purification procedure to new users. However, the handling of the mass spectrometer with Labview is very complicated and could not be implemented.

4 Groundwater study in the Salalah Plain, Oman

The area of interest is the Salalah Plain located in Southern Oman. Extensive groundwater abstraction for irrigation has shown a negative impact on the water quality. Seawater intrusions are posing a threat on the warrant of freshwater availability. To motivate the present groundwater study, aspects of the water consumption in the Salalah Plain, the water budget and the hydrogeology of the aquifer are delineated in Section 4.1. In the course of this thesis, a groundwater study in the Salalah Plain (Oman) was planned and realized which is described in Section 4.2. The sampled water was measured using different tracer techniques. The data analysis is found in Section 4.3 and the results are interpreted in Section 4.4. At last, environmental and technical influences on the results are discussed in Section 4.5.

4.1 Motivation

The city of Salalah is located in the southernmost district of Oman, the governorate of Dhofar. With a population of 165 000 inhabitants, it ranks the second biggest city in Oman after the capital Muscat [World population review, 2018]. As depicted in Figure 4.1, the Salalah Plain forms a coastal enclave, with the Dhofar mountain range in the North and the Arabian Sea in the South.

Water consumption and supply in the Salalah Plain Throughout the last decades, the Sultanate of Oman has experienced a tremendous population growth, and its current growth rate of about 9 % is one of the largest in the world [World population review, 2018]. To satisfy the concomitant increase of agricultural demands and food self-sufficiency plans, efforts have been made to enhance the productivity and improve the structure of agriculture since 1990. Within 20 years, Oman's agricultural sector almost doubled in terms of economic value. As major parts of the

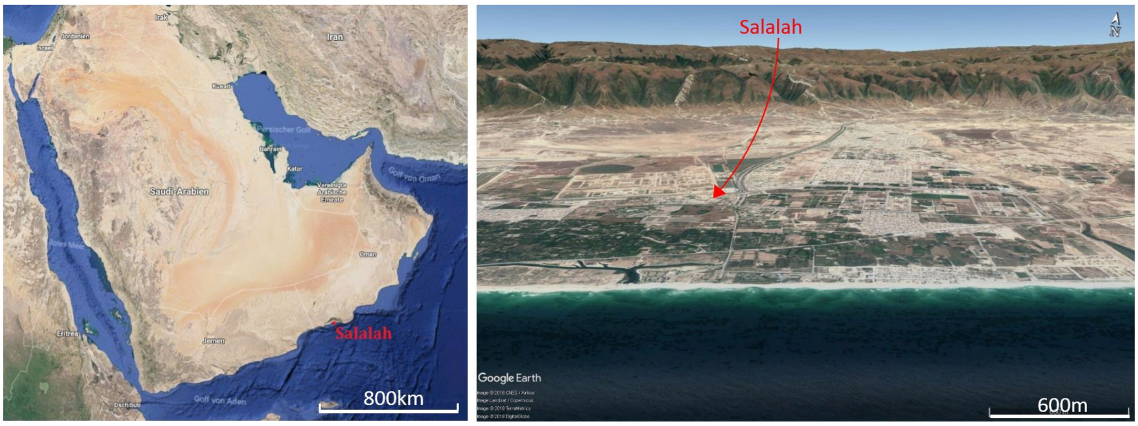

Figure 4.1: Left: Map of the Arabian Peninsula, with Salalah on the South Omani coast [Google Earth, a]. Right: View on the Salalah Plain from South, with the Dhofar mountain range in the North [Google Earth, b].

country are not suitable for agriculture, development plans were focused on a few certain areas meeting the standards for soil quality and water availability. Out of all governorates, Dhofar showed the highest growth of agricultural production between 1997 and 2010. Currently, agriculture accounts for about 70 % of the water demand in the Salalah plain [ICBA, 2012].

At the same time, economic drives to diversify Oman's economy from its reliance on fossil oil have led to an expansion of the industrial sector [McDonnel, 2016]. Nevertheless, it only accounts for about 5 % of the water consumption in Oman.

Finally, the water demands for domestic use have grown due to population growth and increasing living standards. With an average consumption of 200 - 250 L per day, Omanis exhibit a more conservative water use behaviour than their Saudi-Arabian neighbours (500 - 700 L/day) but an increase is looming ahead [Bennet and Kaye, 2018].

Altogether, the total water demand in the Salalah Plain has more than quadrupled since 1980 [ICBA, 2012].

In contrast to increasing demands, Oman is one of the most arid countries of the world and freshwater is a highly limited resource [Bawain, 2012]. While domestic and industrial water demands are increasingly being met by government-subsidized desalination and (in the near future) treated wastewater, the agricultural sector primarily makes use of groundwater [McDonnel, 2016].

In the Salalah Plain this is done by a network of installed wells extracting groundwater from the underlying aquifer. However, extensive pumping has led to the intrusion of seawater which is discussed in Section 4.1.1.

Preliminary studies and the IATI-SGD project To address the groundwater quality problems, a better hydrogeological understanding of the aquifer system in the Salalah Plain is crucial. As a consequence, a variety of studies have been undertaken in the recent past. Besides considerations of the hydrochemistry of the system [Askri et al., 2016], vegetation effects [Bawain, 2012], conceptual flow models [Mueller, 2012], precipitation origins [Strauch et al., 2014] and paleoclimate, a subject of great significance were groundwater ages in the Salalah Plain. Tritium measurements in the plain revealed that the groundwater's mean age was no higher than 35 years [Clark et al., 1987].

In 2015, a joint project was launched between the *GEOMAR Helmholtz Centre for Ocean Research, Kiel, Germany*, the *Helmholtz Centre for Environmental Research - UFZ, Leipzig, Germany* and the ***I**nstitute of **A**dvanced **T**echnology **I**ntegration (IATI)* established through ***T**he **R**esearch **C**ouncil (TRC)*. The aim of the project is to explore, analyse, monitor and model water resources from the foothill of the Dhofar mountains to the Arabian Sea, with a focus on **S**ubmarine **G**roundwater **D**ischarge (SGD). Besides marine investigations, onshore studies to assess and quantify groundwater flow were carried out in the Salalah Plain. This involved an estimation of the natural recharge to the aquifer system as well as a characterization of hydrochemical parameters, stable isotope signatures, inorganic solute concentrations and results from dating tracers [IATI, 2015]. In the course of this thesis, the collaboration will be referred to as the **IATI-SGD project**.

In multiple field campaigns, the infrastructure of monitoring and abstraction wells in the Salalah Plain was assessed and wells at different locations were sampled. Hydrochemical analysis revealed information on solute concentrations throughout the plain and the water origin was identified using stable isotopes. While those results were in accordance with earlier findings, data from dating tracers showed ambiguous results. In contrast to the findings of Clark et al. [1987], all tritium values were below the error margin, indicating the water was infiltrated before the bomb peak in the 1960s (compare Figure 2.7). Meanwhile, radiogenic ^{4}He data yielded inconsistent results with respect to qualitative age considerations. This primarily concerned the Eastern plain where extraordinarily high levels of helium had been found [Mueller, 2018]. Paradoxically, samples from the foot of the mountains were closer to the radiogenic end member than samples taken further downstream, indicating a reversed flow behaviour far inland. Furthermore, one of two wells sampled for radiocarbon dating showed exorbitantly high ^{14}C levels exceeding any atmospheric values ever observed. Thus, a contamination source apart from the atmosphere must exist to produce ^{14}C levels of that magnitude. However, sources of local ^{14}C production, e.g. by nuclear power plants [Yim and Caron, 2006], could not be identified. With an activity of about 0.9 pMC, the second sampled well was in an uncorrected tracer age range of <900 years making the application of any correction model impossible. Hence, at least one of two samples was contaminated and no age information could be deduced.

Those aspects unfolded the necessity of another dating tracer. For its chemical inertness combined with a half-life in the suitable dating range, the radioisotope ^{39}Ar was the tracer of choice for this study (see Section 2.2.5). The only institution currently able to measure ^{39}Ar with ArTTA, the University of Heidelberg, joined the campaign in May 2018. The aim of the sampling campaign was to constrain the residence times in different areas of the Salalah plain with a reliable dating tracer and to put them in context with other dating tracer data.

4.1.1 Hydrogeological setting

The Salalah Plain is about 65 km long and 15 km wide at its broadest point in the center, with a slope of about 100 m at the foot of the mountains down to sea level [ICBA, 2012]. From the plains, the elevation rises abruptly to more than 1 000 mASL (*Dhofar mountains*), with higher ridges in the East and West than in the center [Brueckmann et al., 2016]. The mountains are characterized by deep channels and valleys called *wadis*. North of the Dhofar mountains lies the *Najd* region, a gravel desert with a gently declining slope towards the North.

The Salalah Plain is underlain by the *Fars* formation, a shallow karstic limestone aquifer of tertiary origin with porosities up to 35 % [Flint and Rippon, 1986]. The aquifer exhibits a lower thickness and a higher number of geological fault zones in the East than in the center and the West of the plain.

Recharge The Fars aquifer is naturally recharged in the Dhofar Mountains by an annual precipitation of about 230 - 450 mm/yr from the Indian monsoon and moderate winter rainfall while occasional storm events occur on an infrequent basis

[Shammas and Jacks, 2007]. In the Salalah Plain, less rain is found than in the mountains. The climate graph of Salalah is depicted in Figure 4.2a. Thus, the abstracted groundwater in the Salalah Plain is mainly derived from precipitation infiltrating in the Dhofar mountains and flowing towards the plain [D.MI, 1992].

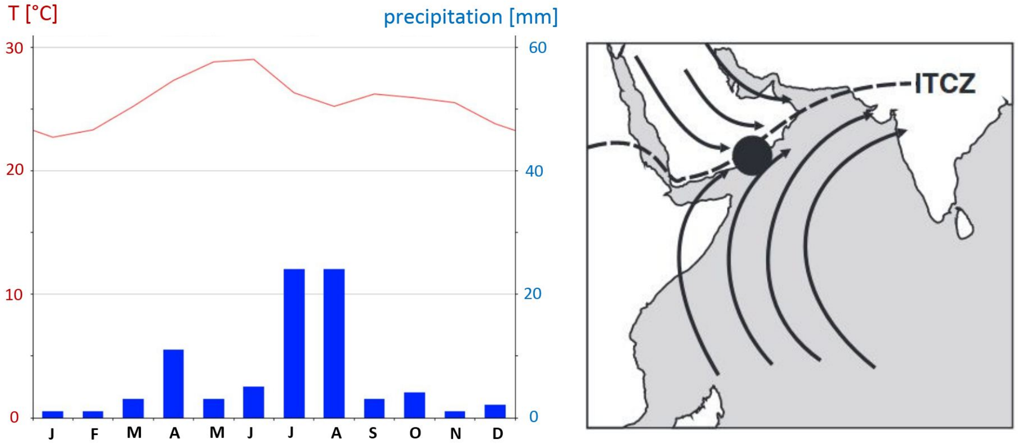

(a) (b)

Figure 4.2: a) Climate graph of Salalah, averages between 1982 and 2012 [Climate, 2012]. b) **I**nnertropical **C**onvergence **Z**one (ITCZ) and winds of the Indian Monsoon in the summer [Fleitmann et al., 2007].

The Dhofar Mountains are the only area of the Arabian Peninsula brushed by the Northern tail of the annual South-West monsoon depicted in Figure 4.2b. Providing a combination of light rain and fog, it represents the most reliable water source of the study area, both as infiltrated groundwater and as surface run-off [Clark et al., 1987; Bawain, 2012]. During monsoon season (*Khareef*) between June and late September, a high vegetation cover of the Salalah Plain (cloud forest) is found, drawing thousands of ecotourists to Salalah. In contrast, the ground looks dry and barren during months of low precipitation. The difference in vegetation cover can be seen in Figure 4.3.

In the winter months (december to april), frontal systems from the North provide moderate rainfall to the Salalah Plain and Dhofar Mountains.

Storm events in Dhofar happen on an infrequent basis (every 2 to 3 years) and result in heavy rains. They originate from either low pressure systems moving across Oman or from cyclones moving westward from the Arabian Sea [Clark et al., 1987].

Figure 4.3: a) Vegetation cover of the Dhofar mountains and fog during monsoon season [Anker, 2010]. b) Dry gravel hills during the dry season (picture taken a few weeks before the start of monsoon season).

Seawater intrusions While the recharge of the Fars aquifer is estimated to be about 30 000 - 50 000 m^3/year, substantially higher groundwater discharge rates have been reported (around 70 000 m^3/year in 2010) [D.MI, 1992; ICBA, 2012]. This deficit in the groundwater budget (see Section 2.1.4) has been shown to not only induce a diminishing of the aquifer but also a reversed water flow from the sea inland [Bear and Cheng, 1999; Shammas and Jacks, 2007].

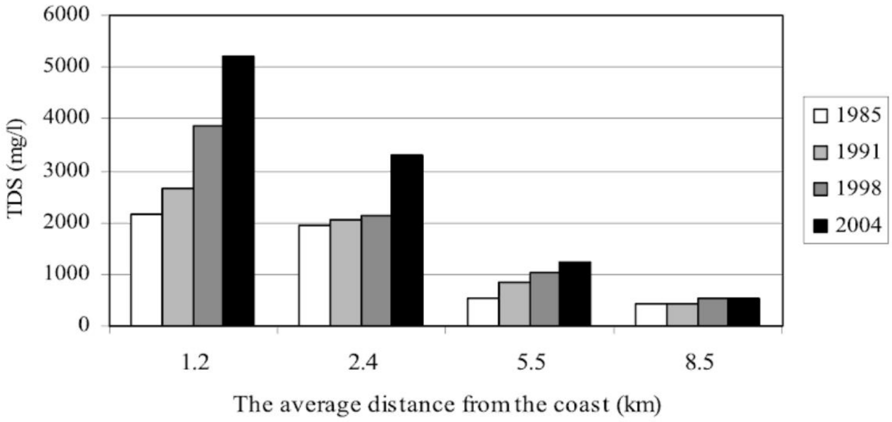

Figure 4.4: Average amount of total dissolved solids (TDS) as a function of distance from the coast, with rising levels from 1985 to 2004 due to seawater intrusions [Shammas and Jacks, 2008].

The seawater intrusions have increased salinity levels along the coastline, but also further inland on the Plain, leading to groundwater quality below drinking standard and reduced agricultural yields [Askri et al., 2016; ICBA, 2012]. This can be seen in Figure 4.4 where the amount of **T**otal **D**issolved **S**olids (TDS) exhibits a major increase between 1985 and 2004 close to the coast. At a distance of 8,5 km from the coast, almost no alteration in salinity was measured.
High salinity levels were found to be more pronounced in the Eastern and Western part of the plain than in the center despite lower groundwater withdrawel rates in those areas [Shammas, 2008]. This may be due to eustatic changes in the area of Salalah; studies suggest that the ocean's waterfront in the geological past reached further inland than today [Robinet et al., 2013]. Apart from that, a higher groundwater flow is estimated in the center than in the East and West [Geo Resources Consultancy, 2004]. Figure 4.5 summarizes the water levels in the Salalah Plain (a) and the classification of groundwater with respect to salinity and ion composition (b). The groundwater was classified by Askri et al. [2016] into three types based on the electric conductivity: the fresh (EC $< 1500\,\mu S/cm$), the brackish ($1500 - 3000\,\mu S/cm$) and the saline zone ($> 3000\,\mu S/cm$).

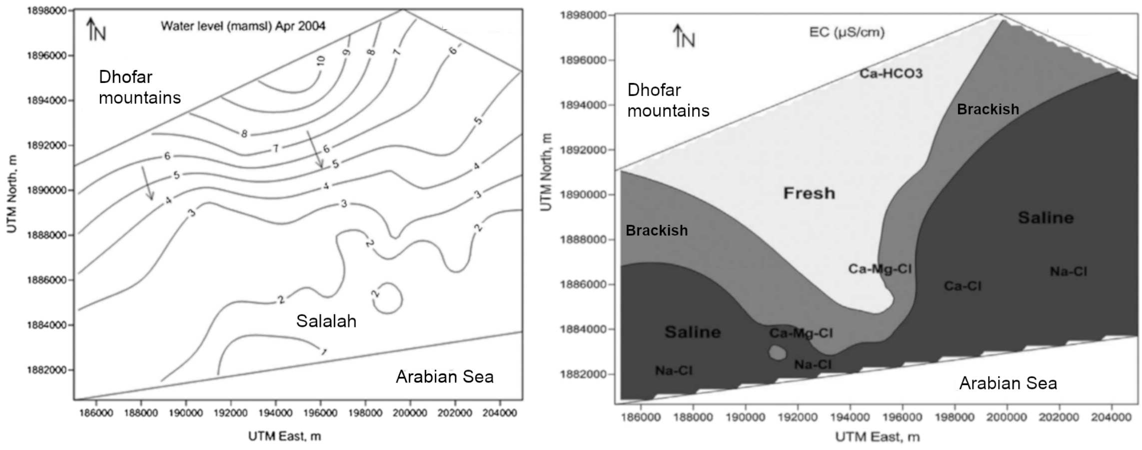

(a) (b)

Figure 4.5: a) Water levels and flow directions in the Salalah Plain. b) Categorization of the Salalah Plain from salinity levels and hydrochemical composition [Askri et al., 2016].

In 2003, an area of elevated hydraulic head by artificial recharge was established along the coast to halt seawater intrusion. Treated wastewater from the municipality is infiltrated through a line of 40 m deep injection wells. The water quality is monitored by observation bores nearby. With this project, water levels are stabilized and saline waters are pushed back towards the coast [Shammas, 2008]. This aspect is of significance for the consideration of samples taken in vicinity of the injection area.

4.2 Sampling

In this section, the sampling in the Salalah Plain is described. At first, the selection of the sampled wells is elucidated. In the following, the typical schematic structure of a well in Dhofar is explained. At last, difficulties and the dealing with them during the sampling campaign are outlined.

4.2.1 Selection of the sampling sites

Although an entire network of sampling wells exists in the Salalah Plain, not all of them were considered suitable for the campaign. Apart from accessibility aspects, the locations and data records of the wells were criteria of importance for the selection of the sampled wells.

In the context of the IATI-SGD project, different sampling conditions and difficulties of the individual wells had been experienced in multiple field campaigns in 2016 and 2017. This experience was valuable to rule out all wells with collapsed bores and problematic accessibility.

As the campaign's main objective was the dating of groundwater with ^{39}Ar, the selection of wells was tailored to the capacities and limitations of this tracer. The low isotopic abundance of ^{39}Ar brings about a high susceptibility to contamination by atmospheric air or (young) equilibrated water components. Sampling locations at the foot of the Dhofar mountains are thought not to be directly influenced by irrigation effects or seawater intrusions; thus, those locations were given preference to locations in vicinity of intense agricultural irrigation or the coast. In addition, hydraulic heads in areas of high groundwater abstraction rates are lowered which may induce alterations in the flow behaviour. This was considered another factor militating for wells at the Northern edge of the plain. Thus, sampling along the mountain front would yield a comparison between groundwater ages in the outer parts and the center, as an indicator for the flow rates. On the other hand, it is possible to identify age differences between samples taken upstream and downstream in the same flow line due to the resolution of ^{39}Ar. This feature could be made use of by taking multiple samples along flow lines to characterize the flow in the system.

On top of that, the existing data record from preliminary campaigns was taken into account. The availability of information on water levels, noble gases and hydrochemistry made wells sampled in 2016 and 2017 attractive candidates for this campaign. In addition, the reliability of ^{39}Ar was expected to disentangle unclear findings from other tracers, especially in the Eastern part of the plain.

Figure 4.6: Map of the sampling area with the sampled wells. Icon colours indicate the type of sampling procedure [QGIS].

Based on the assessment of those aspects, potential sampling locations were chosen. Most were located along the mountains beyond the pumping area, with a few wells further inland to monitor the age along flow lines. A limit of 10 sampled wells was set, for ^{39}Ar measurement with ArTTA is time-consuming and expensive.
Due to complications during the campaign, only five of the chosen wells could be sampled and other techniques had to be applied, as delineated in the following section. In Figure 4.6, the locations of the sampled wells are indicated on the map of the Salalah Plain. The full well IDs for the well codes and coordinates are found in Table 6.3 in the Appendix. The wells can be assigned to different salinity categories according to Figure 4.5b. While wells 25 and 33 are in the freshwater zone and wells 66 and 69 fall in the brackish zone, well 20 is located between the two zones. Meanwhile, wells 1, 19 and 58 are situated in the saline zone.

4.2.2 Well structure

To understand the composition of the water mixtures in the boreholes, this section briefly describes the structure of a typical sampling well in Dhofar. As can be seen in the cross section in Figure 4.7, a part of the borehole is covered by a cement casing. In this section, no water from the aquifer intrudes the well. The water enters through the *screen* which is the uncased part of the well. The water level in the borehole equals the hydraulic head (see Section 2.1.2) and is commonly specified in meters above sea level (mASL). Another important number is the height of the vadose zone which is simply the difference of the ground level and the water level. The total drilled depth is measured relative to the ground level (unit: meters below ground level, mBGL).

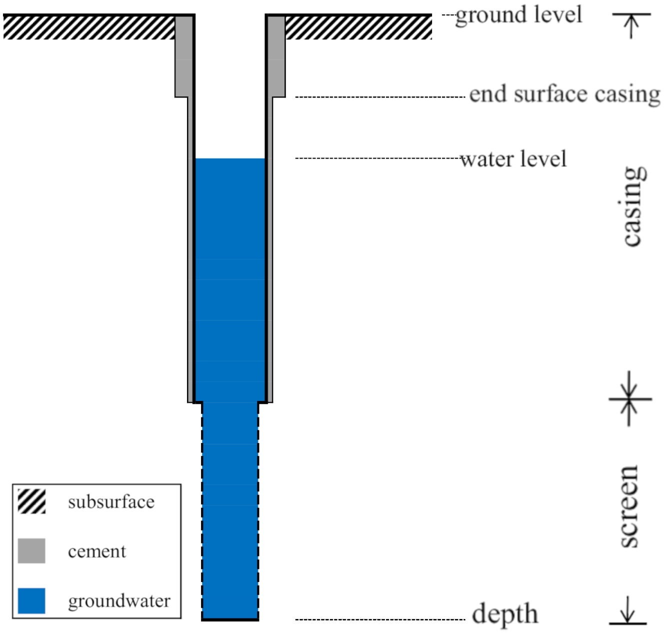

Figure 4.7: Cross section of a typical well in Dhofar [Herb, 2011].

In Table 4.1 information on the elevation of the ground level, the water level and the depth of the sampled wells are found. In addition, the drilled depth and the height of the screen are listed. For wells 66 and 69, none of the numbers were available. For missing data of the other wells, estimates of the screen were done using existing numbers of casing measures.

Wells 25 and 33 are located at much higher elevation and also the water table is significantly higher than at the other wells. Most of the wells extend far below sea level.

well	elevation [mASL]	water level [mASL]	vadose zone [m]	drilled depth [mBGL]	screen [m]
1	45.6	3.6	42	73	<21
19	51.2	3.3	47.9	-	<53.8
20	87	7.5	79.5	-	178[1]
25	132	112.1	19.9	130	29
33	169	150.2	18.8	95	32
58	10	1.2	8.8	112	<40
66	-	-	-	-	-
69	-	-	-	-	-

Table 4.1: Elevation data and measures of the sampled wells.

4.2.3 Sampling in the field

Preliminary to the groundwater campaign, sample containers and the necessary supplements for the sampling of all different tracer methods had to be prepared. The sample containers were cleaned as described in sections 3.1.2 and 3.1.3 in order to avoid contamination. The sampling equipment was shipped to Oman by a shipping company, which posed problems of both administrative and juridical nature. Despite a great number of complications and delays, the equipment arrived in Salalah in time for the campaign. In Salalah, a shed on the grounds of the ***M****inistry of* ***R****egional* ***M****unicipalities and* ***W****ater* ***R****esources (MRMWR)* served as storehouse and workshop. Here, the sample containers were evacuated and the equipment was gathered for the individual sampling excursions.

On the sampling site, the pump was set up as pictured in Figure 3.1a (Section 3.1) and the wells were purged to remove stagnant water. The extracted water volume was monitored with a flow meter to ensure that the well volume was exchanged three times. When the field parameters had stabilized, the sampling was done as delineated in Section 3.1.

Although spare days were scheduled in the campaign, only eight wells were sampled due to difficulties with the equipment. Those included generators with unstable output voltage, a water damaged frequency converter for the MP1 pump, the MP1

---

[1] well 20: Only 108,5 m of the screen are located below the water table

pump itself and, ultimately, a broken car battery. However, all problems concerned the delivering of sample water while the sampling itself was carried out without any trouble. After it had become obvious that conventional sampling with the MP1 pump was not feasible any more, other techniques to convey the water had to be found.

In Figure 4.8a, the sampling setup at a water tank is depicted. Those tanks are fed by permanently installed pumps in a few hundred meters distance and serve for water storage. To avoid contamination, a hose was pushed into the input pipe and a part of the water is diverted for sampling. The delivered water was monitored for air bubbles and the hose was pushed down the pipe until no air was indrawn any more. Once this setup was completed, the sampling procedure was carried out next to the tank in the usual manner. Samples 66 and 69 originate from such tanks.

The second alternative sampling method was provided by a 12 V submersible rotary *Comet* pump with lower pumping power than the MP1 pump. The power was drawn from a car battery, as can be seen in Figure 4.8b. Due to a maximum lifting capacity of about 10 m above the water table, the selection of sampling sites was limited and only well 58 was sampled with this method.

The sampling method of use can be seen in Figure 4.6. While wells with yellow icons were sampled using the (conventional) MP1 pump, green and blue icons indicate water delivered by tanks and the comet pump, respectively.

(a) (b)

Figure 4.8: Alternative sampling techniques: a) Sampling the intake of a tank supplied by a permanently installed pump. b) Sampling with the Comet pump run with power from the car battery.

4.3 Data

In this section the results of the measurements are reported. First, data of the field parameters are given and excess air is quantified. In the following, tracer ages are calculated using the data of the dating tracers. At last, the individual tracer data are compared and a mixing model is presented.

4.3.1 Field parameters for groundwater chemistry

For each well, the temperature, pH, electric conductivity and titration were measured. Due to complications during sampling, no temperature value could be taken for well 66. Salinities were calculated according to Eq. 2.20 using the measured electric conductivity (EC) κ at $T = 25\,^\circ\mathrm{C}$. For titration, sulfuric acid (H_2SO_4) was added into 100 ml of sample water to a pH 4.3 end point using a 1.6 N Hach titration apparatus. With Eq. 2.22 in Section 2.2.1, the equivalent HCO_3^- values were calculated. The uncertainty $\Delta\mathrm{Alk}_{\mathrm{HCO_3^-{-}eqiv}}$ was derived by the error of the mean $\Delta\mathrm{Alk}_{\mathrm{CaCO_3^-{-}eqiv}} = s_m$ of the individual titration measurements (usually 2 to 3):

$$\Delta\mathrm{Alk}\left[\frac{\mathrm{mg}}{\mathrm{L}}\right]_{\mathrm{HCO_3^-{-}eqiv}} = \Delta\mathrm{Alk}\left[\frac{\mathrm{mg}}{\mathrm{L}}\right]_{\mathrm{CaCO_3{-}eqiv}} \cdot \frac{M_{\mathrm{molar}}(\mathrm{HCO_3^-})}{M_{\mathrm{molar}}(\mathrm{CaCO_3})}\,. \tag{4.1}$$

For well 58, no titration was done during this sampling campaign, so a previous value was used. As only one value was available, no error of the mean could be calculated. The field parameters for all sampled wells can be found in Table 4.2.

well	T [°C]	pH	salinity [‰]	titration (HCO_3^--equiv.) [mg/L]	O_2 [mg/L]
1	31.6	7.008	1.77	264.5 ± 3.7	4.98
19	34.4	7.299	1.40	162.7 ± 3.0	0.85
20	32.2	6.995	0.61	278.3 ± 17.9	6.24
25	30.0	6.967	0.56	257.2 ± 2.4	6.43
33	30.2	6.906	0.54	270.0 ± 0.6	6.14
58	30.9	7.610	10.09	151.1[2]	5.59
66	-	7.116	1.74	250.5 ± 3.0	6.45
69	31.1	6.938	2.85	246.2 ± 3.7	5.83

Table 4.2: Field parameters of the sampled wells.

The majority of the field parameter data are consistent with expectations. For the only well in the desert area of the central plain, well 19, a raised water temperature and lower O_2 levels are found than in the other wells. Wells located at the central foot of the mountain (20, 25, 33) show the lowest salinities. Higher salt contents were measured in the East and West of the plain (wells 1, 66, 69) as well as further downstream in the center (19). Well 58 shows significantly higher salt levels which is plausible as it is located in vicinity of the coast.

Using EC data, the categorization into fresh, brackish and saline zones by Askri et al. [2016] can be revisited. Wells 1 and 19 showed lower ECs than predicted from Figure 4.5 while well 69 is more saline than expected. Hence, wells 20, 25 and 33 fall in the fresh zone, wells 1, 19 and 66 are located in the brackish zone and wells 58 and 69 are part of the saline zone. Those categories are a convenient tool to identify clusters of wells with similar behaviour with respect to recharge sources and flow rates.

4.3.2 Tracers for excess air

The amount of excess air is quantified with the measured Ne concentrations as described in Section 2.2.3. The infiltration temperatures and their uncertainties were calculated by Werner Aeschbach using noble gas thermometry. For well 58, the temperature fit does not converge. Thus, the infiltration temperature of an upstream location (well 66) is used. For the infiltration altitude, a value of $500 \pm 250\,\mathrm{mASL}$ is assumed. Salinities are taken from field parameters (Table 4.2). Well 58 shows an exceeding salinity level due to seawater intrusions. As it can be excluded that this salinity was present during infiltration, the salinity value measured at well 66 is assumed for well 58. Although salinity in groundwater generally is not considered a conservative tracer, most wells are located along the mountain front and the measured salinities may reflect a spacial trend of the salinities in the recharge area. Hence, those parameters are used to calculate the equilibrium neon concentration $\mathrm{Ne}_{\mathrm{eq}}$.

For the uncertainty analysis, the error of the equilibrium neon concentration $\Delta\mathrm{Ne}_{\mathrm{eq}}$ is estimated using upper and lower bounds of the infiltration temperature and altitude. In combination with the measurement uncertainty $\Delta\mathrm{Ne}_{\mathrm{meas}}$, this yields

---

[2] This value was taken from a sampling campaign in 2016.

the excess air uncertainty

$$\Delta \mathrm{Ne_{ex}} = \sqrt{(\Delta \mathrm{Ne_{eq}})^2 + (\Delta \mathrm{Ne_{meas}})^2}. \tag{4.2}$$

To derive the total excess air concentration, an atmospheric neon ratio of $r_{\mathrm{Ne.atm}} = (1.818 \pm 0,004) \cdot 10^{-5}$ [Porcelli et al., 2002] is assumed. Excess air is calculated by

$$\frac{V_{\mathrm{air}}}{V_{\mathrm{w}}} = \frac{\mathrm{Ne_{ex}}}{r_{\mathrm{Ne.atm}}} \tag{4.3}$$

$$\Delta\left(\frac{V_{\mathrm{air}}}{V_{\mathrm{w}}}\right) = \frac{V_{\mathrm{air}}}{V_{\mathrm{w}}} \cdot \sqrt{\left(\frac{\Delta \mathrm{Ne_{ex}}}{\mathrm{Ne_{ex}}}\right)^2 + \left(\frac{\Delta r_{\mathrm{Ne.atm}}}{r_{\mathrm{Ne.atm}}}\right)^2} \tag{4.4}$$

with $\frac{V_{\mathrm{air}}}{V_{\mathrm{w}}}$: excess air in $\left[\frac{\mathrm{cc}}{\mathrm{L}}\right]$.

The results are depicted in Figure 4.9 in the following section. Wells 20 and 33 show the highest levels of excess air ($> 2\,\mathrm{ccSTP/g}$) while the lowest level is found in well 58 ($< 1\,\mathrm{ccSTP/g}$). All other wells exhibit moderate values between 1 and 2 ccSTP/g.

Generally, a trend of more excess air is seen in wells located in the center of the plain. This finding meets the expectations as excess air formation is enhanced by large water table fluctuations [Aeschbach et al., 2002]. Those fluctuations between pre- and post-monsoon have been reported to be more pronounced in the central plain (up to 5 m) than in the East and the West (<2 m) [Brueckmann et al., 2016]. This difference may originate from a higher groundwater inflow in the center.

4.3.3 Dating tracers

The main objective of the groundwater study is the investigation of groundwater ages at different locations. This section summarizes tracer ages (according to the Piston-flow Model) obtained by different tracers. In Section 4.3.3, qualitative age information is derived from radiogenic helium. ^{14}C results including different correction models are outlined in Section 4.3.3. Data from the ^{39}Ar extraction and purification are given in Section 4.3.3. At last, age information derived by CFCs and SF$_6$ are found in Section 4.3.3.

^{4}He

The measured helium components are identified as described in Section 2.2.5. The calculation of excess air using the measured neon concentrations is found in Section 4.3.2.

The uncertainty of the radiogenic He component is derived by

$$\Delta \mathrm{He}_{\mathrm{rad}} = \sqrt{\Delta \mathrm{He}_{\mathrm{meas}}^2 + \Delta \mathrm{He}_{\mathrm{eq}}^2 + \Delta \mathrm{He}_{\mathrm{ex}}^2} \tag{4.5}$$

with $\Delta \mathrm{He}_{\mathrm{meas}}$: measurement uncertainty

$\Delta \mathrm{He}_{\mathrm{eq}}$: equilibrium concentration uncertainty originating from temperature and altitude uncertainty

$\Delta \mathrm{He}_{\mathrm{ex}}$: excess air uncertainty .

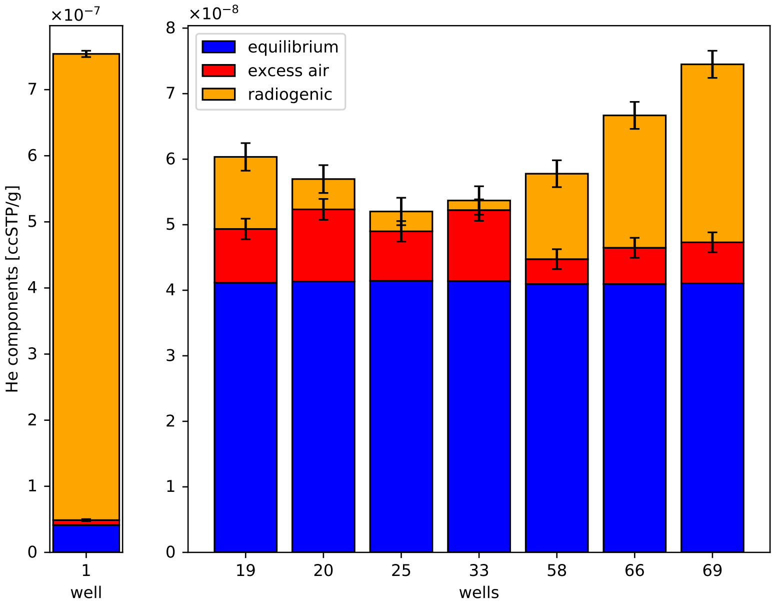

Figure 4.9: ^{4}He components of the sampled wells.

As can be seen in Figure 4.9, the wells show different proportions of $^{4}\mathrm{He}_{\mathrm{rad}}$. The three central wells at the foot of the mountains (20, 25, 33) show the lowest $^{4}\mathrm{He}_{\mathrm{rad}}$ concentrations. The higher $^{4}\mathrm{He}_{\mathrm{rad}}$ level in well 19 seems reasonable as it is thought to lie downstream on a flow path. In comparison, the water in the Western wells (66 and 69) seems to be of older origin although they are located close to the infiltration area. Interestingly, the levels in well 58 are lower although it is located downstream

from there. This may be due to a mixing process with modern ($^4\mathrm{He}_\mathrm{rad}$-free) water, i.e. seawater intrusions and infiltrated wastewater. In total, wells 19 - 69 convey a consistent idea in accordance with an expected higher (and faster) groundwater flow in the center of the plain than in the outer zones. Based on those results, similar tendencies in the groundwater ages deduced by other dating tracers are expected to be found.
Well 1 is plotted using a different scale as it shows $^4\mathrm{He}_\mathrm{rad}$ levels one magnitude larger than the other wells. This abrupt increase towards the Eastern plain has already been reported in the context of the IATI-SGD project [Mueller, 2018] and is now verified. The origin of this accumulated radiogenic helium has not been identified yet and remains an open question.

^{14}C

The water samples for ^{14}C dating were taken and purified according to Sections 3.1.2 and 3.2.1. Well 69, a water tank fed by a permanently installed pump could not be sampled for ^{14}C as the clocked water delivery ended before the sampling was completed. The graphitized samples were measured by Ronny Friedrich in the Radiocarbon AMS-Lab at the Curt Engelhorn Centre for Archeometry Mannheim.

Contamination The amount of residual modern CO_2 in the bottle can be quantified using pressure values from the bottle preparation. As this is only an analysis of magnitude, several approximations are made for simplicity.
First, the amount of CO_2 dissolved in the sample water is estimated from Henry's law:

$$\begin{aligned} m_{\mathrm{CO_2.water}} &= c_{\mathrm{CO_2.air}} \cdot L_{\mathrm{CO_2}} \cdot V_{\mathrm{bottle}} \cdot \rho_{\mathrm{CO_2}} \\ &\approx 6 \cdot 10^{-5}\,\mathrm{g\ CO_2} \end{aligned} \tag{4.6}$$

with $c_{\mathrm{CO_2.air}} = 3.7 \cdot 10^{-4}$: atmospheric concentration of CO_2 [Porcelli et al., 2002]
$L_{\mathrm{CO_2}} = 0.04065$: Ostwald solubility of CO_2 at 20 °C [Aeschbach, 2017]
$V_{\mathrm{bottle}} = 100\,\mathrm{ml}$: volume of sample bottle
$\rho_{\mathrm{CO_2}} = 1.83 \cdot 10^{-3}\,\frac{\mathrm{g}}{\mathrm{mL}}$: density of CO_2 at 20 °C [IFA]

The modern component is deduced as follows. Initially, the sample bottles are filled with air and hence, the CO_2 concentration is atmospheric. As described in Section 3.1.2, the sampling bottles are evacuated twice to a pressure of $p_{\text{vac.lab}} \approx 10^{-1}\,\text{mbar}$ in the laboratory and a third time in the sampling area with $p_{\text{vac.field}} = 1,4\,\text{mbar}$. This leads to the amount of modern CO_2:

$$\begin{aligned} m_{\text{CO}_2\text{.modern}} &= c_{\text{CO}_2\text{.air}} \cdot V_{\text{bottle}} \cdot \left[\frac{10^{-1}\,\text{mbar}}{1\,\text{atm}}\right]^2 \cdot \frac{1.4\,\text{mbar}}{1\,\text{atm}} \cdot \rho_{\text{CO}_2} \\ &\approx 7 \cdot 10^{-16}\,\text{g CO}_2\ , \end{aligned} \tag{4.7}$$

which is only a factor of $r = 10^{-11}$ of the sampled CO_2.
Correcting for the mixing process as described in Section 2.3 results in

$$\begin{aligned} A_{\text{sample}} &= \frac{1}{1-r} \cdot (A_{\text{meas}} - r \cdot A_{\text{modern}}) \\ &\approx A_{\text{meas}} - 10^{-11} \cdot A_{\text{modern}} \\ &\approx A_{\text{meas}} \end{aligned} \tag{4.8}$$

with A_{sample} : corrected ^{14}C activity of the sample
A_{meas} : measured ^{14}C activity of the sample
$A_{\text{modern}} = 1\,\text{pMC}$: modern ^{14}C activity

As the accuracy of the measured ^{14}C activity is in the range of $10^{-3}\,\text{pMC}$, contamination effects are several numbers of magnitude smaller and can be discarded for the data evaluation. In addition, contamination originating from leaks in the carbon extraction setup may play a role but cannot be quantified.

Results The δ^{13}C results plotted against the ^{14}C values are depicted in figure 4.10. For the calcite dissolution, the δ^{13}C values of the end members *soil air* (modern component with 1 pMC) and *calcite* (old component with 0 pMC) were taken from Al-Mashaikhi [2011]. For the modern component, the mean (and its error) from four δ^{13}C values measured in the infiltration area was calculated, giving
$\delta^{13}\text{C}_{\text{soil}} = (-17.6 \pm 2,9)\,‰$. For the old end member, $\delta^{13}\text{C}_{\text{calcite}} = (+2 \pm 1)\,‰$ was assumed.
In the plot, the data points should be located within the error margins of the mixing line or underneath. As a decrease of ^{14}C with time would be expected while δ^{13}C is constant, the values would wander from a certain starting point on the line to the

left. However, this is only the case for wells 19 and 66. All other wells seem to be enriched in δ^{13}C with respect to the expected mixing line between the end members. This aspect depicts a complication for the Pearson model and is addressed in the following.

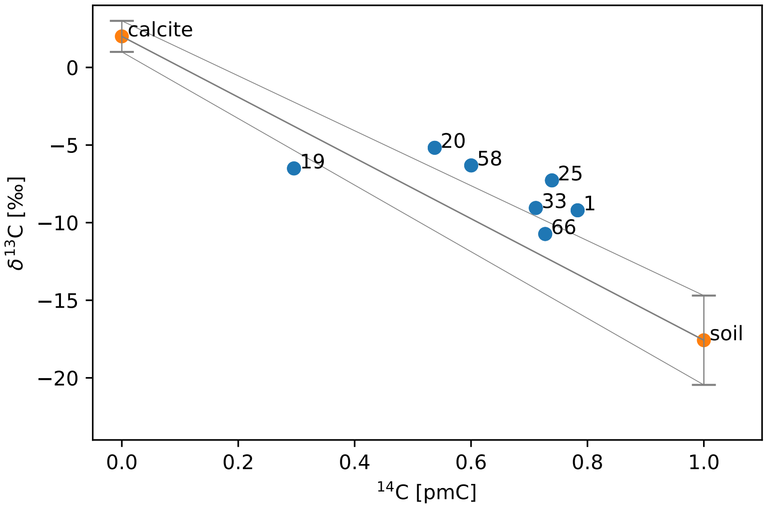

Figure 4.10: δ^{13}C data plotted against ^{14}C, with a mixing line between (modern) soil CO_2 and (radiocarbon-dead) calcite.

As described in Section 2.2.5, the radiocarbon age of the groundwater samples was determined and several correction models were applied. The results are summarized in the following.

Radiocarbon age (uncorrected): The radiocarbon ages with respect to the sampling year were calculated, with errors

$$\Delta \mathrm{t}_{\text{uncorrected}} = \mathrm{t}_{\text{uncorrected}} \cdot \sqrt{\left(\frac{\Delta \mathrm{T}_{1/2}}{\mathrm{T}_{1/2}}\right)^2 + \left(\frac{\Delta A_{\text{meas}}}{A_{\text{meas}}}\right)^2} \tag{4.9}$$

As depicted in Figure 4.12, the tracer ages range between 2000 and 10 000 years. Wells 25 and 33 are among the youngest samples as expected while well 20 seems surprisingly old, given it is located at the foot of the mountains. Likewise, wells 1 and 66 representing wells located in the East and West at the foot of the mountains can be ascribed to the group of rather young ages. Well 19 located downstream in the center meets the expectations of an older radiocarbon age. In contrast, the tracer age of well 58 is much younger although it is located far downstream from the recharge area. Similar to the considerations for $^4\mathrm{He}_{\mathrm{rad}}$, this is an indication for a mixing process with modern components.

Vogel model: In the Vogel model, the initial activity A_0 of modern ^{14}C is corrected by a factor of $q_{\mathrm{Vogel}} = 0.80 \pm 0.05$. While the correction factor commonly found in literature is about 0.85, smaller values have been found for karst systems [Vogel, 1967]. Hence, the geological properties of the karstic aquifer environment in the Salalah Plain can be taken into account.

Generally, this leads to a shift of the groundwater transit times towards younger ages. Due to the characteristics of the logarithm, this is equivalent to subtracting a constant value from the radiocarbon ages. Thus, the Vogel model causes a higher relative age change for young samples than for old samples. The results can be seen in Figure 4.12. Errors were calculated by

$$\Delta \mathrm{t}_{\mathrm{Vogel}} = \mathrm{t}_{\mathrm{Vogel}} \cdot \sqrt{\left(\frac{\Delta \mathrm{T}_{1/2}}{\mathrm{T}_{1/2}}\right)^2 + \left(\frac{\Delta A_{\mathrm{meas}}}{A_{\mathrm{meas}}}\right)^2 + \left(\frac{\Delta A_{0.\mathrm{Vogel}}}{A_{0.\mathrm{Vogel}}}\right)^2} \tag{4.10}$$

Tamers model: For the Tamers age, the activities $[\mathrm{CO}_{2\,\mathrm{aqueous}}]$ and $[\mathrm{HCO}_3^-]$ are derived using alkalinity and pH as described in Section 2.2.5. As the Tamers model tends to overcorrect radiocarbon age, valid values can only be calculated for the two oldest samples (wells 19 and 20). The rest of the samples produces hypermodern ages. Hence, this model is not further considered. The results are listed in Table 6.4.

Pearson model: In the Pearson model, the correction factor q_{Pearson} is calculated using the relation between the measured δ^{13}C and the δ^{13}C of the end members calcite and soil air. With the values used in figure 4.10 ($\delta^{13}\mathrm{C}_{\mathrm{calcite}} = (+2 \pm 1)\,‰$ and $\delta^{13}\mathrm{C}_{\mathrm{soil}} = (-17.6 \pm 2,9)\,‰$), the model overcorrects the ages of all wells to negative numbers except for well 19. Results are found in Table 6.4 but will not be taken into account in the discussion. Hence, the unaltered Pearson model approach does not work for the data set of this study.

A possible explanation is that depending on pH, a fractionation between soil CO_2 and DIC of up to 10 ‰ exists, shifting δ^{13}C towards more positive values (compare Figure 4.11). However, it is hard to determine the pH present during infiltration without in-situ measurements. As outlined in Section 2.2.5, pH is closely linked to the distribution of DIC species. Due to high amounts of dissolved CO_2, it is assumed to be lower (more acidic) than the pH values measured at the sampling sites. Since the effect cannot be quantified in a reasonable way, this method only serves to derive upper and lower age bounds. At pH values present at the sampling sites (see Table 4.2), an enrichment of about 7.1 ‰ between soil CO_2 and DIC is found [Clark and Fritz, 1997], leading to an upper boundary of $\delta^{13}C_{soil} = -10.5$ ‰. For the lower boundary, the value −17.6 ‰ is used as before. Since this calculation only serves as an estimate, uncertainty considerations are renounced.

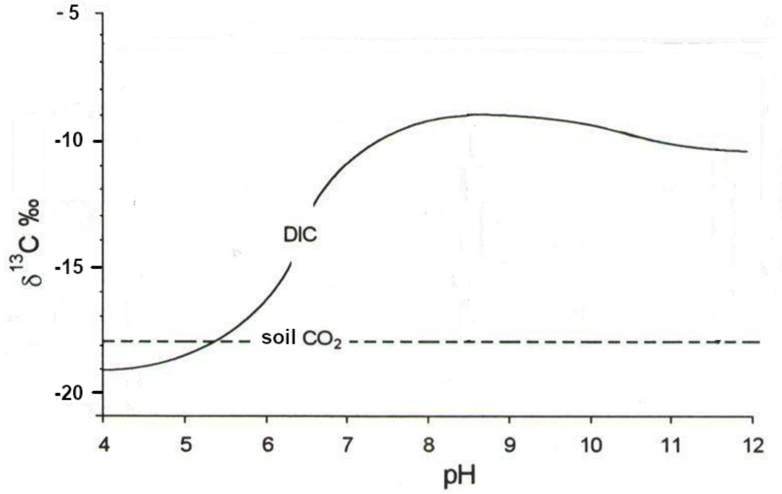

Figure 4.11: Dependence of DIC $\delta^{13}C$ on pH in equilibrium with soil CO_2 ($\delta^{13}C_{soil} \approx -18$ ‰) at 25 °C [Clark and Fritz, 1997].

With this modified Pearson method it is possible to derive positive upper age bounds for all wells. The lower age bound is only positive for well 19. The results are depicted in Figure 4.12 and listed in Table 6.4 in the Appendix. For all wells except for well 19, the (modified) Pearson model predicts groundwater ages below 3000 years. The age range of well 19 is estimated to be between 3000 and 7000 years.

By comparing the ^{14}C age results of the uncorrected model, the Vogel model and the range derived by the Pearson model it becomes obvious that the models produce different results. Only for well 66 both the uncorrected and the Vogel age lie in the Pearson age range. Vogel ages of wells 1 and 33 are in the Pearson age range while the uncorrected ^{14}C age is significantly older. For all other wells, both the uncorrected and the Vogel model indicate groundwater ages that are substantially older than the Pearson age range.

Generally, the Pearson model can be considered the method with the highest credibility as it takes into account $\delta^{13}C$ data measured at the wells. Thus, prevalent

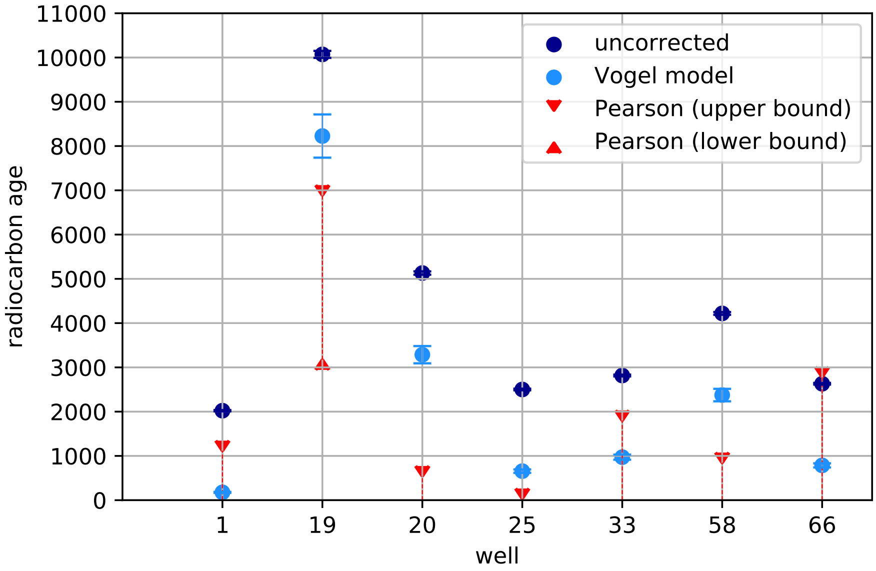

Figure 4.12: ^{14}C groundwater ages derived by the uncorrected radiocarbon method, the Vogel model and the Pearson model. For the Pearson model, an upper bound of $\delta^{13}C_{\text{soil}} = -10.5\,‰$ and a lower bound of $-17,6\,‰$ are used.

environmental conditions are quantified and applied in the age calculation. In contrast, the Vogel model is only based on empirical findings while the uncorrected radiocarbon age does not take into account calcite dissolution at all. Hence, with the ^{14}C method, it is only possible to determine a possible age range with a lower age bound of modern water for all wells but well 19.

^{39}Ar

As described in Sections 3.1.3 and 3.2.2, the water was sampled in propane gas bottles for ^{39}Ar analysis with ArTTA. The dissolved air was extracted and argon was purified. Unfortunately, no sample has been measured so far.

Contamination Analogous to ^{14}C, the ^{39}Ar contamination of the sample containers with atmospheric air can be estimated.

First, the expected argon volume from the sample water is derived according to Section 3.1.3, resulting to an argon yield of about 3 mL. For the contamination, the remaining air in the bottle after the preparation of the sample containers is considered. The argon bottles are initially filled with air of atmospheric concentration

$c_{\mathrm{Ar.atm}} = 0,934\,\%$ [Porcelli et al., 2002]. They are evacuated three times to 1/1000 of their pressure, giving a dilution of factor 10^{-9}. With the volume of the sample container $V_{\mathrm{bottle}} = 12.2\,L$, the argon volume by contamination arises to

$$\begin{aligned} V_{\mathrm{Ar.modern}} &= c_{\mathrm{Ar.atm}} \cdot V_{\mathrm{bottle}} \cdot 10^{-9} \\ &\approx 1 \cdot 10^{-7}\,\mathrm{mL\ Ar} \end{aligned} \tag{4.11}$$

which is a factor of about $r = 10^{-7}$ of the sampled argon. In a mixing process analogous to Section 2.3 the measured activity is corrected as follows:

$$\begin{aligned} A_{\mathrm{sample}} &= \frac{1}{1-r} \cdot (A_{\mathrm{meas}} - r \cdot A_{\mathrm{modern}}) \\ &\approx A_{\mathrm{meas}} - 10^{-7} \cdot A_{\mathrm{modern}} \\ &\approx A_{\mathrm{meas}} \end{aligned} \tag{4.12}$$

with A_{sample} : corrected ^{39}Ar activity of the sample
A_{meas} : measured ^{39}Ar activity of the sample
$A_{\mathrm{modern}} = 1\,\mathrm{pMC}$: modern ^{39}Ar activity

For young samples, the contamination in the order 10^{-7} is negligible compared to the measurement uncertainty of 10 % [Ebser et al., 2018]. However, the effect is increased exponentially for older samples. While a groundwater age of 100 years produces an uncertainty in the order of $\Delta t = 10^{-4}$ years, contamination effects a 1000 year old sample (the upper dating boundary of ^{39}Ar) by about $\Delta t = 10^{-1}$ years.

Argon yield During sampling, preliminary considerations regarding the ideal amount of sample water were taken into account. The volume of the sampled water and the (estimated) amount of purified argon are listed in Table 4.3. The purity is determined by mass spectrometry. All samples yield enough argon for the measurement with ArTTA.

At the time of writing this thesis, the results of the analysis with ArTTA were not available yet. Thus, a data analysis is not possible at this point.

well	sample volume [L]	Ar volume [mL]	purity [%]
1	11,23	3,07	96.7
19	10,76	3,18	97.4
20	10,93	2,78	97.3
25	10,35	2,87	98.3
33	10,33	3,20	97.6
58	10,47	2,70	98.2
66	8,85	2,70	97.7
69	11,00	2,84	97.3

Table 4.3: Amount of sampled water for ^{39}Ar analysis and estimated volume and purity of pure argon extracted.

CFCs and SF_6

The CFC and SF_6 groundwater ages at different wells were calculated as described in sections 2.2.5 and 2.2.5 using the evaluation software by USGS [2017]. The infiltration parameters were chosen analogously to Section 4.3.2 with infiltration temperatures derived by noble gas thermometry, salinities measured in the field and an altitude of $500 \pm 250\,\mathrm{mASL}$. In addition, the excess air values calculated in Section 4.3.2 were applied.

All values with higher equivalent concentrations than atmospheric are excluded from data analysis. While all wells show computable CFC-11 and CFC-12 concentrations, only wells 58, 66 and 69 are taken into account for CFC-113. For the SF_6 analysis, only wells 1, 20, 58, 66 and 69 are considered since the others are clearly contaminated.

CFC errors are derived with upper and lower bound from uncertainties in infiltration temperature, altitude, excess air and the measurement error. For well 25, the error exceeds the possible atmospheric CFC-12 concentration, so the given error of 11 years is only an estimate.

For the calculation of the SF_6 error, the influence of systematic uncertainties in infiltration temperature and altitude is estimated by upper and lower bound. Statistical errors originating from measurement uncertainties of the SF_6 and neon measurements are included by the evaluation software, giving the total error

$$\Delta \mathrm{SF}_6 = (\Delta \mathrm{SF}_6)_{\mathrm{sys}} + (\Delta \mathrm{SF}_6)_{\mathrm{stat}} \ . \tag{4.13}$$

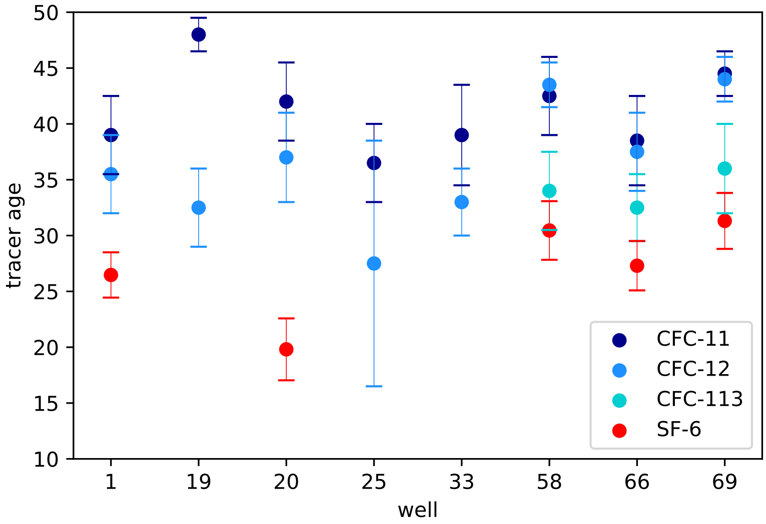

Figure 4.13: Groundwater ages derived from CFC and SF_6 concentrations.

Results The CFC and SF_6 groundwater ages are displayed in Figure 4.13 and the values are found in Table 6.5 (Appendix). Comparing the different tracer ages, a clear trend is seen. For almost all wells, SF_6 yields the youngest ages, followed by CFC-113, CFC-12 and CFC-11. This is investigated in further detail in the discussion (Section 4.5).

The tracer ages calculated using CFC-11 and CFC-12 levels are in good agreement except for well 19. All other wells lie within a 2σ interval. Hence, both tracers are considered in the multi-tracer analysis and is discussed in more detail in Section 4.3.4.

In contrast, CFC-113 data produce valid groundwater ages for only three of the wells and they are significantly younger than the CFC-11 and CFC-12 ages. Due to those aspects, CFC-113 is not used for the multi-tracer analysis.

For wells 1 and 20, high discrepancies between SF_6 and the (valid) CFC ages are seen while wells located in the West (58, 66 and 69) seem to agree better for all four tracers. All wells located in the central plain (19, 25, 33) show exceeding levels of SF_6 making an age calculation impossible. As a consequence, SF_6 is rated an unreliable tracer in this study and is not considered in the multi-tracer approach.

4.3.4 Comparison of the individual dating tracers

Up to this point, tracer ages analogous to the Piston Flow Model were derived. As discussed in Section 2.3, a distinct age hardly reflect the hydrological system; instead, an age distribution is required. As the sampled wells have broad but limited screens, multiple flow lines with different residence times are tapped. In addition, mixing within the aquifer due to different flow paths and velocities has to be taken into account. Hence, the Dispersion Model (DM) is chosen to be the most suitable Transit Time Distribution. According to Section 2.3, a Peclet number of $Pe = 10$ is chosen for all calculation, leaving the Mean Residence Time (MRT) the only free parameter.

To compare two individual dating tracers, their concentrations are plotted against each other in *synoptic plots* using the Software *Lumpy* by Axel Suckow [Suckow, 2012]. Synoptic plots are a powerful tool as they allow to plot the tracer data in combination with the input functions for all MRTs.

This Section is structured as follows: First, the ^{14}C data are compared to the qualitative $^{4}\mathrm{He}_{\mathrm{rad}}$ age information (Section 4.3.4). In the following, CFC-11 and CFC-12 concentrations are discussed. Finally, CFC-11 and ^{14}C are compared and a mixing model is applied.

Comparison of ^{4}He and ^{14}C data

Using radiogenic helium data from Section 4.3.3 and radiocarbon data from Section 4.3.3, the age information derived for the individual wells can be compared. Generally, $\mathrm{He}_{\mathrm{rad}}$ shows the youngest ages in the upper central plain and higher $\mathrm{He}_{\mathrm{rad}}$ levels further downstream (well 19) and in the Western Plain, as well as an excess of $\mathrm{He}_{\mathrm{rad}}$ in the Eastern plain. Meanwhile, the lowest (uncorrected) radiocarbon ages are found for wells 1, 25, 33 and 66 while wells 20 and 58 show increased ages. The highest ^{14}C levels are found in well 19.

Both tracers estimate the wells located in the freshwater zone (salinity categories in Section 4.3.1) to be among the youngest, only well 20 exhibits comparably high ^{14}C levels. The Pearson Model, however, corrects for alterations in δ^{13}C and predicts a groundwater age in the same range as wells 25 and 33. Hence, the $\mathrm{He}_{\mathrm{rad}}$ and the ^{14}C age data are in good agreement for the freshwater zone.

Well 19 located in the brackish zone further downstream in the central plain is expected to indicate a higher groundwater age as the water travels a longer distance from the infiltration area. This trend is seen in both tracers.

While wells 58 and 66 in the Western plain exhibit higher He_{rad} levels, in uncorrected ^{14}C this trend is only seen for well 58. In addition, the Pearson model predicts the age of well 58 to be similar to those in the freshwater zone. This may be due to mixing with modern components (seawater intrusions and infiltrated wastewater). Generally, the wells in the Western plain show corresponding tendencies in He_{rad} and Pearson-corrected ^{14}C. However, increased levels with respect to the central plain are not found in the Pearson Model data.

The highest discrepancy is found for well 1 located in the Eastern brackish zone. While both corrected and uncorrected ^{14}C data indicate a groundwater age in the range as the freshwater wells 20,25 and 33 or younger, He_{rad} exceeds all other wells by an order of magnitude.

To conclude, the tracers ^{4}He and ^{14}C deliver consistent results for most of the wells but leave open questions on the hydrodynamic and hydrogeological behaviour which is outlined in Section 4.4.

Synopsis of CFC-11 and CFC-12

In this section, the age results derived by CFC-11 and CFC-12 are compared. To this end, their possible output curves for all MRTs are combined in a synoptic plot using the software *Lumpy*. Details on the program can be found in Suckow [2014]. As the solubility of gases is dependent on input parameters, the software allows to specify infiltration temperature, altitude, salinity and excess air. In addition, the input function can be refined considering a delay, an input factor, an offset, a daughter correction factor, background and production of individual tracers. These values, however, are kept in their default settings. As the input parameters are applied to all wells, mean values of the data displayed in Table 4.2 are computed. The following input parameters are used:

$$\begin{aligned} \text{infiltration temperature}: &\quad 24\,^{\circ}\text{C} \\ \text{infiltration altitude}: &\quad 500\,\text{m} \\ \text{salinity}: &\quad 1\,‰ \\ \text{excess air}: &\quad 2\,\text{cc(STP)/kg} \end{aligned}$$

The synoptic plot in Figure 4.14 shows the CFC-11 data measured at the wells in dependence of the CFC-12 data. In addition, possible output combinations of CFC-11 and CFC-12 are plotted for three different Transit Time Distributions. CFC input functions are provided by USGS [2017]. As mentioned before, the Dispersion Model with $Pe = 10$ reflects best the hydraulic behaviour of the groundwater system. The numbers labelling specific points on the lines are the mean residence times (MRTs). Hence, the synoptic plot encompasses three dimensions.

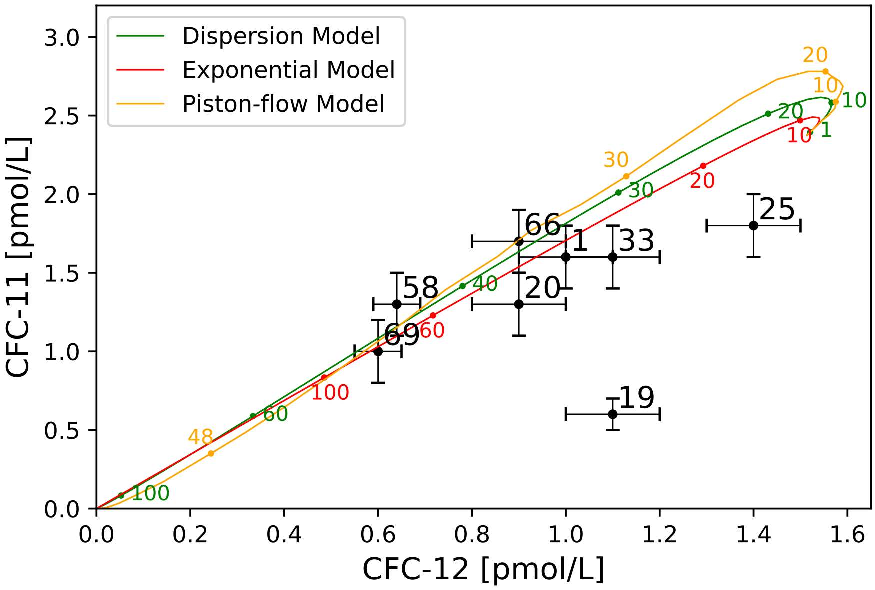

Figure 4.14: Synoptic plot of the CFC-11 and CFC-12 data including their possible output functions at all MRTs for different Transit Time Distributions.

The differences between the TTDs becomes obvious, especially for the part of the curves in the lower left corner of the plot. An MRT in the range of 50 years for the Piston-flow Model corresponds to an MRT of about 80 years in the Dispersion Model and even more than 100 years in the Exponential Model. The first conclusion drawn from this plot is that the Piston-flow CFC ages in Section 4.3.3 are underestimated, given that the Dispersion Model is the more realistic model.

Consistent CFC-11 and CFC-12 data would result in data points that are all located along the output line of the Dispersion Model. The individual wells could be simply assigned to the respective MRT on the graph. Effectively, the data are distributed around the graph with a tendency to an excess in CFC-12. Most wells show a high level of agreement with respect to their CFC-11 and CFC-12 data, except for wells 19 and 25. From the graph it can be read that the CFC-11 DM age of well 19 is in the order of 60 years while CFC-12 data would indicate a DM age of about 30 years. Thus, either a depletion of CFC-11 is present or a (small) contamination with CFC-12. The only process leading to CFC-11 depletion described in literature is microbial degradation under anaerobic conditions in the groundwater. Indeed, field data in Table 4.2 reveals a lower oxygen content in well 19 than in the other sampled wells. However, O_2 is not consumed entirely and the conditions can still be considered aerobic. Thus, CFC-11 consumption can be ruled out and a contamination with CFC-12 is presumed. An additional argument emphasizing the credibility of CFC-11 as a tracer is its higher solubility leading to a lower susceptibility to unconsidered air entrapments. If excess air is underestimated as implied in Section 4.3.3, the error in CFC-12 would be larger than in CFC-11. On top of that, well 19 is located downstream from the freshwater zone wells (20, 25 and 33), so a decrease in CFC levels indicating older groundwater is expected. This trend is only seen in CFC-11. Well 25 is expected to be in the same data range as wells 20 and 33 but shows substantially more CFC-12. For CFC-11, the difference is not significant. Hence, CFC-11 is anticipated the more reliable tracer and is chosen over CFC-12 for comparison with ^{14}C.

Synopsis of CFC-11 and ^{14}C

As ^{14}C and CFCs cover different age ranges, the comparison of age data derived from those two tracers is of particular interest. While CFCs are used to date young water (<100 years), radiocarbon is suitable for ages in the order of a few thousand years.

Synopsis with one water mass In Figure 4.15, the synoptic plot of CFC-11 and ^{14}C is shown. The input parameters are chosen similar to the previous section, with a ^{14}C background of 1 before the bomb peak. The bomb peak is best visible in the Piston-flow Model where a distinct ^{14}C maximum is pronounced for an MRT of 48 years. In the Dispersion Model and the Exponential Model, this maximum is superimposed with ^{14}C concentrations of other ages as they assume an age distribution rather than a distinct age. Like in the previous section, the Dispersion Model is the TTD of choice. The Piston-flow Model and the Exponential Model are not taken into further consideration.

It is evident that the output curve of the Dispersion Model approaches CFC-11 values of zero for ages higher than 100 years. Hence, for the radiocarbon ages calculated in Section 4.3.3 the samples should barely contain any CFC-11 at all. In contrast to this expectation, the data points of the wells are all located far off the DM output curve and a mean residence time cannot be deduced. This may be due to to the fact that *Lumpy* uses raw ^{14}C data rather than a correction model. The only correction model applicable in the context of the software is the Vogel model. This would be done by setting the input factor in the parameters to 0.8, corresponding to the Vogel correction factor. Nevertheless, this correction alone cannot account for the deviation of the two tracer data sets.

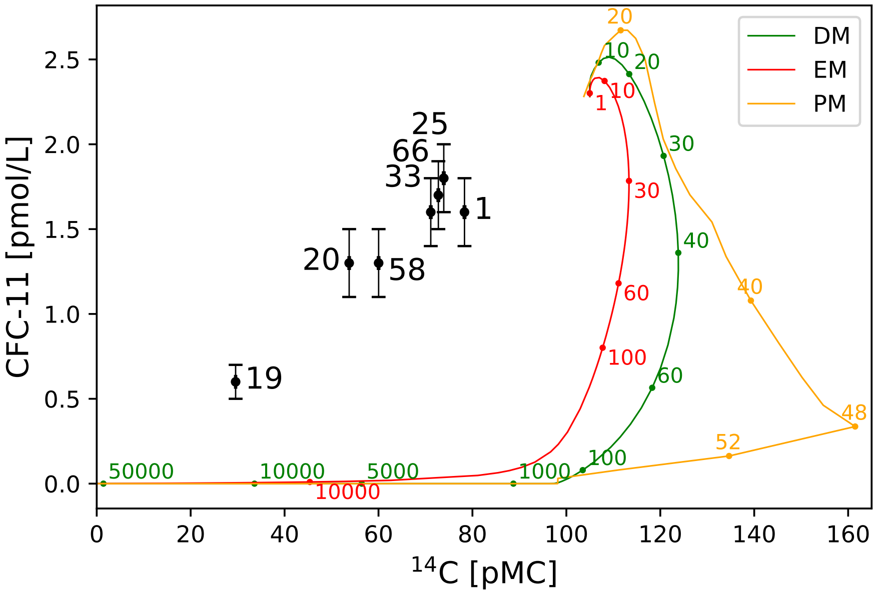

Figure 4.15: Synoptic plot of CFC-11 and the uncorrected ^{14}C data including their output functions at all MRTs for different Transit Time Distributions.

Mixing of two water masses As the discrepancy between CFC-11 and ^{14}C cannot arise within a single water mass, a mixing model is applied as described in 2.3. *Lumpy* allows to mix two water masses with different input parameters and assign MRTs and mixing ratios to the individual measurements. For all wells except well 58, a young water mass may originate from water infiltrated at lower altitudes with a shorter distance travelled through the subsurface. Hence, the input parameters of water mass B reflect results from noble gas thermometry at zero altitude. In addition, the Vogel correction is applied to the ^{14}C output curve as described above. This leads to the input parameters

This leaves three parameters open, i.e. the MRT of water mass A ($\mathrm{MRT_{old}}$), the MRT of water mass B ($\mathrm{MRT_{young}}$) and the mixing ratio r of the two. Hence, the system of equations is underconstrained yielding a solution space rather than a fixed configuration of parameters for each well. However, a quantification is of interest and the three parameters have to be narrowed down. Based on plausibility arguments

	water mass A	**water mass B**
infiltration temperature :	24 °C	26 °C
infiltration altitude :	500 m	0 m
salinity :	1 ‰	1 ‰
excess air :	2 cc(STP)/kg	2 cc(STP)/kg
delay :	0 (default)	0 (default)
input factor :	0.8	0.8
offset :	0 (default)	0 (default)
daughter correction factor :	0 (default)	0 (default)
background CFC-11 :	0 (default)	0 (default)
background ^{14}C:	1	1
production :	0 (default)	0 (default)

and considerations of valid results, the MRT of the young component is the most predictable figure. Consequently, a value of $\mathrm{MRT}_{\mathrm{young}} = 10$ years is assumed and kept constant for the following data evaluation.

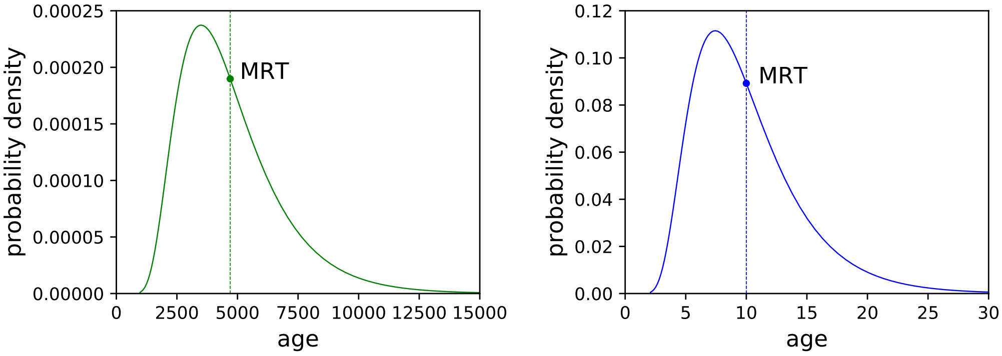

Figure 4.16: Age distribution within the old (left) and young (right) component for $\mathrm{MRT}_{\mathrm{old}} = 4700$ years (plausible for wells 25, 33 and 66).

The age distributions of the old and the young component in the Dispersion Model are depicted in Figure 4.16. The MRT of the old component ($\mathrm{MRT}_{\mathrm{old}}$) was chosen 4700 years (suitable for well 25). As the probability density of the young component exceeds that of the old component by factor 1000 it is not practical to plot the age distribution of the mix of the two water masses.

The synoptic plot with two water masses is depicted in Figure 4.17 where a mixing line between the young component and the old component (here with $\mathrm{MRT}_{\mathrm{old}} = 4700$ years) is drawn. The numbers labelling different positions on the mixing lines designate the ratio r of the young component B. For instance, well 25 with $r = 0.71$ is described as a mix of 71 % young water and 29 % old water. The result of concern at this point is the $\mathrm{MRT}_{\mathrm{old}}$ of 4700 years as it represents the groundwater age of the old component corrected for the young contribution.

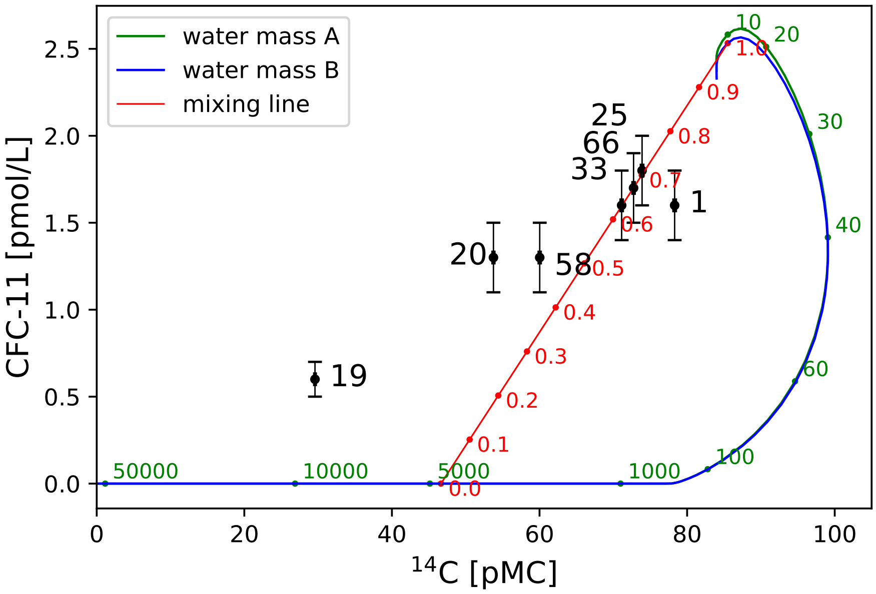

Figure 4.17: Synoptic plot of CFC-11 and the (Vogel corrected) ^{14}C data including their input functions at all MRTs for two water masses. Water mass A is the old component ($\mathrm{MRT}_{\mathrm{old}}$=4700 yrs), water mass B is a young component ($\mathrm{MRT}_{\mathrm{young}}$=10 yrs). The mixing line of the two water masses intersects data of wells 25, 33 and 66.

$\mathrm{MRT}_{\mathrm{old}}$ in Figure 4.17 was chosen aiming to intersect the data points of wells 25, 33 and 66. Hence, those three wells can be assigned the same $\mathrm{MRT}_{\mathrm{old}}$ (water mass A) of 4700 years, with varying ratios of the young water component. This is done for all wells. The results are found in Table 4.4. The upper and lower errors of $\mathrm{MRT}_{\mathrm{old}}$ are quantified using the error margins of CFC-11.

According to the multi-tracer approach, only wells 25, 33 and 66 can be grouped together whereas none of the $\mathrm{MRT}_{\mathrm{old}}$ values of the other wells coincide. In particular, well 20 is substantially older than the wells 25 and 33 although they are all located in the same zone in the upper central plain. In addition, the error bounds are remarkably large. On the other hand, well 19 exhibits the highest $\mathrm{MRT}_{\mathrm{old}}$ and a low share of the modern component as expected. In the Western plain, well 66 located at the foot of the mountains is estimated to be in the same age range as the freshwater zone wells whereas the coastal well 58 is older. Surprisingly, well 1 in the brackish Eastern Plain is significantly younger than the freshwater zone wells 20, 25 and 33.

All those aspects only consider relative observations between the wells. Looking at the absolute numbers, $\mathrm{MRT}_{\mathrm{old}}$ seems eminently high and the uncertainties are large. Besides, the share of the young component is higher than 50 % for all wells except for well 19. Those findings are important for the applicability of a mixing model in this study. In addition, at this point it is important to note that all findings are based on the assumption that the mean residence time of the young component is kept constant at $\mathrm{MRT}_{\mathrm{young}} = 10$ years. This may not be true for all wells and the results of $\mathrm{MRT}_{\mathrm{old}}$ and the ratio r have to be treated with caution, as outlined in the discussion (Section 4.5).

well	$\mathrm{MRT}_{\mathrm{old}}$ [yrs]	$\mathrm{MRT}_{\mathrm{young}}$ [yrs]	ratio r
1	$1650\,^{+600}_{-500}$	10	0.63
19	$19000\,^{+4000}_{-3000}$	10	0.24
20	$13000\,^{+10000}_{-3800}$	10	0.51
25	$4700\,^{+3500}_{-1200}$	10	0.71
33	$4700\,^{+2500}_{-1200}$	10	0.63
58	$8000\,^{+3500}_{-2000}$	10	0.51
66	$4700\,^{+3000}_{-1200}$	10	0.67

Table 4.4: Mean residence times and ratios of the water masses in the Dispersion Model.

4.4 Interpretation

In this section the data presented in the previous section are interpreted. The center, the East and the West of the plain are discussed individually.

Central plain Four wells were sampled in the central plain, of which wells 20, 25 and 33 are part of the freshwater zone at the foot of the Dhofar mountains whereas well 19 is located further downstream towards the coast. Generally, data in the central plain produce consistent results with rather young ages in the upper plain and increased tracer ages further downstream. This is in good agreement with former findings of a high groundwater flow rate in the center of the plain due to a good hydrogeological connection to the Dhofar mountains in that area Brueckmann et al. [2017].

In contrast to the coherent picture, well 20 shows ambiguous results. While ^{4}He and CFC data suggest a tracer age in the same range as wells 25 and 33, the ^{14}C age (and hence, $\mathrm{MRT_{old}}$) is significantly older. The Pearson model, however, corrects for this effect by taking into account δ^{13}C measurements and assigns well 20 a tracer age in agreement with the expectations.

Ignoring the Western plain, the measured SF_6 concentrations are increasing starting in the East and going westwards, so from well 1 over wells 20 and 33 to well 25. The highest SF_6 concentrations are found in well 19. As CFCs do not exhibit a similar behaviour, this geographical tendency may indicate a subsurface production of SF_6 in the center (and, to a lower extent, in the East) of the plain. However, this finding cannot be made use of for this study as the effect is unquantifiable and hence, cannot be corrected for.

Western plain Wells 66 and 69 were sampled in the Western plain whereby the measurement of ^{14}C was only possible for well 66. Both wells supply water to a storage tank in a few hundred meters distance from the borehole using a permanently installed pump. Hence, the hydraulic head and the groundwater flow are altered from natural conditions and the data have to be treated with caution.

In the Western plain wells, a discrepancy between different tracer data is apparent. Both wells seem to be rather young (i.e. only slightly older than the central plain) in CFC tracer age but exhibit substantially higher concentrations of radiogenic ^{4}He. The ^{14}C analysis of well 66 also indicates a tracer age in the same range as the wells in the central freshwater zone. These ambiguous findings exacerbate a conclusion regarding the flow rate in the West compared to the center. Geological models of the plain indicate a better hydrogeological connection in the central area than at the sides [Brueckmann et al., 2017]. While helium data substantiate this expectation, ^{14}C and CFC tracer ages do not exhibit a trend of that kind. This behaviour may originate from the admixture of a very old water mass from depth enriched in helium. In contrast to the central plain, no or only a marginal SF_6 production is evident in the Western plain as the CFC and SF_6 data are in good agreement.

Eastern plain Only one well was sampled in the Eastern plain. Salinity levels in the Eastern plain are generally higher than in the center and the West which is why it is sometimes referred to as the Eastern brackish zone. This area was chosen for investigation as former results of the IATI-SGD project revealed exceedingly high ^{4}He concentrations and even suggested a reversed flow from the coast towards the mountains [Mueller, 2018].

Among all locations sampled in this study, well 1 shows the highest discrepancy between the calculated tracer ages. While both CFCs and ^{14}C data (corrected and uncorrected) indicate a tracer ages comparable to the central wells 20,25 and 33, the calculated radiogenic ^{4}He concentration surpasses all other wells by an order of magnitude. Although this sudden increase with respect to concentrations in neighbouring wells remains an open question, similar results have been produced in the scope of the IATI-SGD project. Hence, this finding is reproducible. As mentioned above, a possible explanation would be the admixture of very old groundwater in the Eastern plain, perhaps from a deeper reservoir, with a high concentration of radiogenic helium. This is substantiated by the identification of geological fault zones [Brueckmann et al., 2017]. However, the geology of the area is not understood well enough to confirm presumptions on old water components and is not subject of this thesis.

Apart from ^{4}He results it is remarkable that well 1 is the youngest of all sampled wells with respect to $\mathrm{MRT}_{\mathrm{old}}$ although it is not located closer to the infiltration area. This is in contrast to the expectation that the highest flow rate would be found in the central plain.

4.5 Discussion

The data of the dating tracers ^{4}He, ^{14}C, CFCs and SF_6 do not yield a consistent age information for all of the sampled locations. Possible reasons are outlined in this section. First, influences of the environment leading to contradicting results are considered. Subsequently, technical aspects and the applied methods are discussed.

Environmental influences on tracer data

Generally, tracer ages may be influenced by various effects. First, deriving a tracer age using the Dispersion Model or even the Piston-flow Model assumes a water mass originating from the recharge area and a (dispersive) flow towards lower head gradients. However, the potentiometric surface of the Salalah Plain is not in its natural state. Excessive groundwater abstraction lowers the hydraulic head locally and thus, induces a flow towards areas of pumping. This is primarily relevant for wells 19, 66, 69 and 58 as they are located downstream or in vicinity of extraction points. In addition, an irrigation return flow in agricultural areas may depict a modern component in the groundwater. This is potentially accounted for in the mixing model which is outlined below. An influence of seawater intrusions is not expected to be seen for any of the wells except for well 58. This particular well is presumably also affected by wastewater infiltrated along the coastline as outlined in Section 4.1.1. The westernmost infiltration bore is located in about 3 km distance East of well 58 and the flow velocity is estimated to be around 600 meters per year, resulting in a travel time of about 5 years [Shammas, 2008]. Hence, infiltrated wastewater represents a substantial modern component to well 58. Those aspects all consider the mixing of the monsoon-originated groundwater with a modern component.

In addition, particularly old water components may deflect the tracer concentrations in the aquifer. As mentioned above, old groundwater from depth may intrude in the Eastern or the Western plain. This is a possible explanation for the raised helium levels with respect to the central plain. Another potential influence is described in Brueckmann et al. [2017]: As the Salalah Plain was submerged by the ocean in the geological past, deposits from about 35 000 years ago [Leroy et al., 2012] may induce changes in the tracer concentrations. However, this proposition is solely of speculative nature and cannot be further investigated in the scope of this thesis.

Finally, several processes in the soil may influence the tracer data directly. Apart from the mentioned subsurface production of SF_6, also CFCs may be concerned. While a rise in CFC concentrations may originate from anthropogenic actions (e.g. effects of irrigation and pesticides, leaks in sewage lines and waste disposal), microbial degradation of CFC-11 (and, to a lower extent, CFC-12) has been found in anaerobic soils [IAEA, 2006]. However, none of those aspects considering CFCs seems to be evident in the study area.

Critical review of the applied methods

In a next step, the tracer methods the data are based on have to be discussed. Those encompass the quantification of excess air with noble gases as well as the derivation of a tracer age with ^{4}He, ^{14}C, CFCs and SF_6. A Transit Time Distribution is chosen to represent the hydrodynamic system. In addition, synoptic plots help to compare the tracer data and a mixing model corrects for modern components.

Excess air was derived from measured noble gas concentrations as described in Section 2.2.3. As the focus of this work lies on dating tracers, the most simplified model was used assuming the complete dissolution of entrapped air without fractionation. This may not reflect the actual process rigorously. However, the deviation to other excess air models was quantified by comparison with data processed by Werner Aeschbach and found to be negligible.

^{14}C tracer ages generally have to be treated with caution as carbon is susceptible to fractionation and involved in a variety of chemical and biological processes. As a consequence, a variety of correction models have been developed and were applied for this study. The **Vogel model** is based on empirical findings and causes a (constant) age shift towards younger ages. Hence, properties specific to the study area are not taken into account and the model serves rather as an estimation of the ^{14}C tracer age. The **Tamers model** is disregarded for this study as the correction shifts the tracer ages towards negative (i.e. hypermodern) ages.

The **Pearson model** was modified in order to realize it in this study. This model is considered the most reliable age estimation as it includes the δ^{13}C data of the wells. However, the isotopic signature of the end members, especially soil air, is not sufficiently defined as measurements of the pH in the infiltration area are missing. As outlined in Section 4.3.3, this is accounted for by calculating a tracer age range rather than a distinct age. For almost all wells, this yields tracer ages up to modern values.
In addition to those critical aspects concerning the correction models, ^{14}C may not be an ideal dating tracer for the study area as it covers the dating range of 1000 - 30 000 years. The age resolution decreases for younger samples and an exact dating of the groundwater is not feasible. Previous attempts for groundwater dating in the study area did not yield consistent results (compare Section 4.1) which is why in this study, multiple dating tracers covering different ranges were applied in the first place. Hence, the complications with radiocarbon dating can be seen a result of this study, indicating that this tracer is simply not suitable for groundwater dating in the Salalah Plain and that dating tracers compatible with younger water are required. Finally, it is worth emphasizing that in contrast to previous ^{14}C applications in the

Salalah Plain, no contamination with atmosphere was evident in this study.

Furthermore, tracer ages were calculated using **CFC-11, CFC-12, CFC-113 and $\mathbf{SF_6}$**. Generally, a trend is seen in the data: For almost all wells, SF_6 yields the youngest ages, followed by CFC-113, CFC-12 and CFC-11. Interestingly, this corresponds to their solubility at infiltration temperatures of about 25 ℃ , as depicted in Figure 2.5. The smaller the solubility of a substance, the younger is its calculated tracer age. A similar behaviour would be seen if excess air was not taken into account as entrapped air has a higher influence on substances with low solubility. This may suggest that for the calculation of CFC and SF_6 groundwater ages, the effect of excess air was underestimated. However, this cannot account for all CFC-113 and SF_6 data that had to be excluded from analysis due to contamination as immensely high excess air values in the order of 1000 cc/kg would be required to produce similar tracer ages. In addition, at temperatures around 25 ℃, the solubility of CFC-113 is not significantly less than that of CFC-12. Therefore, it is rather unlikely that the difference in age can be entirely affiliated to an underestimation of excess air. However, it may indicate some other kind of contact with (modern) air.

CFCs and SF_6 are very susceptible for contamination, hence, the results yielding tracer ages younger than 50 years have to be treated with caution. Mistakes during sampling may induce major changes in the resulting tracer ages. Those encompass insufficient flushing of the sample container with sample water producing samples with residue atmosphere-equilibrated water as well as the neglection of an enclosed air bubble. In addition, as the tubing is stored in contact with atmospheric air, CFCs may diffuse into the material. This effect has been found to affect CFC-11 and CFC-113 more than CFC-12 [IAEA, 2006]. While the results do not reveal lower CFC-11 tracer ages than those calculated from CFC-12, CFC-113 tracer ages are indeed younger. In addition, it is remarkable that exceeding CFC-113 concentrations are found for all wells sampled by the conventional technique whereas the shallow well 58 and the water tanks 66 and 69 exhibit reasonable concentrations. Apart from possible effects from the MP1 pump itself, a correlation between the length of tubing material and the contamination in CFC-113 is visible. Taking data for the height of the vadose zone from table 4.1 shows that wells 1 - 33 all required a minimum hose length of about 20 - 80 meters. For well 58, the hose was shortened to a length of <15 m to reduce the resistance. Sampling at wells 66 and 69 only required hoses of a few meters length. Hence, outgassing of CFC-113 from the tubing material constitutes a realistic source of contamination. This could be avoided by storing the sampling equipment in water.

The type of **Transit Time Distribution** chosen to represent groundwater flow is of great importance for the resulting tracer age. This is seen in Figures 4.14 and 4.15 where output curves for different types of TTDs were plotted. The Dispersion Model is suggested to represent the age distribution in the sampled water body. However, for the first part of the age data analysis (Section 4.3.3) the Piston-flow Model is used for simplicity. The calculations are performed without a modelling software. Especially for the analysis of CFCs and SF_6 the tracer solubility in water was calculated for each well individually. In the second part of the age data analysis (Section 4.3.4) the software *Lumpy* was applied and the Dispersion Model was used. However, the software uses the same gas solubility for all wells which limits the accuracy of the tracer ages. Hence, both parts of the age data analysis ignore an aspect in the calculation.

A similar situation is found for **^{14}C correction models**. While in Section 4.3.3 an extensive consideration of different correction models is found, the software *Lumpy* only supports the Vogel model. As the Vogel model is rated less reliable than the Pearson model, this results in an incomplete consideration of the environmental conditions on site. In particular, well 20 is concerned as the Pearson correction has a large effect on its radiocarbon age. This results in an overestimation of MRT_{old} (Table 4.4) and explains why it is older than the two other freshwater zone wells.

Synoptic plots are useful tools to illustrate the measured concentrations of two tracers. However, for the synopsis of CFC11 and ^{14}C a large difference in the suitable age range of the two tracers is present. At the same time, the measured concentrations of the two tracers show immense discrepancies with respect to the possible combinations at different mean residence times. Those can only be accounted for by applying **mixing models**. The large gap between the two tracer ages can only be explained by a mixture of very young and very old water. The MRT of the young component is assumed and kept constant while the MRT of the old component (MRT_{old}) is derived for each well individually. However, to result in the tracer combinations found in the wells, this requires MRTs in a range of poor resolution. In other words, the abundance of CFC-11 combined with low ^{14}C activities limits the accuracy of $\mathrm{MRT}_{\mathrm{old}}$.

Another aspect of the mixing models worth discussing is the factor r determining the ratio of the young component in the groundwater. The calculated values of all wells are listed in Table 4.4. The ratio of the young component ranges from about 0.25 to 0.7 which is many times higher than the expected values. Originally, a mixing model aims to correct for small modern contributions slightly varying the tracer concentrations. The essential result is the MRT of the old component, $\mathrm{MRT}_{\mathrm{old}}$, as this is the prevailing quantity for an accurate description of the hydrological system. However, for young ratios of this extent, it remains unclear whether the hydrological system can indeed be characterized by the MRT of the old component alone.

For the parameters of the young component, it is assumed to originate from recent precipitation infiltrated at low altitudes. In addition, other sources like irrigation return flow, seawater intrusions or infiltrated wastewater may be involved as outlined in Section 4.5. This can be verified by comparing the ratio of well 58 with the other ratios as well 58 is known to be influenced by those components while most other wells are not. However, the ratio of the modern component in well 58 is below the mean ratio of the other wells. Hence, the origin of the young component can be restricted to recent precipitation from low altitudes or atmospheric contamination.

To conclude, a variety of aspects may have influenced the calculated tracer ages. In this thesis, the accuracy of the groundwater age investigation is limited by the set of tracers and more information needs to be derived using additional dating tracers. For this reason, samples for tritium (^{3}H) analysis were taken during the campaign as it represents a valuable dating tracer for young water (1 to 50 years)[IAEA, 2013]. In contrast to CFCs and SF_6 it is not susceptible to contamination with atmospheric air. In addition, dating with ^{39}Ar covers ages between 50 and 1000 years which is the expected groundwater age range in the study area. Hence, the groundwater in the Salalah Plain will be dated with both ^{3}H and ^{39}Ar subsequent to this thesis. Those results are of great significance for the prospective interpretation of the data and will play a key role in revealing the flow of the groundwater system in the Salalah Plain .

5 Summary and Outlook

In the course of this thesis, technical aspects of the sampling and purification of argon for dating with ^{39}Ar were improved. Those progresses were applied in a multi-tracer study in Southern Oman with the objective to investigate groundwater ages at different locations in the Salalah Plain.
For groundwater dating with ArTTA, water samples are degassed and the argon is separated in a purification setup at the Institute of Environmental Physics (IUP) in Heidelberg. To enable the estimation of the extracted air volume for small samples, a calibration curve for a reduced inner volume was recorded and a pressure-volume conversion factor was determined. In addition, a conversion factor for the original inner volume was calculated and compared to former results which served as a measure for the uncertainty.
The purification process is monitored by seven pressure gauges at different locations within the setup. To simplify the monitoring and render the procedure more user-friendly, the pressure readout was automated. A Labview program was written comprising the readout, record and visualization of the pressures. In addition, the program enables volume estimations of the extracted gas and the residual pure argon. An alarm system serves to warn the user when pressures approach ranges that are not supported by the pressure gauges. For sudden pressure jumps, the program protects the hardware by switching off several pressure gauges and is capable to switch them back on again. The software is in frequent operation during sample purification and further improvements will be implemented on a regular basis.

In the context of an ongoing project between the ***I**nstitute of **A**dvanced **T**echnology **I**ntegration (IATI)*, Oman, and the Helmholtz Centres *GEOMAR* (Kiel) and *UFZ* (Leipzig), referred to as the IATI-SGD project, a multi-tracer study in the Salalah Plain was planned and realized. The principal objective was the investigation of the groundwater ages with several dating tracers. Besides measurements for determination of the groundwater chemistry, the applied tracers were noble gases, ^{14}C, ^{39}Ar, CFCs and SF_6. Excess air was calculated using measured neon concentrations in the groundwater and the results were taken into account for the dating tracers. A qualitative dating approach was performed by radiogenic ^{4}He. Former results indicating unusually high concentrations in the Eastern plain were reproduced and also the Western plain exhibited increased radiogenic helium with respect to the center. Using ^{14}C data radiocarbon ages were calculated and correction models by Vogel [1967], Tamers [1975] and Pearson JR. [1965] were applied. In contrast to former studies, no contamination was evident. The Tamers model did not produce realistic results and was disregarded whereas modifications in the Pearson model helped to restrict the groundwater to ages younger than 3000 years (except for one well). The argon was purified but could yet not be measured by ArTTA due to technical complications. Finally, CFCs and SF_6 tracer ages were calculated and ranged between 20 and 40 years. A high number of samples were contaminated in CFC-113 and SF_6. Potential contamination sources for CFC-113 were discussed and potential areas of SF_6 subsurface production were identified. CFC-11 and CFC-12 data were mostly in good agreement except for one well.

For the intercomparison of the individual tracers the data was visualized in *synoptic plots*. Among the young tracers, CFC-11 was chosen over CFC-12, CFC-113 and SF_6 and was plotted with respect to ^{14}C to derive the mean residence time of the old component in the groundwater. Results ranged from less than 2000 years up to 19 000 years which exceeded the expected age range by far.

Unfortunately, the tracer data did not yield a consistent age information for the eight sampled locations. Further investigations in the context of the IATI-SGD project are required and will be made subsequent to this thesis.

In addition to the correction models applied in this thesis, further considerations can be included in the analysis of the ^{14}C data. Further measurements of δ^{13}C in the infiltration area (Dhofar mountains) may help to improve the accuracy of the Pearson model. As no data on the plant distribution of types C3 and C4 was available, vegetation effects were ignored and are to be taken into account prospectively. After implementing those aspects in the Pearson model, the model can be applied to synoptic plots with other tracers. As the software *Lumpy* is not able to use δ^{13}C data, this has to be done in two steps. First, the Pearson correction needs to be calculated as done in this thesis. In the following, the corrected ^{14}C data are entered into *Lumpy*.

Furthermore, measurements of the pH and the partial pressure of soil CO_2 in the infiltration area may allow for the application of the *Chemical mass balance* model. In this model the ^{14}C-active Dissolved Inorganic Carbon is compared to total carbonate content at the time of sampling [Clark and Fritz, 1997]. Finally, in an extensive investigation with *NETPATH* a geochemical mass balance for the mixing process of up to five initial waters can be made USGS [2017]. The required data of major ion concentrations in the groundwater were gathered by Thomas Müller, UFZ during the field campaign in May 2018.

For the analysis of the CFC tracer ages, the lag time for CFC diffusion through the unsaturated zone was ignored in this thesis. This effect may lead to an overestimation of the CFC tracer age and produce an even higher discrepancy between results of CFCs and ^{14}C. However, the lag time can be estimated by measurements of the CFC concentration in the unsaturated zone [Cook and Solomon, 1995].

Generally, the main reason for the incomplete hydrological picture was the lack of data from reliable dating tracers. Although tracers for the hydrochemistry, ^{3}H and - above all - ^{39}Ar were sampled in the field campaign, the results were not available at the time of writing this thesis. However, they will be investigated in the further progress of the IATI-SGD project. As mentioned above, hydrochemical data can be used for a ^{14}C analysis with NETPATH. ^{3}H covers an age range similar to CFCs and SF_6 but is not equally susceptible to contamination [IAEA, 2006]. Hence, it can serve as a validation of the data presented in this thesis. Most notably, the most promising tracer of this field campaign, ^{39}Ar, offers an ideal dating range while it is not involved in chemical or biological processes due to its inertness. Prospectively, investigation of ^{39}Ar activities and the synoptic combination with tracer data from ^{14}C, ^{3}H and CFC-11 may allow for a better hydrogeological understanding of the groundwater flow in the Salalah Plain.

6 Appendix

6.1 Solubility of gases in water

The data displayed in Figure 2.5 in Section 2.1.5 are derived in the following ways:

CO_2 data are taken from Aeschbach [2017]. The values are converted using

$$L = \frac{1}{K'_\mathrm{H}} = \frac{R \cdot T}{K_\mathrm{H}} \tag{6.1}$$

$$\text{with} \quad \begin{array}{rl} R = 0.08206\,\frac{\mathrm{atm\,L}}{\mathrm{mol\,K}}: & \text{universal gas constant[Aeschbach, 2017]} \\ T: & \text{temperature in Kelvin} \quad . \end{array}$$

The solubility of the noble gases is calculated using

$$\ln \beta = t_1 + t_2 \cdot \frac{100\,\mathrm{K}}{T} + t_3 \cdot \ln\left(\frac{T}{100\,\mathrm{K}}\right) \tag{6.2}$$

with dimensionless coefficients t_i. The salinity is set to zero according to the measured field data.

The solubility of CFC-11, CFC-12, CFC-113 and SF_6 is derived by

$$\ln K_\mathrm{H} = t_1 + t_2 \cdot \frac{100\,\mathrm{K}}{T} + t_3 \cdot \ln\left(\frac{T}{100\,\mathrm{K}}\right) \tag{6.3}$$

which is converted to a solubility using Eq. 6.1.

The solubility coefficients t_i were taken from Weiss [1971] (He and Ne), Weiss [1970] (Ar), Warner and Weiss [1985] (CFC-11 and CFC-12), Bu and Warner [1995] (CFC-113) and Bullister et al. [2002] (SF_6) and are listed in Table 6.1. The calculated Ostwald solubilities are found in Table 6.2.

	He	Ne	Ar	CFC-11	CFC-12	CFC-113	SF_6
t_1	-34.6262	-39.1971	-55.6578	-136.2685	-124.4395	-136.129	-96.5975
t_2	43.0285	51.8013	82.0262	206.115	185.4299	206.475	139.883
t_3	14.1391	15.7699	22.5929	57.2805	51.6383	55.8957	37.8193

Table 6.1: Solubility coefficients t_i for Eq. 6.2 and 6.3.

T	He	Ne	Ar	CFC-11	CFC-12	CFC-113	SF6	CO2
0.1	9.41	12.43	53.49	862.29	209.96	281.13	13.86	75.12
5	9.16	11.78	47.10	643.30	161.91	204.16	11.22	63.23
10	8.97	11.23	41.84	490.99	127.44	151.68	9.22	53.91
15	8.83	10.78	37.59	385.09	102.79	115.86	7.72	46.58
20	8.73	10.40	34.12	309.84	84.83	90.83	6.57	40.65
25	8.67	10.10	31.27	255.34	71.53	72.97	5.69	35.48
30	8.64	9.86	28.93	215.22	61.54	59.98	5.01	
35	8.65	9.67	26.99	185.27	53.97	50.38	4.47	
40	8.69	9.53	25.38	162.70	48.17	43.19	4.04	

Table 6.2: Calculated Ostwald solubility in water in $10^3 \cdot [(\mathrm{mol/L})/(\mathrm{mol/L})]$.

6.2 Block diagram of the automation program

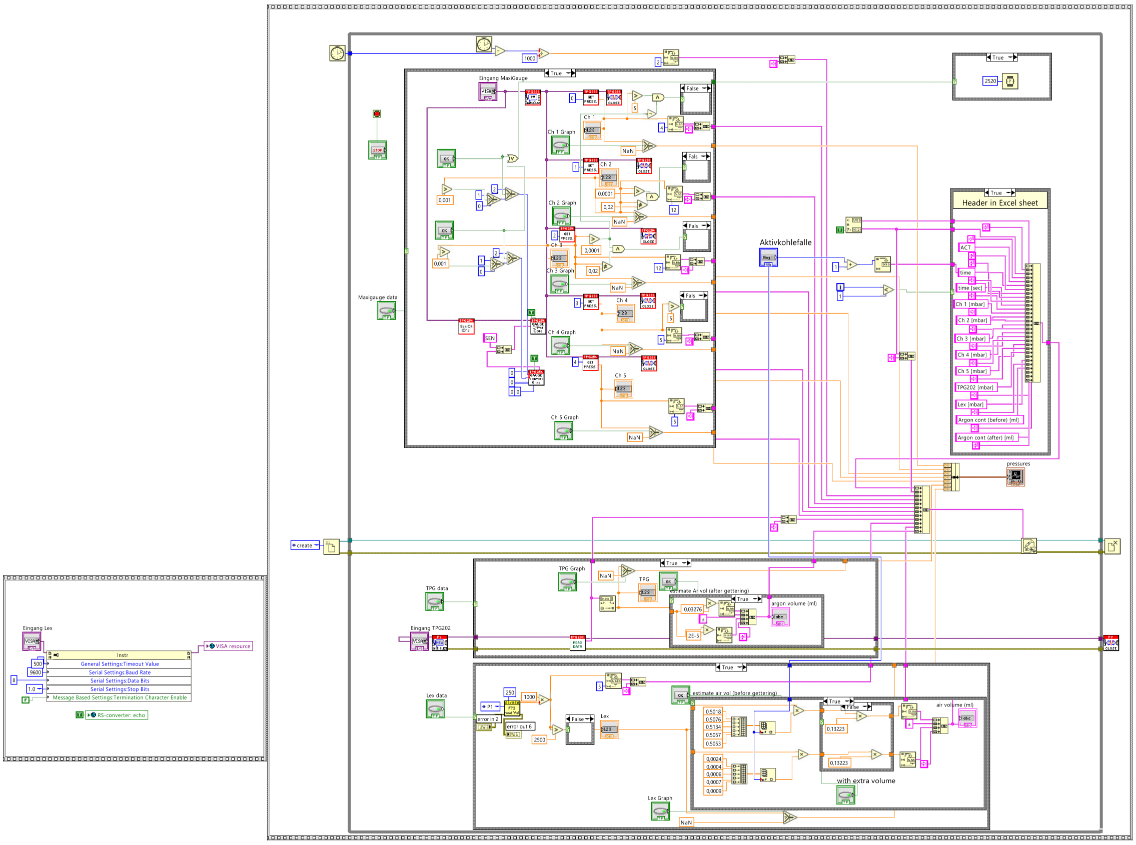

Figure 6.1: Block diagram of the Labview progam for the readout and control of pressure gauges in the argon purification setup.

6.3 Full IDs and geographical locations of the sampled wells

well	well ID	Easting [UTM]	Northing [UTM]
1	BD190195AA	210900	1891500
19	AD999057AA	199500	1890700
20	BD095528AA	205200	1895800
25	AD898401AA	188450	1894100
33	AD999903AA	199000	1899300
58	AD881162AA	181680	1881220
66	001/683	818226	1887231
69	001/669	184926	1890582

Table 6.3: Locations and IDs of the sampled wells.

6.4 Piston-flow radiocarbon data of all correction models

well	uncorrected [yrs]	Vogel [yrs]	Tamers [yrs]	Pearson (min) [yrs]	Pearson (max) [yrs]
1	2 021 ± 15	177 ± 11	-2572	-2601	1117
19	10 070 ± 79	8226 ± 518	4990	3171	6889
20	5 131 ± 38	3287 ± 207	616	-3174	545
25	2 501 ± 18	656 ± 61	-1929	-3682	36
33	2 816 ± 21	972 ± 61	-1469	-1917	1801
58	4 219 ± 31	2375 ± 149	-1174	-2870	848
66	2 631 ± 19	786 ± 49	-2165	-936	2782

Table 6.4: Radiocarbon data for all correction models.

6.5 CFCs and SF_6 Piston-flow data

well	CFC-11 [yrs]	CFC-12 [yrs]	CFC-113 [yrs]	SF_6 [yrs]
1	39.0 ± 3.5	35.5 ± 3.5	-	26.5 ± 2.0
19	48.0 ± 1.5	32.5 ± 3.5	-	-
20	42.0 ± 3.5	37.0 ± 4.0	-	19.8 ± 2.8
25	36.5 ± 3.5	27.5 ± 11.0	-	-
33	39.0 ± 4.5	33.0 ± 3.0	-	-
58	42.5 ± 3.5	43.5 ± 2.0	34.0 ± 3.5	30.5 ± 2.6
66	38.5 ± 4.0	37.5 ± 3.5	32.5 ± 3.0	27.3 ± 2.2
69	44.5 ± 2.0	44.0 ± 2.0	36.0 ± 4.0	31.3 ± 2.5

Table 6.5: Groundwater dating with CFCs and SF_6. Empty lines indicate contaminated samples.

List of Figures

List of Tables

Bibliography

[ICBA 2012] : *Oman Salinity Strategy.* 2012

[Aeschbach 2017] Aeschbach, Werner: *Lecture notes of 'Physics of Aquatic systems'.* 2017

[Aeschbach et al. 2002] Aeschbach, Werner ; Beyerle, Urs ; Holocher, Johannes ; Peeters, Frank ; Kipfer, Rolf: Excess air in groundwater as a potential indicator of past environmental changes. In: *Study of environmental change using isotope techniques.* Vienna : IAEA, 2002, S. 174–183. – URL `http://nbn-resolving.de/urn:nbn:de:bsz:352-243968`. – ISBN 9201164025

[Aeschbach-Hertig and Solomon 2013] Aeschbach-Hertig, Werner ; Solomon, D. K.: Noble Gas Thermometry in Groundwater Hydrology. In: *The Noble Gases as Geochemical Tracers.* Berlin, Heidelberg : Springer Berlin Heidelberg, 2013, S. 81–122. – URL `http://link.springer.com/10.1007/978-3-642-28836-4_5`

[Al-Mashaikhi 2011] Al-Mashaikhi: *Evaluation of groundwater recharge in Najd aquifers using hydraulics, hydrochemical and isotope evidences*, Friedrich Schiller University Jena, PhD Thesis, 2011

[Alley 2002] Alley, W. M.: Flow and Storage in Groundwater Systems. In: *Science* 296 (2002), Nr. 5575, S. 1985–1990. – URL `http://www.sciencemag.org/cgi/doi/10.1126/science.1067123`. – ISSN 00368075

[Andrews et al. 1989] Andrews, J. N. ; Davis, S. N. ; Fabryka-Martin, J. ; Fontes, J. C. ; Lehmann, B. E. ; Loosli, H. H. ; Michelot, J. L. ; Moser, H. ; Smith, B. ; Wolf, M.: The in situ production of radioisotopes in rock matrices with particular reference to the Stripa granite. In: *Geochimica et Cosmochimica Acta* 53 (1989), Nr. 8, S. 1803–1815. – ISBN 0016-7037

[Anker 2010] Anker, Arthur: *Flickr fotostream: Dhofar mountains, southern Oman.* 2010. – URL `https://www.flickr.com/photos/artour_a/5046369762`

[Askri et al. 2016] Askri, Brahim ; Ahmed, Abdelkader T. ; Al-Shanfari, Razan A. ; Bouhlila, Rachida ; Al-Farisi, Khater Ben K.: Isotopic and geochemical identifications of groundwater salinisation processes in Salalah coastal plain, Sultanate of Oman. In: *Chemie der Erde* 76 (2016), jun, Nr. 2, S. 243–255. – URL `https://www.sciencedirect.com/science/article/pii/S0009281915300222`. – ISSN 0009-2819

[Bauer and Yavitt 1996] Bauer, M.R. ; Yavitt, J.B.: Processes and mechanisms controlling consumption of CFC-11 and CFC-12 by peat from a conifer-swamp and black spruce-tamarack bog in New York State. In: *Chemosphere* 32 (1996), feb, Nr. 4, S. 759–768. – URL `https://www.sciencedirect.com/science/article/pii/0045653595003665`. – ISSN 0045-6535

[Bawain 2012] Bawain, Abdullah Mohammed A.: *Influence of Vegetation on Water Fluxes at the Ground Level in a Semi-arid Cloud Forest in Oman*, Friedrich-Schiller Universität Jena, PhD Thesis, 2012

[Bear and Cheng 1999] Bear, J. ; Cheng, A. H.-D.: Seawater Intrusion in Coastal Aquifers: Concepts, Methods and Practices. URL `http://link.springer.com/10.1007/978-94-017-2969-7_1`, 1999, Kap. Introducti, S. 1–8

[Beiser 1957] Beiser, A.: Variations in the geomagnetic dipole in the past 15,000 years. In: *J. Geophys. Res.* 62 (1957), Nr. 2, S. 235–239

[Bennet and Kaye 2018] Bennet, Mikaela ; Kaye, Josh: *Desalination and Climate: How the Restructuring of Water is Shaping Oman*, George Washington University, Dissertation, 2018

[Beyersdorfer 2016] Beyersdorfer, S: *Argon extraction from glacier ice and ocean water for dating with ^{39}Ar - ATTA*, University of Heidelberg, Master's thesis, 2016

[Bredehoeft 2002] Bredehoeft, John D.: The water budget myth revisited: Why hydrogeologists model. In: *Ground water* 40 (2002), S. 340–345

[Britannica 2018] Britannica, Encyclopedia: *Water cycle.* 2018

[Brueckmann et al. 2017] Brueckmann, Warner ; Schmidt Patrick Leibold Hajar Al Balushi GEOMAR, Mark ; Friesen Thomas Mueller, Jan ;

Al-Busaidi, Ghaliya: Submarine Groundwater Discharge Adaption of an autonomous aquatic vehicle for robotic measurements, sampling, and monitoring. (2017)

[Brueckmann et al. 2016] Brueckmann, Warner (. ; Schmidt, Mark (. ; Friesen, Jan (Helmholtz Centre for Environmental Research UFZ L.: Submarine Groundwater Discharge. In: *IATI Contract* (2016)

[Bu and Warner 1995] Bu, X. ; Warner, M.J.: Solubility of chlorofluorocarbon 113 in water and seawater. In: *Deep Sea Research Part I: Oceanographic Research Papers* 42 (1995), Nr. 7, S. 1151–1161. – URL https://www.sciencedirect.com/science/article/pii/0967063795000528

[Bullister et al. 2002] Bullister, John L. ; Wisegarver, David P. ; Menzia, Frederick A.: The solubility of sulfur hexafluoride in water and seawater. In: *Deep Sea Research Part I: Oceanographic Research Papers* 49 (2002), Nr. 1, S. 175–187. – URL https://www.sciencedirect.com/science/article/pii/S0967063701000516

[Chen et al. 1999] Chen, C. Y. ; Li, Y. M. ; Bailey, K. ; O'Connor, T. P. ; Young, L. ; Lu, Z.-T.: Ultrasensitive Isotope Trace Analyses with a Magneto-Optical Trap. In: *Science* 286 (1999), nov, Nr. 5442, S. 1139–1141. – ISSN 0036-8075

[Clark and Fritz 1997] Clark, I. D. ; Fritz, P.: *Tracing the carbon cycle.* 1997

[Clark et al. 1987] Clark, I.D. ; Fritz, P. ; Quinn, O.P. ; Rippon, P.W. ; Nash, H. ; Al Said, S.B.B.G.: Modern and fossil groundwater in an arid environment: a look at the hydrogeology of Southern Oman. In: *Isotope techniques in water resources development* (1987), S. 167–187. – URL http://www.iaea.org/inis/collection/NCLCollectionStore/_Public/38/050/38050469.pdf#page=185

[Climate 2012] Climate: *Climate graph Salalah, Oman.* 2012. – URL https://en.climate-data.org/asia/oman/dhofar/salalah-2087/#climate-graph

[Collon et al. 2004] Collon, Philippe ; Kutschera, Walter ; Lu, Zheng-Tian: Tracing noble gas radionuclides in the environment. In: *Annu. Rev. Nucl. Part. Sci* 54 (2004), S. 39–67

[Cook and Solomon 1995] Cook, P. G. ; Solomon, D. K.: Transport of Atmospheric Trace Gases to the Water Table: Implications for Groundwater Dating with Chlorofluorocarbons and Krypton 85. In: *Water Resources Research* 31 (1995), feb, Nr. 2, S. 263–270. – URL http://doi.wiley.com/10.1029/94WR02232. – ISSN 00431397

[Crowe 1958] Crowe, C.: Carbon-14 activity during the past 5,000 years. In: *Nature* 182 (1958), S. 470–471

[Detwiler 2015] Detwiler, Ross: *Hypoxia, Business and Commercial Aviation.* 2015. – URL http://aviationweek.com/bca/it-s-not-about-breathing

[Devlin and Sophocleous 2005] Devlin, John F. ; Sophocleous, Marios: The persistence of the water budget myth and its relationship to sustainability. In: *Hydrogeology Journal* 13 (2005), Nr. 4, S. 549–554. – ISBN 1431-2174

[D.MI 1992] D.MI: *Water and wastewater masterplan for Salalah.* 1992

[Ebser et al. 2018] Ebser, S. ; Kersting, A. ; Stoeven, T. ; Feng, Z. ; Ringena, L. ; Schmidt, M. ; Tanhua, T. ; Aeschbach, W. ; Oberthaler, M. K.: ^{39}Ar dating with small samples resolves ocean ventilation. In: *Nature Communications* 9 (2018)

[Ebser 2018] Ebser, Sven C.: *Dating of ice and ocean samples with Atom Trap Trace Analysis of* ^{39}*Ar*, University of Heidelberg, Germany, PhD Thesis, 2018

[Feng et al. 2018] Feng, Zhongyi ; Bohleber, Pascal ; Ebser, Sven ; Ringena, Lisa ; Schmidt, Maximilian ; Kersting, Arne ; Hopkins, Philip ; Hoffmann, Helene ; Fischer, Andrea ; Aeschbach, Werner ; Oberthaler, Markus K.: Dating glacier ice of the last millennium by quantum technology. (2018), nov. – URL http://arxiv.org/abs/1811.03955

[Ferrario 1996] Ferrario, B: Chemical pumping in vacuum technology. In: *Vacuum* 47 (1996), apr, Nr. 4, S. 363–370. – URL https://www.sciencedirect.com/science/article/pii/0042207X95002529. – ISSN 0042-207X

[Fitts 2013] Fitts, Charles R.: *Groundwater Science.* URL http://linkinghub.elsevier.com/retrieve/pii/B9780123847058000017, 2013. – ISBN 1471-6771 (Electronic) 0007-0912 (Linking)

[Fleitmann et al. 2007] Fleitmann, Dominik ; Burns, Stephen J. ; Mangini, Augusto ; Mudelsee, Manfred ; Kramers, Jan ; Villa, Igor ; Neff, Ulrich ; Al-Subbary, Abdulkarim A. ; Buettner, Annett ; Hippler, Dorothea ; Matter, Albert: Holocene ITCZ and Indian monsoon dynamics recorded in stalagmites from Oman and Yemen (Socotra). In: *Quaternary Science Reviews* 26 (2007), jan, Nr. 1-2, S. 170–188. – URL `https://www.sciencedirect.com/science/article/pii/S0277379106002265`. – ISSN 0277-3791

[Flint and Rippon 1986] Flint, R. ; Rippon, P.: Geological Reassessment of the Salalah plain aquifer. In: *Council for conservation of environment and water resources* (1986)

[Florkowski 1992] Florkowski, T.: Natural production of radioactive noble gases in the geosphere. In: *Isotopes of noble gases as tracers in environmental studies* (1992)

[Gelhar et al. 1992] Gelhar, Lynn W. ; Welty, Claire ; Rehfeldt, Kenneth R.: A critical review of data on field-scale dispersion in aquifers. In: *Water Resources Research* 28 (1992), jul, Nr. 7, S. 1955–1974. – URL `http://doi.wiley.com/10.1029/92WR00607`. – ISSN 00431397

[Geo Resources Consultancy 2004] Geo Resources Consultancy, GRC: Detailed water resources management and planning study for the Salalah region Part A, Final report. (2004)

[Godwin 1962] Godwin, H.: Half-life of Radiocarbon. In: *Nature* 195 (1962), Nr. 4845, S. 984

[Google Earth a] Google Earth, Digital Globe 2.: *Arabian Peninsula (14.12.2015), eye alt. 2949 km*

[Google Earth b] Google Earth, Digital Globe 2.: *Salalah, Oman (22.10.2018), 17°01'28.78"N, 54°09'01.91"O, eye alt 1,43 km*

[Harnisch et al. 2000] Harnisch, Jochen ; Frische, Matthias ; Borchers, Reinhard ; Eisenhauer, Anton ; Jordan, Armin: Natural fluorinated organics in fluorite and rocks. In: *Geophysical Research Letters* 27 (2000), jul, Nr. 13, S. 1883–1886. – URL `http://doi.wiley.com/10.1029/2000GL008488`. – ISSN 00948276

[Herb 2011] Herb, Christian: *Paleoclimate study based on noble gases and other environmental tracers in groundwater in Dhofar (Southern Oman)*, University of Heidelberg, Diploma Thesis, 2011

[Hopkins 2018] Hopkins, Philip: *Setting up a new argon separation system for glacier ice and ocean dating with ^{39}Ar-ATTA*, University of Heidelberg, Master's Thesis, 2018

[Hubbert 1940] Hubbert, M. K.: The theory of groundwater motion. In: *Geology* 48 (1940), S. 785–944

[IAEA 2006] IAEA: *Use of Chlorofluorocarbons in Hydrology: a Guidebook*. Vienna : International Atomic Energy Agency, 2006

[IAEA 2013] IAEA: *Isotope methods for dating old groundwater*. Vienna : International Atomic Energy Agency, 2013. – ISBN 978-92-0-137210-9

[IATI 2015] IATI: *Water Pilot Projects of the Institute of Advanced Technology Integration*. 2015. – URL `https://www.ufz.de/iati/index.php?en=34100`

[IFA] IFA: *Carbon Dioxide*. – URL `http://gestis-en.itrust.de/nxt/gateway.dll/gestis_en/000000.xml?f=templates$fn=default.htm$vid=gestiseng:sdbeng$3.0`

[Kinzelbach et al. 2002] Kinzelbach, W. ; Aeschbach, W. ; Alberich, C. ; Goni, I.B. ; Beyerle, U. ; Brunner, P. ; Chiang, W.-H. ; Rueedi, J. ; Zoellmann, K.: *A Survey of Methods for Groundwater Recharge in Arid and Semi-arid regions*. Nairobi, Kenya, 2002. – ISBN 92 - 80702131 - 3

[Kipfer et al. 2002] Kipfer, R. ; Aeschbach-Hertig, W. ; Peeters, F. ; Stute, M.: Noble Gases in Lakes and Ground Waters. In: *Reviews in Mineralogy and Geochemistry* 47 (2002), jan, Nr. 1, S. 615–700. – URL `https://pubs.geoscienceworld.org/rimg/article/47/1/615-700/235415`. – ISSN 1529-6466

[Klement 2005] Klement, Rainer: *Optimierung von SF6-Grundwasserprobenahme-Methoden*, University of Heidelberg, Diploma Thesis, 2005

[Leroy et al. 2012] Leroy, S. ; Razin, P. ; Autin, J. ; Bache, F. ; D'Acremont, E. ; Watremez, L. ; Robinet, J. ; Baurion, C. ; Denèle, Y. ; Bellahsen, N. ; Lucazeau, F. ; Rolandone, F. ; Rouzo, S. ; Kiel, J.S. ; Robin, C. ; Guillocheau, F. ; Tiberi, C. ; Basuyau, C. ; Beslier, M.O. ; Ebinger, A.: From rifting to oceanic spreding in the Gulf of Aden: a synthesis. In: *Arabian Journal of Geosciences* 5 (2012), S. 859–901

[Levin et al. 2010a] Levin, I. ; Naegler, T. ; Heinz, R. ; Osusko, D. ; Cuevas, E. ; Engel, A. ; Ilmberger, J. ; Langenfelds, R. L. ; Neininger, B. ; Rohden, C. v. ; Steele, L. P. ; Weller, R. ; Worthy, D. E. ; Zimov, S. A.: The global SF6 source inferred from long-term high precision atmospheric measurements and its comparison with emission inventories. In: *Atmospheric Chemistry and Physics* 10 (2010), mar, Nr. 6, S. 2655–2662. – URL http://www.atmos-chem-phys.net/10/2655/2010/

[Levin et al. 2010b] Levin, Ingeborg ; Naegler, Tobias ; Kromer, Bernd ; Diehl, Moritz ; Francey, Roger J. ; Gomez-Pelaez, Angel J. ; Steele, L. P. ; Wagenbach, Dietmar ; Weller, Rolf ; Worthy, Douglas E.: Observations and modelling of the global distribution and long-term trend of atmospheric 14CO2. In: *Tellus, Series B: Chemical and Physical Meteorology* 62 (2010), Nr. 1, S. 26–46. – ISBN 0280-6509

[Libby 1952] Libby, W.F.: Radiocarbon dating. In: *1. Chicago: University of Chicago Press* (1952)

[Loosli 1983] Loosli, H. H.: A dating method with ^{39}Ar. In: *Earth and Planetary Science Letters* 63 (1983), Nr. 1, S. 51–62. – ISSN 0012821X

[Loosli et al. 2000] Loosli, Heinz H. ; Lehmann, Bernhard E. ; Smethie, William M.: Noble gas radioisotopes: ^{37}Ar, ^{85}Kr, ^{39}Ar, ^{81}Kr. In: Cook, P. (Hrsg.) ; Herczeg, A. (Hrsg.): *Environmental Tracers in Subsurface Hydrology SE.* Springer US, 2000, Kap. 12, S. 379–396

[Maiss and Brenninkmeijer 1998] Maiss, Manfred ; Brenninkmeijer, Carl A. M.: Atmospheric SF6: Trends, Sources, and Prospects. (1998). – URL https://pubs.acs.org/doi/abs/10.1021/es9802807

[McDonnel 2016] McDonnel, Rachel: Groundwater use and policies in Oman. In: *IWMI Project Report: Groundwater governance in the Arab world* 14 (2016)

[Molina and Rowland 1974] Molina, Mario J. ; Rowland, F. S.: Stratospheric sink for chlorofluoromethanes: chlorine atom-catalysed destruction of ozone. In: *Nature* 249 (1974), jun, Nr. 5460, S. 810–812. – URL http://www.nature.com/articles/249810a0. – ISSN 0028-0836

[Mook 2002] Mook, W.G.: Environmental isotopes in the hydrological cycle. Principles and applications. In: *IHP-V Technical Documents in Hydrology* Bd. 1. Paris : UNESCO, 2002

[Mook and van der Pflicht 1999] Mook, W.G. ; Pflicht, J. van der: Reporting 14C activities and concentrations. In: *Radiocarbon 41* (1999), Nr. 3, S. 227 – 239

[Mueller 2012] Mueller, Thomas: *Recharge and residence times in an arid area aquifer*, Technical University Dresden, PhD Thesis, 2012

[Mueller 2018] Mueller, Thomas: *Presentation of the IATI-SGD project: Study area and previous findings.* 2018

[Pearson JR. 1965] Pearson JR., F. J.: Use of C-13/C-12 ratios to correct radiocarbon ages of material initially diluted by limestone. In: *Proceedings of the sixth international conference radiocarbon and tritium dating.* Washington D.C., 1965, S. 357–366

[Porcelli et al. 2002] Porcelli, Donald ; Ballentine, Chris J. ; Wieler, Rainer: An Overview of Noble Gas Geochemistry and Cosmochemistry. In: *Reviews in Mineralogy and Geochemistry* 47 (2002), Nr. 1, S. 1–19

[QGIS] QGIS: *Geographical Information System*

[World population review 2018] review, Webpage World population: *World population review.* 2018. – URL http://worldpopulationreview.com/countries/oman-population/

[Rice 2016] Rice, Ken: *Ocean CO2 uptake - part 2.* 2016. – URL https://andthentheresphysics.wordpress.com/2016/11/02/ocean-co2-uptake-part-2/

[Richey et al. 2015] Richey, Alexandra S. ; Thomas, Brian F. ; Lo, Min-Hui ; Reager, John T. ; Famiglietti, James S. ; Voss, Katalyn ; Swenson, Sean ; Rodell, Matthew: Quantifying renewable groundwater stress with GRACE. In: *Water Resources Research* 51 (2015), Nr. 7, S. 5217–5238. – ISBN 1944-7973

[Ritterbusch et al. 2014] Ritterbusch, F. ; Ebser, S. ; Welte, J. ; Reichel, T. ; Kersting, A. ; Purtschert, R. ; Aeschbach-Hertig, W. ; Oberthaler, M. K.: Groundwater dating with Atom Trap Trace Analysis of ^{39}Ar. In: *Geophysical Research Letters* (2014). – ISSN 19448007

[Robinet et al. 2013] Robinet, J. ; Razin, P. ; Serra-Kiel, J. ; Gallardo-Garcia, A. ; Leroy, S. ; Roger, J. ; Grelaud, C.: The Paleogene pre-rift to syn-rift succession in the Dhofar margin (northeastern Gulf of Aden): Stratigraphy and depositional environments. In: *Tectonophysics* 607 (2013), nov, S. 1–16. – URL `https://www.sciencedirect.com/science/article/pii/S0040195113002618`. – ISSN 0040-1951

[Roth 2017] Roth, Kurt: *Physics of Terrestrial Systems*. 2017

[Roy-Barman and Jeandel 2016] Roy-Barman, Matthieu ; Jeandel, Catherine: *Marine Geochemistry : Ocean Circulation, Carbon Cycle and Climate Change*. Oxford University Press USA, 2016

[Schneider 2014] Schneider, Tim: *Eine Paläoklimastudie an einem Grundwasseraquifersystem in der Nordchinesischen Ebene*, University of Heidelberg, PhD thesis, 2014

[Schwartz and Ibaraki 2011] Schwartz, F. W. ; Ibaraki, M.: Groundwater: A Resource in Decline. In: *Elements* 7 (2011), jun, Nr. 3, S. 175–179. – URL `https://pubs.geoscienceworld.org/elements/article/7/3/175-179/137897`. – ISSN 1811-5209

[Shammas and Jacks 2007] Shammas, M. I. ; Jacks, G.: Seawater intrusion in the Salalah plain aquifer, Oman. In: *Environmental Geology*, 2007. – ISSN 09430105

[Shammas 2008] Shammas, Mahaad I.: The effectiveness of artificial recharge in combating seawater intrusion in Salalah coastal aquifer, Oman. In: *Environmental Geology* 55 (2008), jul, Nr. 1, S. 191–204. – URL `http://link.springer.com/10.1007/s00254-007-0975-4`. – ISSN 0943-0105

[Shammas and Jacks 2008] Shammas, Mahaad I. ; Jacks, Gunnar: Management of the Salalah plain aquifer, Oman. In: *Groundwater for Sustainable Development: Problems, Perspectives and Challenges* 1 (2008), S. 409

[Solomon et al. 1993] Solomon, D. K. ; Schiff, S. L. ; Poreda, R. J. ; Clarke, W. B.: A validation of the ^{3}H/ ^{3}He method for determining groundwater recharge. In: *Water Resources Research* 29 (1993), sep, Nr. 9, S. 2951–2962. – URL http://doi.wiley.com/10.1029/93WR00968. – ISSN 00431397

[Solomon 2000] Solomon, D. K.: ^{4}He in Groundwater. In: *Environmental Tracers in Subsurface Hydrology*. Boston, MA : Springer US, 2000, S. 425–439. – URL http://link.springer.com/10.1007/978-1-4615-4557-6_14

[Sophocleous 2002] Sophocleous, Marios: Interactions between groundwater and surface water: The state of the science. In: *Hydrogeology Journal* 10 (2002), Nr. 1, S. 52–67. – ISBN 1431-2174

[Speicher 2018] Speicher, Ronja: *Refining the Sampling and Extraction for Groundwater Dating with Radiocarbon*, University of Heidelberg, Master's Thesis, 2018

[Still et al. 2003] Still, Christopher J. ; Berry, Joseph A. ; Collatz, G. J. ; DeFries, Ruth S.: Global distribution of C3 and C4 vegetation: Carbon cycle implications. In: *Global Biogeochemical Cycles (AGU)* 17 (2003), Nr. 1

[Stoenner et al. 1965] Stoenner, R.W. ; Schaeffer, O.A ; Katcoff, S.: Half-Lives of Argon-37, Argon-39, and Argon-42. In: *Science* 148 (1965), Nr. 3675

[Strauch et al. 2014] Strauch, Gerhard ; Al-Mashaikhi, Khalid S. ; Bawain, Abdullah ; Knöller, Kay ; Friesen, Jan ; Müller, Thomas: Stable H and O isotope variations reveal sources of recharge in Dhofar, Sultanate of Oman. In: *Isotopes in Environmental and Health Studies* 50 (2014), oct, Nr. 4, S. 475–490. – URL http://www.tandfonline.com/doi/abs/10.1080/10256016.2014.961451. – ISSN 1025-6016

[Suckow 2012] Suckow, Axel: *Lumpy–an interactive lumped parameter modeling code based on MS access and MS excel.* URL https://meetingorganizer.copernicus.org/EGU2012/EGU2012-2763.pdf, 2012. – 2763 S

[Suckow 2014] Suckow, Axel: *Lumped Parameter Modelling of Age Distributions using up to two Parallel Black Boxes.* 2014

[Suess 1955] Suess, H. E.: Radiocarbon concentration in modern wood. In: *Science* 122 (1955), Nr. 3166, S. 415–417

[Swagelok] Swagelok: *Online Catalogue.* – URL https://www.swagelok.de

[Tamers 1975] Tamers, M.A.: Validity of radiocarbon dates on groundwater. In: *Geophysical surveys* (1975), Nr. 2, S. 217–239

[Unkel 2006] Unkel, Ingmar: *AMS-^{14}C-Analysen zur Rekonstruktion der Landschafts-und Kulturgeschichte in der Region Palpa (S-Peru)*, PhD Thesis, 2006

[USGS 2017] USGS: *United States Geological Survey (USGS), Reston Groundwater Dating Laboratory.* 2017. – URL http://water.usgs.gov/lab

[Vogel 1967] Vogel, J. C.: Investigation of groundwater flow with radiocarbon. In: *IAEA-SM-83.* Vienna, 1967, Kap. Isotopes i, S. 355–369

[Vogel 1968] Vogel, J. C.: Investigation of groundwater flow with radiocarbon. In: *Isotopes in Hydrology.* Vienna : International Atomic Energy Agency, 1968, S. 355–369

[Walker et al. 2000] Walker, S. J. ; Weiss, R. F. ; Salameh, P. K.: Reconstructed histories of the annual mean atmospheric mole fractions for the halocarbons CFC-11 CFC-12, CFC-113, and carbon tetrachloride. In: *Journal of Geophysical Research: Oceans* 105 (2000), Nr. C6, S. 14285–14296. – URL http://doi.wiley.com/10.1029/1999JC900273. – ISSN 01480227

[Warner and Weiss 1985] Warner, M. J. ; Weiss, Ray F.: Solubilities of chlorofluorocarbons 11 and 12 in water and seawater. In: *Deep Sea Research Part A. Oceanographic Research Papers* 32 (1985), Nr. 12. – URL https://www.sciencedirect.com/science/article/pii/0198014985900998

[Weiss 1970] Weiss, R. F.: The solubility of nitrogen, oxygen and argon in water and seawater. In: *Deep-Sea Research and Oceanographic Abstracts* (1970), S. 721–735. – ISBN 0011-7471

[Weiss 1971] Weiss, Ray F.: Solubility of helium and neon in water and seawater. In: *Journal of Chemical and Engineering Data* 16 (1971), apr, Nr. 2, S. 235–241. – URL http://pubs.acs.org/doi/abs/10.1021/je60049a019. – ISSN 0021-9568

[Wieser 2011] Wieser, Martin: *Imprints of climatic and environmental change in a regional aquifer system in an arid part of India using noble gases and other environmental tracers*, University of Heidelberg, PhD Thesis, 2011

[Yim and Caron 2006] Yim, Man-Sung ; Caron, François: Life cycle and management of carbon-14 from nuclear power generation. In: *Progress in Nuclear Energy* 48 (2006), jan, Nr. 1, S. 2–36. – URL `https://www.sciencedirect.com/science/article/pii/S0149197005000454`. – ISSN 0149-1970

[Ziegler et al. 1981] Ziegler, H. ; Batanouny, K.H. ; Sankhla, N. ; Vyas, O.P. ; Stichler, W.: The Photosynthetic Pathway Types of some Desert Plants from India, Saudi Arabia, Egypt, and Iraq. In: *Oecologia* 48 (1981), S. 93–99

Acknowledgement

An dieser Stelle möchte ich all denen danken, die mich auf dem Weg zur fertigen Masterarbeit unterstützt haben.

Mein erster Dank gilt Prof. Dr. Werner Aeschbach dafür, dass ich Teil einer Arbeitsgruppe mit so spannenden Forschungsthemen werden durfte und für seine konstruktive Unterstützung - ob aus der Ferne oder die letzten Monate auch vor Ort. Danke auch für das angenehme Klima bei Besprechungen und Gruppensitzungen.

Außerdem möchte ich Prof. Dr. Norbert Frank für die Übernahme der Zweitkorrektur danken sowie auch für die Übernahme der Spezialisierungsprüfung und nicht zuletzt für die lustigen Weihnachtsansprachen.

Danke auch an Dr. Thomas Müller für die Einbeziehung ins Projekt, das Engagement bei der Planung, das Know-How auf der Feldkampagne im Oman und die Unterstützung bei der Interpretation der Daten. Danke auch an Nico Trauth für die angenehme Atmosphäre bei der Feldkampagne.

Ein riesiger Dank gilt zudem meinem Betreuer und Freund Arne Kersting, für die Geduld beim erklären, den antiautoritären Erzieh... Betreuungsstil, die angenehme Zeit im Labor und schöne Pausen dazwischen, mehrere Motivations-Pitches, gute Ideen und Erfahrungswerte, die Zeit im Oman und nicht zuletzt fürs Korrekturlesen meiner Arbeit.

Philip Hopkins möchte ich danken für das Einlernen im Labor, den Spaß beim Bau der Induktionsheizungen, schöne Gespräche und natürlich fürs Korrekturlesen. Danke auch an Yannis Arck für lustige Gespräche sowie gute Musik und die stets frische Brise im Labor.

Vielen Dank auch an die gesamte Arbeitsgruppe für nette Mittagessen, sportliche Pausen, schöne Ausflüge und konstruktive Gruppensitzungen.

Danke an Florian Freund fürs Messen der Edelgasproben und an Ronja Speicher fürs Einlernen in die ^{14}C - Methode.

Danke an das gesamte ATTA-Team des KIP für die schöne Zusammenarbeit und gelegentliche ATTA-Lunches und Dinner. Besonderer Dank geht an Zhongyi Feng für die Betreuung auf der Jagd nach Krypton und das geduldige Erklären.

Vielen Dank an meine WG und Freunde, die mir viel Wärme und Kraft geben.

Nicht zuletzt möchte ich miener Familie dafür danken, dass sie immer für mich da war und ist. Danke für eure Unterstützung.

Erklärung:

Ich versichere, dass ich diese Arbeit selbstständig verfasst habe und keine anderen als die angegebenen Quellen und Hilfsmittel benutzt habe.

Heidelberg, den ....